SPARSITY-AWARE LOW-POWER ADC ARCHITECTURE WITH ADVANCED RECONSTRUCTION ALGORITHMS

A Dissertation

by

JUN ZHOU

Submitted to the Office of Graduate and Professional Studies of
Texas A&M University
in partial fulfillment of the requirements for the degree of

DOCTOR OF PHILOSOPHY

Chair of Committee,	Sebastian Hoyos
Committee Members,	Jose Silva-Martinez
	Peng Li
	Javier A. Jo
Head of Department,	Chanan Singh

August 2014

Major Subject: Electrical Engineering

ABSTRACT

Compressive sensing (CS) technique enables a universal sub-Nyquist sampling of sparse and compressible signals, while still guaranteeing the reliable signal recovery. Its potential lies in the reduced analog-to-digital conversion rate in sampling broadband and/or multi-channel sparse signals, where conventional Nyquist-rate sampling are either technology impossible or extremely hardware costly.

Nevertheless, there are many challenges in the CS hardware design. In coherent sampling, state-of-the-art mixed-signal CS front-ends, such as random demodulator and modulated wideband converter, suffer from high power and nonlinear hardware. In signal recovery, state-of-the-art CS reconstruction methods have tractable computational complexity and probabilistically guaranteed performance. However, they are still high cost (basis pursuit) or noise sensitive (matching pursuit).

In this dissertation, we propose an asynchronous compressive sensing (ACS) front-end and advanced signal reconstruction algorithms to address these challenges. The ACS front-end consists of a continuous-time ternary encoding (CT-TE) scheme which converts signal amplitude variations into high-rate ternary timing signal, and a digital random sampler (DRS) which captures the ternary timing signal at sub-Nyquist rate. The CT-TE employs asynchronous sampling mechanism for pulsed-like input and has signal-dependent conversion rate. The DRS has low power, ease of massive integration, and excellent linearity in comparison to state-of-the-art mixed-signal CS front-ends.

We propose two reconstruction algorithms. One is group-based total variation, which exploits piecewise-constant characteristics and achieves better mean squared error and faster convergence rate than the conventional TV scheme with moderate noise. The second algorithm is split-projection least squares (SPLS), which relies on a series of low-complexity and independent l_2-norm problems with the *prior* on ternary-valued signal. The SPLS scheme has good noise robustness, low-cost signal reconstruction and facilitates a parallel hardware for real-time signal recovery.

In application study, we propose multi-channel filter banks ACS front-end for the interference-robust radar. The proposed receiver performs reliable target detection with nearly 8-fold data compression than Nyquist-rate sampling in the presence of -50dBm wireless interference. We also propose an asynchronous compressed beamformer (ACB) for low-power portable diagnostic ultrasound. The proposed ACB achieves 9-fold data volume compression and only 4.4% contrast-to-noise ratio loss on the imaging results when compared with the Nyquist-rate ADCs.

To my family

ACKNOWLEDGEMENTS

I would like to express my deep gratitude to my advisor, Dr. Sebastian Hoyos, who is the best mentor I could have wished for. His professional guidance and lasting support always encouraged me for challenges over the years. He leads as a maverick thinker. His ability to look beyond limits is a true gift in my research and will continue influencing on my thinking and life. It is my great honor to have been his student and worked with him.

I would also like to express my sincere acknowledgement to my committee members, Dr. Jose Silva-Martinez, for precious instructions on circuit design and analysis, and Dr. Peng Li, Dr. Javier A. Jo for their invaluable guidance and support throughout the course of this research.

I also want to thank Dr. Brian Sadler. He is an exceptional mentor who encourages me to pursue, to persist and to achieve.

Thanks also go to my lab mates Xi, Zhuizhuan, Mario, Ramy and Ehab. It is really great experience working with you. I thank all my friends in AMSC who I've spent those amazing years with.

Last but not least, I would like to thank my mother and father for their always being with me. Thanks to my wife. I could've accomplished little without you.

NOMENCLATURE

ADC	Analog-to-Digital Converter
ACS	Asynchronous Compressive Sensing
ACB	Asynchronous Compressed Beamformer
ASIC	Application-Specific Integrated Circuit
BPDN	Basis Pursuit De-Noise
CNR	Contrast-to-Noise Ratio
CP	Clustering Parameters
CRLB	Cramér–Rao Lower Bound
CS	Compressive Sensing
CT-TE	Continuous-Time Ternary Encoding
DAC	Digital-to-Analog Converter
DFT	Discrete Fourier Transform
DPL	Double Pass-transistor Logic
DRS	Digital Random Sampler
DSP	Digital Signal Processing
ECG	Electrocardiography
ER	Error Rate
FIFO	First-In-First-Out
FPGA	Field-Programmable Gate Array
GTV	Group-based Total Variation

GLRT	Generalized Likelihood Ratio Test
i.i.d.	Independent and identically distributed
IRLS	Iteratively Reweighted Least Squares
ISR	Interference-to-Signal Ratio
LFSR	Linear Feed-Back Shift Register
LPF	Low-Pass Filter
LS	Least Squares
LSB	Least Significant Bit
MIMO	Multiple-Input Multiple-Output
MSE	Mean Squared Error
MVU	Minimum-Variance Unbiased
PN	Pseudorandom Number
PRNG	Pseudo-Random Number Generator
PSF	Point Spread Function
rms	Root mean square
OMP	Orthogonal Matching Pursuit
SNR	Signal-to-Noise Ratio
SPLS	Split-Projection Least Squares
SR	Slew Rate
SSR	Sub-Nyquist Sampling Ratio
TEM	Time Encoding Machine
TV	Total Variation

VLSI	Very-Large-Scale Integration
WBSN	Wireless Body Sensor Networks

TABLE OF CONTENTS

CHAPTER

LIST OF FIGURES

FIGURE Page

FIGURE Page

FIGURE Page

FIGURE Page

LIST OF TABLES

CHAPTER I

INTRODUCTION

I.A. Motivation

Real-world signals like light, pressure, temperature, voice, etc., naturally appear in the analog format. To capture the embedded useful information, various mathematical processing like addition, subtraction, multiplication and division are required. Dedicated analog circuits are adopted if signal processing needs to be carried out directly in the analog domain. Nevertheless, it is more flexible and less expensive to implement them in the digital domain, especially when advanced digital signal processing (DSP) are desired.

Conventional DSP systems take the discrete and quantized samples rather than analog waveform as input signals. Conversion from a continuous band-limited signal to its discrete format requires a minimum sampling rate of twice of the signal bandwidth in order to keep image aliasing free. Such a sampling strategy is known as the famous Shannon/Nyquist sampling theorem [1], which is fundamental in modern DSP systems. The minimum sampling rate of a band-limited signal is called its Nyquist rate. Sampling process generates discrete measurements and quantization process outputs a stream of 1's and 0's to represent the measurements in a digital format. The hardware to fulfill the sampling and quantization tasks is analog-to-digital converter (ADC). Depending on specific application requirements, state-of-the-art ADCs may have various architectures, such as successive approximation register ADC, sigma-delta ADC, pipelined ADC, and time-interleaving ADC, etc. Each architecture makes different trade-off between power,

speed and resolution. However, all of the aforementioned ADC architectures abide by the famous Shannon/Nyquist sampling theorem [2].

Nyquist-rate ADC architecture has encountered challenges in terms of power and area when sampling very wideband and multi-channel signals. For example, wideband spectrum sensing in cognitive radio networks looks for an effective sampling rate up to several tens of gigahertz [3]. Such a high conversion rate together with a moderate to high resolution pushes ADC design to the technology limit [4]. Multi-channel filter-bank approach [5], [6] may relax the ADC requirements in each individual channel, but the aggregated power is very large. Another illustrating example is diagnostic ultrasound imaging system [7], where several hundreds of signal processing channels are designed in parallel to accommodate digital beamforming with a large transducer array. Though Nyquist-rate sampling of one channel requires typically around 50MHz, the aggregated data volume easily goes beyond 300Gbps when 512-channel 12-bit ADCs are employed. Excessive data volume in mixed-signal interface requires large power and complicates the high-speed data link design between analog front-end and digital processing unit.

In addition, Nyquist-rate sampling may not be efficient or optimal in some cases. Most of natural signals are known to be sparse and/or compressible in a certain domain. The mathematical definition on terms “sparse” and “compressible” will be discussed in Chapter II. Here, we simply interpret them as the signal’s information rate is lower than the Nyquist rate. For example, spectrum sensing signal in cognitive radio networks has very broad bandwidth, which means a very large Nyquist rate. However, the spectrum coefficients after Discrete Fourier Transform (DFT) may contain most of zeros, which

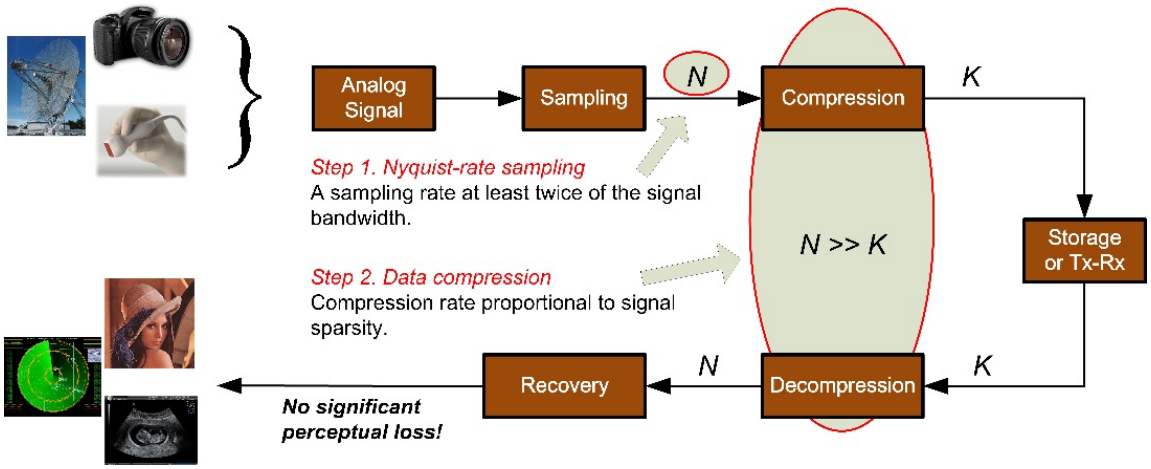

Fig. 1. Block diagram of signal processing chain in conventional DSP systems.

means a very low information rate. Hence, a small set of nonzero spectrum coefficients can well describe the original spectrum sensing signal. Similarly, most of natural images are compressible in the wavelet domain [8]. It means a small set of most significant wavelet coefficients can represent the original image with no significant perceptual loss. The fact that there is low information rate in most of natural signals has enabled various signal compression algorithms [9–12], to name a few. However, nearly all of them require a Nyquist sampling as the first stage. Fig. 1 illustrates the signal processing chain in conventional DSP systems, like camera, radar detection, ultrasound imaging, etc.

It seems to be a great waste in terms of the ADC sampling efforts if we have to first capture all measurements but later on discard most of them after signal compression. A natural question arises, if we have *a prior* that signals are sparse/compressible in a certain domain, can we achieve compression right at the sampling stage? In other words, can we accomplish compressed sampling or sub-Nyquist rate sampling?

Compressive sensing (CS) is a promising technique which enables sub-Nyquist sampling of sparse/compressible signals. According to the CS theorem, any sufficiently sparse and/or compressible signal can be perfectly reconstructed with an overwhelming probability from a much smaller number of incoherent, non-adaptive, randomized linear projection samples relative to the conventional Nyquist-rate sampling systems [13], [14]. The CS technique successfully integrates signal sampling and compression into one step, reducing the sampling rate directly at the analog front-end rather than the digital domain. Because of its sub-Nyquist sampling ability, the CS framework has shown its potential in many applications where Nyquist sampling is either impossible or very costly, such as medical imaging [15], consumer electronics [16], wireless communication [17], statistical signal processing [18], and geophysics [19], etc.

The great potential to wide applications motivates to implement CS technique in practical hardware. A general CS framework consists of two parts: incoherent sampling and signal reconstruction. The first part fulfills the compressed measurements generation. It mainly studies the following questions: (i) what kind of signal is possible for sub-Nyquist rate sampling or compressed sampling? And how much compression can be achieved at the analog front-end relative to the Nyquist rate? (ii) What restrictions are placed on the compressed sampling kernel? (iii) How do we design a compressed sampling front-end in hardware? (iv) Are there any limitations to non-ideal hardware? If so, how do we analyze and address them in CS?

The second part of CS framework is signal reconstruction. It mainly exploits the following areas: (i) is there any algorithm with tractable computational complexity for

reliable signal reconstruction from the compressed measurements? (ii) If so, what's the performance metrics of these algorithms? Are there any constraints? (iii) Can we achieve better performance than some general reconstruction algorithms if more information is available in addition to the signal sparsity? (iv) Can we develop low-complexity signal recovery algorithms that are suitable for low-cost hardware implementation and potential in real-time signal processing?

The aforementioned questions motivate the research work in this dissertation.

I.B. Research Contribution

The objective of this research work is to develop low-power and low-complexity mixed-signal CS front-end together with advanced signal reconstruction algorithms. The power and complexity are co-optimized in both of compressed sampling stage as well as signal reconstruction stage. Numerical analyses are included in the context of some practical applications, such as electrocardiography (ECG) recording in wireless body sensor networks, radar detection with in-band wireless communication interference and low-power portable diagnostic ultrasound imaging systems. Some highlights of this research work are list as follows:

1. A low-power asynchronous compressive sensing (ACS) front-end scheme is proposed, in which asynchronous sampling mechanism is applied for reduced duty cycle of power-demanding circuits.
2. Design considerations on building blocks of the ACS front-end are exploited, including continuous-time ternary encoding (CT-TE) scheme and digital random sampler (DRS). Two types of DRS are designed.

3. A high-performance signal reconstruction algorithm using group-based total variation (GTV) is developed, which achieves better mean squared error (MSE) and faster convergence rate. Performance of the GTV algorithm is evaluated in the context of ECG recording in wireless body sensor networks.
4. A low-complexity signal reconstruction algorithm using split-projection least squares (SPLS) is proposed, which converts the nonlinear and high-cost l_1-norm optimization problem into a series of independent and low-cost least squares (LS) problems.
5. The statistics and computational complexity of the SPLS algorithm are analyzed and compared with state-of-the-art signal reconstruction algorithms. Hardware of the SPLS for real-time CS signal reconstruction is investigated. A *k*-term approximation method to matrix inversion is studied in fixed point.
6. Numerical performance of the SPLS algorithm is studied in the context of radar target detection with in-band wireless communication interference and low-power portable diagnostic ultrasound imaging system.

I.C. Dissertation Organization

The rest of dissertation is organized as follows.

Chapter II reviews the compressive sensing (CS) background, including the incoherent sampling, state-of-the-art mixed-signal CS front-ends and conventional signal reconstruction algorithms. Both advantages and challenges are investigated.

Chapter III presents the proposed ACS front-end. Both continuous-time ternary encoding (CT-TE) and two types of digital random sampler (DRS) will be discussed in

details with signal models and hardware implementation. Comparisons with state-of-the-art mixed-signal CS front-ends are provided.

Chapter IV introduces the group-based total variation (GTV) sparse signal reconstruction algorithm. Main theorem and computational complexity are analyzed. Numerical simulation results are provided in the context of electrocardiography (ECG) recording in wireless body sensor networks.

Chapter V introduces the SPLS signal reconstruction algorithm. Main theorem and computational complexity are also analyzed. The SPLS hardware implementation is discussed. A *k*-term approximation method to matrix inversion in least squares (LS) estimator is also proposed. Numerical results are compared with the theoretical analyses.

Chapter VI investigates the proposed ACS front-end and the SPLS scheme in two applications: radar detection with in-band wireless communication interference and low-power portable diagnostic ultrasound imaging systems. Hardware implementation and optimizations are included for each specific application.

Chapter VII concludes this research work.

CHAPTER II

FUNDAMENTALS OF COMPRESSIVE SENSING

In this chapter, we first define mathematical models for sparse and compressible signals used extensively in compressive sensing (CS). Then we briefly review the incoherent sampling protocol and state-of-the-art mixed-signal CS front-ends. In the end, various CS signal reconstruction algorithms will be discussed.

II.A. Sparse and Compressible Signals

An N-dimensional discrete signal $x \in \mathbb{R}^N$ is called K-sparse if only a maximum of K components out of N are non-zero. Mathematically, we define

$$\|x\|_0 = \left|\mathrm{supp}(x)\right| = \left|\{i : x_i \neq 0\}\right| \quad , \tag{2.1}$$

where support function returns the set of non-zero valued components in x, $\|\ \ \|_0$ is the l_0-norm which counts the number of non-zero items, and $|\ \ |$ function finds the absolute value. Then x is K-sparse if we have

$$\|x\|_0 \leq K \ll N \quad . \tag{2.2}$$

Usually signal x is not sparse in its original format but needs some transformation. A signal x is called *general* K-sparse if the number of non-zero coefficients in a certain representation basis $\boldsymbol{\Psi}$ is smaller than or equal to K,

$$x = \boldsymbol{\Psi} a, \quad \|a\|_0 \leq K \ll N \quad , \tag{2.3}$$

where a represents the coefficients of x in basis $\boldsymbol{\Psi}$. Unless otherwise specified, *general* K-sparse will be denoted as K-sparse for simplicity in this dissertation.

Real-world signals are often compressible rather than strictly sparse. Mathematically, a signal $x = \mathbf{\Psi}a$ is compressible if its coefficient a satisfies power law decay,

$$\left|\left(a^*\right)_i\right| \le Ci^{-\frac{1}{q}} \quad , \tag{2.4}$$

where a^* is the sorted sequence of a with descending order, C is a positive constant, and $0 < q < 1$. By Eq. (2.4), we can see that only a small set of coefficients are significant. Most lossy compression algorithms utilize the most significant coefficients to represent the original signals. Note that the definition of sparse signal is a special case in that of the compressible one.

II.B. Incoherent Sampling

Conventional Shannon/Nyquist sampling scheme employs a uniform distributed Dirac delta streams as the sampling kernel $h(t)$,

$$h\left(t\right) = \begin{cases} \delta(t - nT), & n = 0,1,2,... \\ 0 \quad\quad\quad , & \text{otherwise} \end{cases} \quad , \tag{2.5}$$

where T denotes sampling period, which needs to satisfy the Shannon/Nyquist sampling criterion [1]. The sampling process can be therefore represented as a multiplication,

$$x[n] = x(t) \times h(t) \quad , \tag{2.6}$$

where $x[n]$ represents the discrete sampled sequence of $x(t)$.

Conventional Shannon/Nyquist sampling scheme requires a sampling rate fully dependent on the signal's Nyquist-rate. Signal compression is performed on the discrete samples $x[n]$. Such a sampling technique has dominated the DSP design for more than 50 years though it is inefficient in dealing with sparse and compressible signals, where only a small set of most significant coefficients are actually used during compression.

Recent breakthroughs in compressive sensing (CS) [13], [14] have enabled an innovative sampling framework that integrates sampling and compression into one step. According to the CS theorem, a sparse/compressible signal can be reconstructed with an overwhelming probability from a much smaller number of incoherent, randomized, non-adaptive linear projection measurements relative to the conventional Nyquist sampling systems. In this section, we will introduce incoherent sampling in the context of discrete input signal. The mixed-signal CS signal model and analog front-end hardware will be discussed in the next section.

CS theorem employs non-adaptive linear measurements. The easiest way to do so is by an inner product of the input signal $x \in \mathbb{R}^N$ and the sensing vector $\phi \in \mathbb{R}^N$. Mathematically, the compressed measurements can be represented as the product of an M-by-N sensing or measurement matrix $\mathbf{\Phi}$ and the input signal x,

$$y = \mathbf{\Phi} x \quad . \tag{2.7}$$

It is implicit by compression that the dimension of sensing matrix of $\mathbf{\Phi}$ follows, $M < N$, which means a reduced number of measurements compared with the Nyquist sampling scheme. It is intuitive to recover the sparse signal via an l_0-norm optimization problem, that is

$$\min_x \|x\|_0 \text{ subject to } y = \mathbf{\Phi} x \quad . \tag{2.8}$$

Here it's assumed x itself is sparse. We notice that most of CS literatures have adopted this assumption when analyzing incoherent sampling and signal reconstruction. However, very few papers indeed exploit the results that incorporate a sparse representation basis. We refer the interested readers to [20] for more discussions.

Problem in Eq. (2.8) involves combinatorial search which is NP-hard [13]. One of main contribution of CS theorem is an l_1-norm relaxation (2.9) to l_0-norm problem,

$$\min_x \|x\|_1 \text{ subject to } y = \mathbf{\Phi}x \quad . \tag{2.9}$$

which is convex with tractable complexity when certain conditions are held [13], [14]. The equivalence between l_0-norm and l_1-norm approaches not only requires the sparsity of signal x, but also depends on the incoherence of the sensing or measurement matrix $\mathbf{\Phi}$.

Definition 2.1 [21] *Let* $\mathbf{\Phi} = (\phi_i)_{i=1}^n$ *be an M-by-N matrix. Then its* mutual coherence $\mu(\mathbf{\Phi})$ *is defined as*

$$\mu(\mathbf{\Phi}) = \max_{i \neq j} \frac{|\langle \phi_i, \phi_j \rangle|}{\|\phi_i\|_2 \|\phi_j\|_2} \quad . \tag{2.10}$$

The mutual coherence of a sensing matrix measures the smallest angle between any two columns in $\mathbf{\Phi}$. The upper and lower bounds of mutual coherence are,

$$\sqrt{\frac{N-M}{M(N-1)}} \leq \mu(\mathbf{\Phi}) \leq 1 \quad . \tag{2.11}$$

The mutual coherence of sensing matrix provides a way to quantify the sufficient conditions on the equivalence between l_0-norm and l_1-norm approaches.

Theorem 2.1 ([22], [23]) *Let* $\mathbf{\Phi} = (\phi_i)_{i=1}^n$ *be an M-by-N matrix, and let* $x \in \mathbb{R}^N \backslash \{0\}$ *be a solution of Problem (2.8) satisfying,*

$$\|x\|_0 < \frac{1}{2}\left(1 + \mu(\mathbf{\Phi})^{-1}\right) \quad . \tag{2.12}$$

Then x is the unique solution of Problem (2.8) and Problem (2.9).

Another well-known theorem of sufficient condition on the l_0-norm and l_1-norm equivalence is Restricted Isometry Property (RIP), which is firstly introduced in [24].

Theorem 2.2 ([24]) *Let* $\mathbf{\Phi} = (\phi_i)_{i=1}^n$ *be an M-by-N matrix. Then* $\mathbf{\Phi}$ *has the* Restricted Isometry Property (RIP) *of order K, if there exists a* $\delta_K \in (0, 1)$ *such that for all* $x \in \sum_K$

$$\left(1-\delta_K\right)\|x\|_2^2 \le \|\mathbf{\Phi}x\|_2^2 \le \left(1+\delta_K\right)\|x\|_2^2$$

where $\sum_K$ *is defined as* $\{x \in \mathbb{R}^N : \|x\|_0 \le K\}$

RIP requires the sensing matrix $\mathbf{\Phi}$ preserves the Euclidean length of all *K*-sparse signals during the dimension decrease. Construction of a sensing matrix satisfying RIP is expensive when following a deterministic approach. It is shown in [25] that the number of measurement needs to be larger than K^2 for RIP condition. However, most of random matrices satisfy RIP condition with high probability, as studied in [26],

Theorem 2.3 [26] *Let* $\delta \in (0, 1)$*. If the probability distribution generating the M-by-N matrices* $\mathbf{\Phi}$ *satisfies the concentration inequality with* $\varepsilon = \delta$*, then there exist constants* c_1 *and* c_2 *such that, with probability* $\le 1 - 2e^{-c_2\delta^2 M}$, $\mathbf{\Phi}$ *satisfies the RIP of order K with* δ *for all* $K \le c_1\delta^2 M/\log(N/K)$.

It is also shown in [26] that random matrices generating from independent and identically distributed (*i.i.d.*) Gaussian and Bernoulli random processes satisfy the RIP condition of order *K* with δ if

$$M \ge c \times K \log\left(N/K\right) \quad , \tag{2.13}$$

where c is a constant related to δ. The inequality in (2.13) provides a lower bound on the number of compressed measurements required for the RIP condition for a given specific sparsity. Note that, these random matrices are independent on sparse representation basis $\mathbf{\Psi}$ and have universality property. It means if $\mathbf{\Phi}$ has the RIP, then the combination of $\mathbf{\Phi}$ and $\mathbf{\Psi}$, i.e. $\mathbf{A} = \mathbf{\Phi\Psi}$, also has the RIP with high probability.

II.C. Mixed-Signal CS Front-Ends

As mentioned earlier, the main contribution of CS theorem is the integration of sampling and compression into one step. In previous section, we have reviewed the CS framework in the digital domain. The related theorems are readily to be extended to analog signals. We name the incoherent sampling schemes of analog signals as mixed-signal CS front-ends.

A famous mixed-signal CS front-end is random demodulator, which was firstly presented in [27], [28], and are employed in various applications, [29–32]. As shown in Fig. 2, a random demodulator consists of a pseudorandom number (PN) generator, a mixer, and an integrator. The mixer performs randomization by multiplying the input $x(t)$ with a PN sequence or chipping sequence $p_c(t)$ at continuous time. The analog integrator operates as an anti-aliasing filter and also serves as a sub-Nyquist sampling module. The mixer output is a continuous-time demodulated signal,

$$y(t) = x(t) \times p_c(t) \quad . \tag{2.14}$$

And discrete samples are collected by the integrator at every T seconds,

$$y[n] = \frac{1}{T}\int_{nT}^{(n+1)T} y(t)\,dt, \;\; n = 0,1,\ldots \quad . \tag{2.15}$$

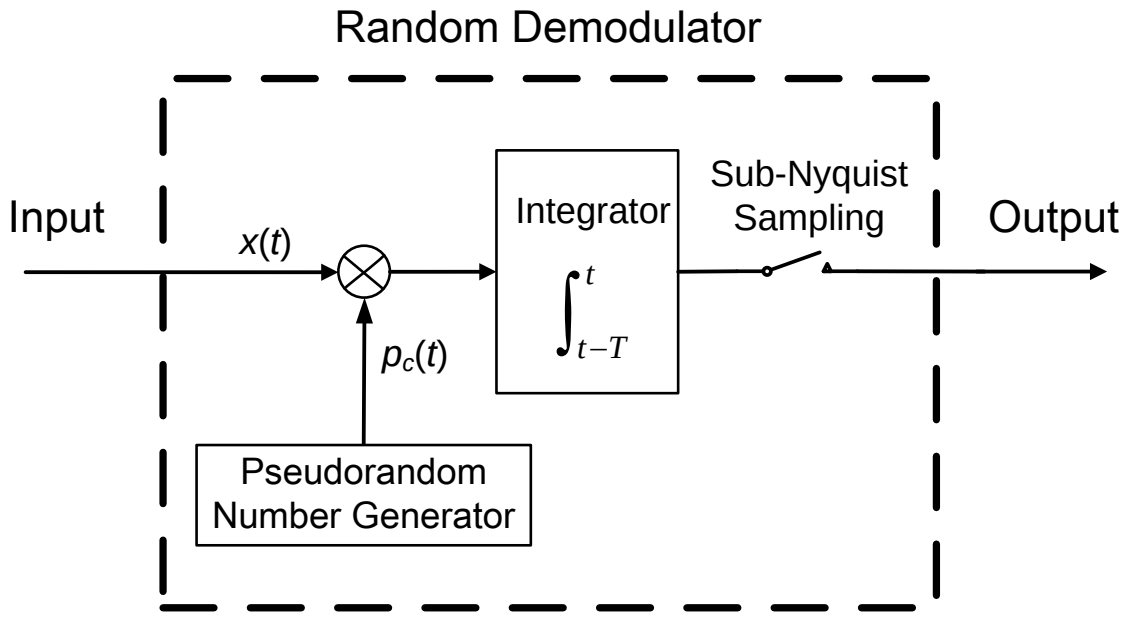

Fig. 2. Block diagram of mixed-signal CS front-end using random demodulator.

The chipping sequence is usually drawn from an *i.i.d.* symmetric Bernoulli distribution due to its low-cost implementation with a linear feed-back shift register (LFSR) circuit [56]. However, the chipping frequency at the mixer needs to be greater than the Nyquist rate for incoherent measurements, resulting in considerable dynamic power. Because both the mixer and integrator have to be active in the entire compressed measurements generation, random demodulator hardware displays excessive dynamic power consumption [34]. Also, dedicated analog circuitries are required to display very good linearity in compressed measurements generation, because non-linear distortion is difficult to compensate and degrade the signal reconstruction [33]. A recent study also shows that the finite rising and falling time of PN sequence limits the mixer sampling

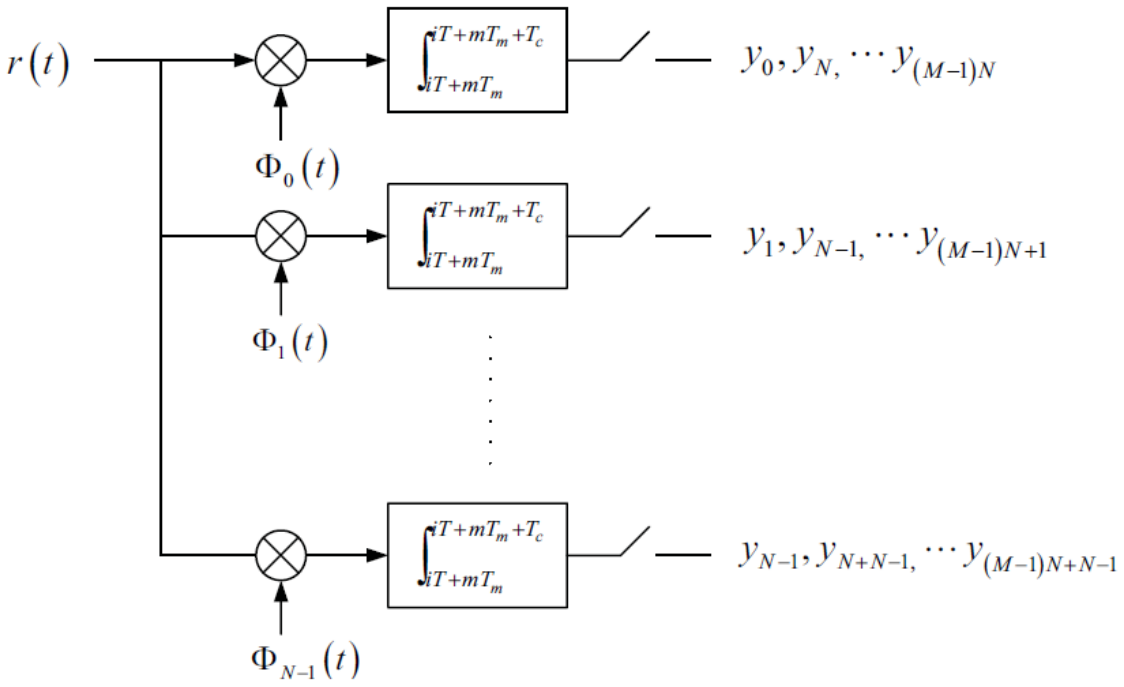

Fig. 3. Architecture of the parallel segmented compressed sensing scheme.

bandwidth and introduces aperture effect which seriously limits the CS performance [116]. This static effect can be compensated by calibration [117].

A random demodulator based extension was proposed in [35], called parallel segmented compressed sensing (PSCS) in Fig. 3. Compressed samples in the PSCS are obtained in parallel by calculating the inner product during a known time period. Each channel collects the measurements independently. The parallel architecture provides design trade-off between the system complexity and the sampling rate of each channel, which is attractive when a single ADC in random demodulator is insufficient. Also, the PSCS design is known to be flexible for spurious frequency rejection [35]. Nevertheless,

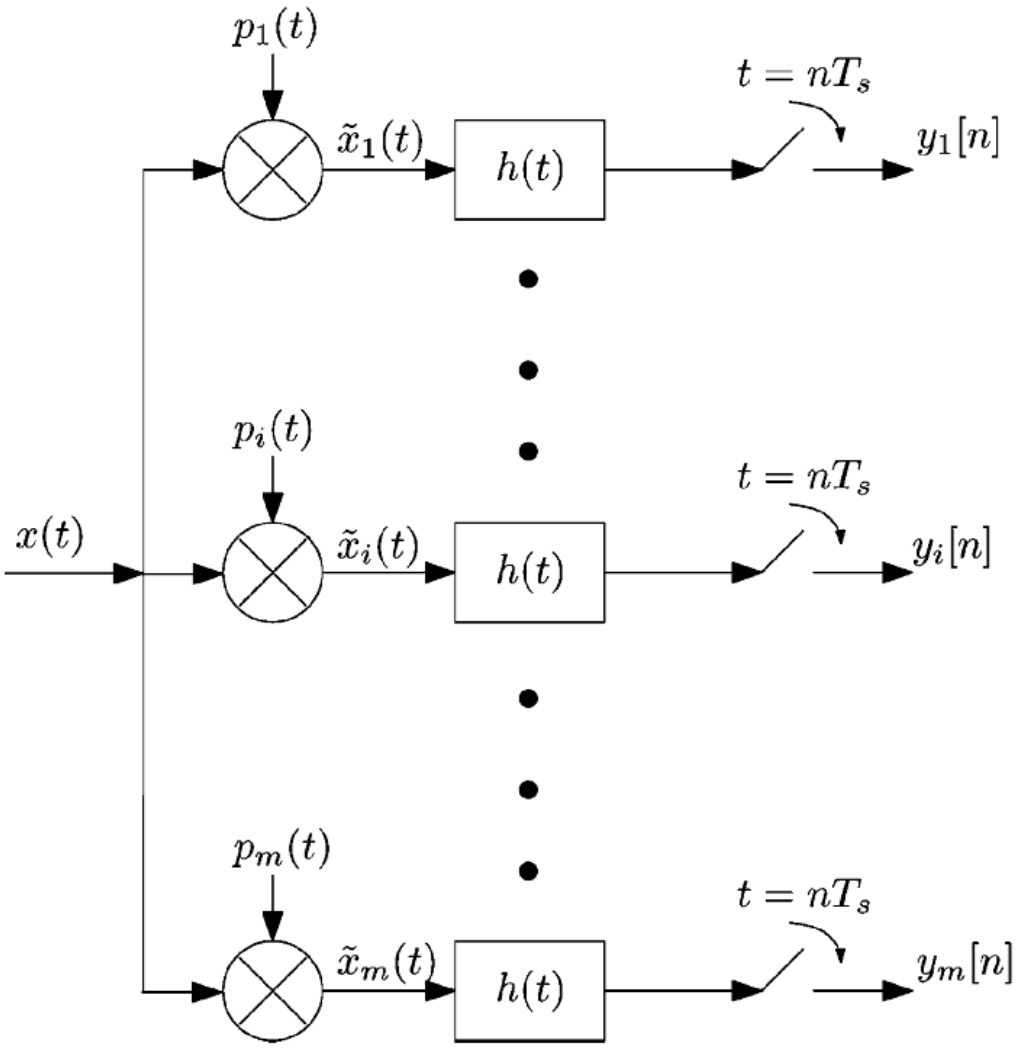

Fig. 4. Architecture of the modulated wideband converter (MWC) scheme.

multiple parallel channels in the PSCS scheme complicates the hardware design and relies on the symmetry between each channel hardware for reliable signal reconstruction.

Another popular mixed-signal CS front-end is modulated wideband converter (MWC), which was initially presented in [36], [37]. Similar with the PSCS scheme, the

MWC also has multiple parallel signal processing channels as shown in Fig. 4. However, instead of utilizing PN sequence as the mixer input, a series of periodic waveforms are employed. With careful adjustments on the number of channels, waveform period, and sampling period, the MWC scheme can satisfy the RIP condition with high probability. The periodic characteristics provide spectrum spreading features, because the periodicity in the time domain implies a series of harmonics in the frequency domain. Therefore, time-domain multiplication results in a band shifting in the frequency domain, which can be utilized to modulate a band-pass component to baseband. After spectrum spreading, the baseband signal is processed by a low-pass filter followed by sub-Nyquist sampling. As shown in [37], the number of active channels is required to be no smaller than four times of the signal bands, resulting in an increased hardware overhead. As an example in [37], 35 channels are employed which is very costly in hardware. In addition, it is also challenging to implement the multiple T-periodic waveforms generation.

We note that the spectrum spreading in the MWC is also similar with the idea of ultra-wideband analog to digital conversion via signal expansion which was presented in [38] and [39]. The differences between the two are that [38] and [39] are applicable to general signals while the MWC scheme is specially optimized for sparse signals.

II.D. Signal Reconstruction

Recovering continuous signals from Nyquist-rate samples can be carried out by interpolation kernels. The ideal interpolation filter has sinc function as impulse response.

However, signal reconstruction from the compressed measurements using CS is much more complicated. As reviewed in previous section, incoherent sampling protocol

enables relaxation from an l_0-norm problem, which is NP-hard, to an l_1-norm problem. Though l_1-norm problem is convex, the algorithms to it are highly nonlinear.

There are mainly two categories of signal reconstruction methods in CS literature [24], [40–44]. One group follows basis pursuit principle using linear programming, such as [24], [40], [41]. Basis pursuit solves the problem in (2.9) in noiseless situation. If the measurements contain observation noise, an additional constraint is required,

$$\min_x \|x\|_1 \text{ subject to } \|\mathbf{\Phi}x - y\|_2^2 \le \varepsilon \quad , \tag{2.16}$$

where $\varepsilon > 0$ is related to the noise. Thus, with a proper regulation parameter λ, Problem in (2.16) can be reformulated to an unconstrained version,

$$\min_x \frac{1}{2}\|\mathbf{\Phi}x - y\|_2^2 + \lambda \|x\|_1 \quad . \tag{2.17}$$

Problem in (2.17) can be solved by various convex optimization algorithms, for example, interior-point method [24], iterative thresholding [45], projected gradient method [46], and Dantzig selector [47]. The complexity of these algorithms is tractable in polynomial time, but it is still considerably high, usually in the order of cubic of problem dimension. The stability of basis pursuit was studied in [48].

Theorem 2.4 [48] *Let* $\mathbf{\Phi}$ *be a measurement matrix satisfying the RIP condition. Then for any K-sparse signal x and the corrupted measurements* $y = \mathbf{\Phi}x + w$ *with* $||w||_2 \le \varepsilon$*, the solution* $\hat{x}$ *to (2.17) satisfies*

$$\|\hat{x} - x\|_2 \le C_K \varepsilon \quad ,$$

where C_K *depends only on the RIP constant* δ*.*

Theorem 2.4 tells that the signal reconstruction via basis pursuit is correct with error proportional to the noise power.

The other group adopts the greedy principle to find the sparse solution by iterations [42–44]. The most famous one is called orthogonal matching pursuit (OMP) [42]. The OMP finds the most correlated atom in sensing matrix at each iteration, and solves a least squares (LS) estimate for the weight. The OMP is an improved successor of matching pursuit [49]. Some extensions on the OMP include CoSaMP [43], stage-wise OMP (StOMP) [44].

The stability of the OMP was studied in [42] and [50].

Theorem 2.5 [42], [50] *Fix $\delta \in (0, 0.36)$ and let $\mathbf{\Phi}$ be an M-by-N Gaussian measurement matrix with $M \geq CK \log(N/\delta)$, where C is a constant. Let x be an arbitrary K-sparse signal in $\mathbb{R}^N$. With probability exceeding 1–2δ that OMP correctly reconstructs the signal x from linear measurements $y = \mathbf{\Phi}x$.*

Both basis pursuit and matching pursuit schemes mentioned above have tractable computational complexity as well as probabilistically guaranteed signal reconstruction performance. However, both of them have limitations, and may become sub-optimal in some situations. For example, greedy methods like matching pursuit are usually faster than convex relaxation and are also friendly to some non-convex constraints. However, its performance is sensitive to heavy observation noise [51]. Basis pursuit is known to be noise robust. But the algorithm is generally much slower, and the computational cost is appreciably greater than direct processing of the Nyquist-rate samples. These drawbacks

limit CS to applications where both good noise robustness and low-cost real-time signal reconstruction are necessities.

Some other numerical methods for signal reconstruction are also available in CS literature, such as the HHS pursuit [52], Fourier sampling [53], Bayesian compressive sensing (Bayesian CS) [54], and smoothed-L0 [55], to name a few.

CHAPTER III

ASYNCHRONOUS COMPRESSIVE SENSING FRONT-END*

In this chapter, we present the proposed low-power asynchronous compressive sensing (ACS) front-end. We firstly introduce the overall signal processing chain of the proposed ACS front-end. Then we study its building blocks in details, such as the continuous-time ternary encoding (CT-TE) and the digital random sampler (DRS). The signal model is derived for each module. Block diagram and hardware of each module are studied. Practical design considerations for each part are also included in this chapter.

III.A. Overview

ADC serves as mixed-signal interface in a DSP system. The mixed-signal CS front-ends reviewed in Chapter II can be considered as a special kind of ADCs that converts sparse analog signals into discrete and quantized samples at its sub-Nyquist rate. A difference between mixed-signal CS front-ends and conventional Nyquist ADCs is that CS-based approaches require an additional signal reconstruction stage before any further DSP processing. Fig. 5 illustrates the signal processing chain of the proposed ACS front-end in a typical mixed-signal system.

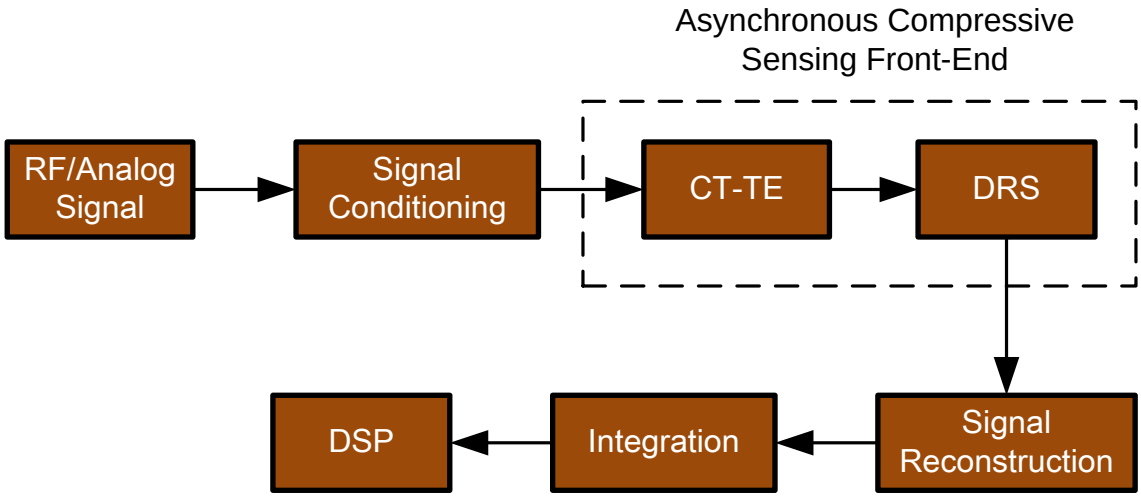

Fig. 5. Signal processing chain of the proposed asynchronous compressive sensing (ACS) front-end in mixed-signal systems.

Unlike conventional ADCs that are applicable to arbitrary band-limited signals, the proposed ACS front-end is limited to sparse and compressible RF/analog signals due to the sparsity constraints in CS framework. It's a reasonable assumption that has been adopted in state-of-the-art mixed-signal CS front-ends. The sparse RF/analog signal is firstly processed by some signal conditioning modules, such as amplifier and filter, etc. Amplifier adjusts the input amplitude to full scale before analog-to-digital conversion, and filter shapes the signal's spectrum and removes the out-band components. This step is generally mandatory in any ADC design. Their effects to the proposed ACS front-end will be discussed in later section. As shown in Fig. 5, the ACS front-end consists of two parts: CT-TE module and DRS module. The CT-TE module converts input amplitude variations into high-rate ternary timing signal, and the DRS module captures the ternary

timing information by compressed samples at a sub-Nyquist rate. Signal reconstruction recovers the ternary timing signal. And the Nyquist-rate samples of RF/analog signal can be restored by an integration module, which are ready for further DSP processing.

The ACS front-end is optimized for pulsed-like signals, which widely present in many electronic systems, for example ultrasound imaging, radar detection and ranging, sensor network, etc. In this chapter, we will focus on the signal model and architecture of the proposed ACS front-end [64]. Chapter IV and Chapter V will introduce two advanced signal reconstruction algorithms for the ACS front-end. Application studies will be presented in Chapter VI.

III.B. Continuous-Time Ternary Encoding

Fig. 6 illustrates the architecture of the continuous-time ternary encoding (CT-TE) scheme, which includes two parts: a comparator and a threshold generator. Suppose the input signal $z(t)$ has been properly pre-amplified to the full scale with a peak-to-peak amplitude U. V_{ref} denotes the reference signal in analog-to-digital conversion. The threshold generator divides U equally into 2^Q levels based on quantization bit Q. At each time, the threshold generator provides a pair of thresholds ($V_{th,L}$, $V_{th,H}$) to the comparator. The difference between $V_{th,L}$ and $V_{th,H}$ is fixed to one quantization step Δ. In the ADC context, it's equal to one least significant bit (LSB) in digit representation.

Visually, one thresholds pair ($V_{th,L}$, $V_{th,H}$) constructs a comparison window for input signal $z(t)$. Initially, the comparison window is adjusted to a quantization level that captures the input signal by calculating its running average. When $z(t)$ goes higher than $V_{th,H}$ or lower than $V_{th,L}$, the comparator outputs "+1" or "–1", respectively and the

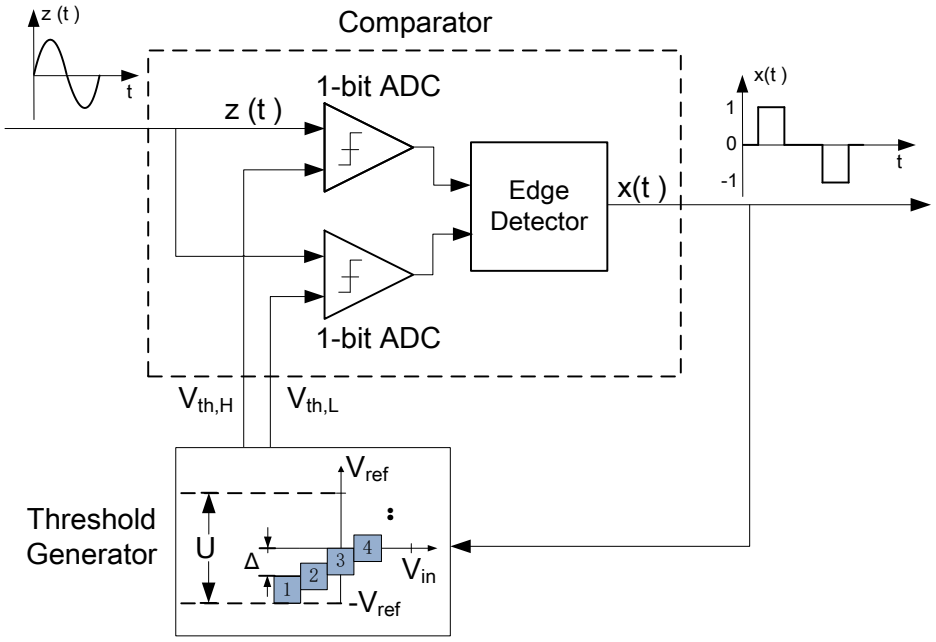

Fig. 6. Architecture of the continuous-time ternary encoding (CT-TE) scheme.

threshold generator will update the comparison window accordingly based on the input amplitude variation for the next comparison; otherwise, the comparator outputs “0”, and the threshold generator holds the current threshold pair unchanged. As a result, the amplitude variations in $z(t)$ are modulated to the ternary timing signal $x(t)$. Without loss of generality, we assign unit amplitude “+1” and “–1” to the comparator outputs pulses.

Mathematically, the operation of the CT-TE module can be modeled by Eq. (3.1) to Eq. (3.3), where τ_1 and τ_2 are finite settling time of the comparator and the threshold generator, respectively, when finite hardware response speed is considered. Note that no clock is involved in the amplitude variation to the ternary timing information conversion. The ternary timing signal and the thresholds pair are fully signal-driven and functions of continuous time.

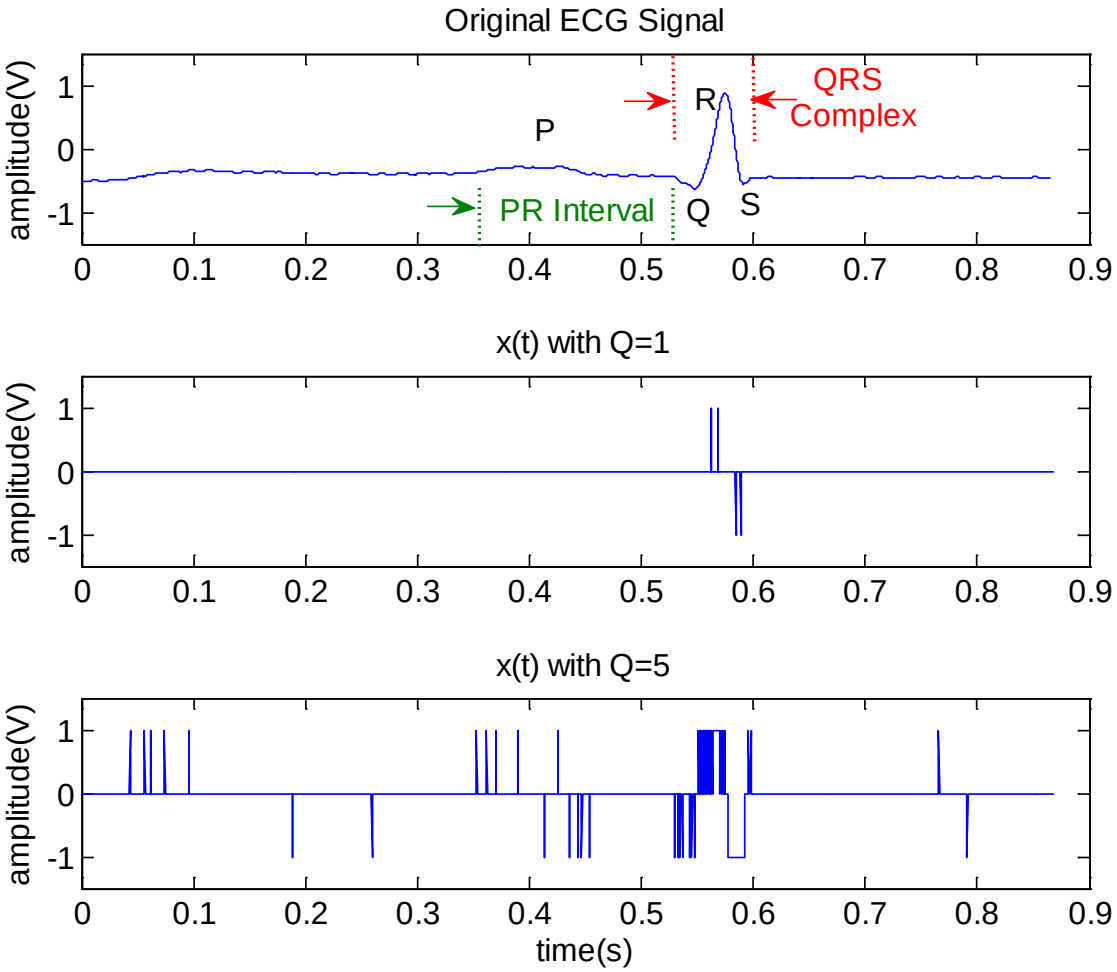

Fig. 7. An example of the CT-TE scheme input and output. From top to bottom, the first waveform shows the original ECG signal. The second waveform shows the output of the CT-TE scheme with $Q = 1$. The third waveform shows the output of the CT-TE scheme when $Q = 5$.

$$x(t-\tau_1)=\begin{cases}1, & \text{if } z(t)>V_{th,H}(t)\\ 0, & \text{if } V_{th,L}(t)\le z(t)\le V_{th,H}(t)\\ -1, & \text{if } z(t)<V_{th,L}(t)\end{cases}. \tag{3.1}$$

$$V_{th,H}(t-\tau_2)=\begin{cases}V_{th,H}(t)+\Delta, & \text{if } x(t)=1\\ V_{th,H}(t), & \text{if } x(t)=0\\ V_{th,H}(t)-\Delta, & \text{if } x(t)=-1\end{cases}. \tag{3.2}$$

$$V_{th,L}(t-\tau_2)=\begin{cases}V_{th,L}(t)+\Delta, & \text{if } x(t)=1\\ V_{th,L}(t), & \text{if } x(t)=0\\ V_{th,L}(t)-\Delta, & \text{if } x(t)=-1\end{cases}. \tag{3.3}$$

The embedded Schmitt trigger structure [57] in the threshold generator makes the proposed CT-TE scheme robust to moderate noise. Although this structure requires one additional bit ability in the threshold resolution, we argue that the effective resolution of the comparator is still *Q*-bit. Fig. 7 shows the output of the CT-TE scheme with a typical ECG signal at the input. With Q = 1, the pulse in output $x(t)$ concentrates around the QRS complex where significant variation occurs. However, $x(t)$ remains 0 for most of the other time. Hence, $x(t)$ is a ternary approximation of the original signal with timing information that captures the most significant variations. A significant variation refers to the one that exceeds the given resolution. By increasing *Q*, the CT-TE scheme increases the ability to detect small variations. As shown in the third plot when Q = 5, the CT-TE scheme is able to response to smaller amplitude variations that exceed 5-bit resolution.

The CT-TE scheme is different from some other modulation methods that also convert the amplitude information to timing signals, like the time encoding machine (TEM) [58], Delta modulation [59] and integrate-and-fire scheme [60]. Both the TEM

and delta modulation include a negative feedback loop to lock the input signal variations. Once starting, the entire circuit keeps on flip-flopping, like a sigma-delta modulator output with constant input, and firing all the time even when there is no amplitude variations at the input. The integrate-and-fire scheme calculates the weighted running average and also fires even if no amplitude variation occurs, resulting in unnecessary power overhead. Whereas in the CT-TE scheme, the circuits fire only when significant variation occurs, which have been shown in Fig. 7. Therefore, the CT-TE scheme has less firing overhead in converting the amplitude variations into timing information and thus exhibits more power efficiency for pulsed-like signals.

The CT-TE scheme also introduces quantization noise like the conventional ADCs. Obviously, a larger quantization bit Q in DAC provides a higher resolution. However, the comparator requires some sufficiently large settling time to provide a stable output and the threshold generator also requires time to update the comparison window properly. Therefore, the achievable Q is constrained by the slew rate of signal and the settling time of the circuitry. Let SR denote the slew rate of the input signal $z(t)$,

$$SR = \max\left(\left|\frac{dz(t)}{dt}\right|\right) \quad . \tag{3.4}$$

Assume settling time of entire circuitry is $\tau = \tau_1+\tau_2$, the maximum allowable Q is

$$Q \le \log_2 \frac{U}{SR \cdot \tau} - 1 \quad . \tag{3.5}$$

If the CT-TE module in Fig. 6 violates (3.5), $x(t)$ cannot provide sufficient pulses to represent variations larger than 2Δ due to the ternary output in each comparison. As a result, $x(t)$ is not able to track fast variations. It is referred to as overflow distortion.

The design constraint in (3.5) tells that the conversion rate of the CT-TE scheme should be high enough to satisfy slew rate requirement. Sometimes, the conversion rate may be even higher than the Nyquist rate, resulting in oversampling in the ternary timing signal. However, we argue that the CT-TE scheme is much simpler in hardware than the conventional ADCs. In addition, the conventional ADCs carry out amplitude sampling without memory. It means each samples are captured and quantized independent. While the CT-TE scheme follows amplitude sampling with memory. The high-rate ternary timing signals have low information rate for pulsed-like input. The sparsity motivates the usage of an event-driven sampling.

Fig. 8 shows an illustration of received pulse signal and its corresponding output waveform using different amplitude sampling schemes with memory. Delta modulation and the CT-TE scheme have 5-bit DAC, Sigma-Delta modulation has 1-bit DAC.

In addition to the finite response rate, for small input signals the comparator may enter into metastable state and fail to resolve within the assigned time. This unpredictability of the comparator can cause errors in the subsequent logic. In order to quantify the probability of a metastability error, we analyze the step response of a typical two-stage open-loop comparator with a DC gain of A_{DC} [61]. Its frequency response is

$$A_v(s) = \frac{A_{DC}}{\left(\frac{s}{p_1}+1\right)\left(\frac{s}{p_2}+1\right)} \quad , \tag{3.6}$$

where p_1 and p_2 are the comparator's two poles. The step response when $p_1 \neq p_2$ is

$$v_{out}(t) = A_{DC} v_{in}\left[1 + \frac{p_2}{p_1 - p_2} e^{-p_1 t} - \frac{p_1}{p_1 - p_2} e^{-p_2 t}\right] \quad , \tag{3.7}$$

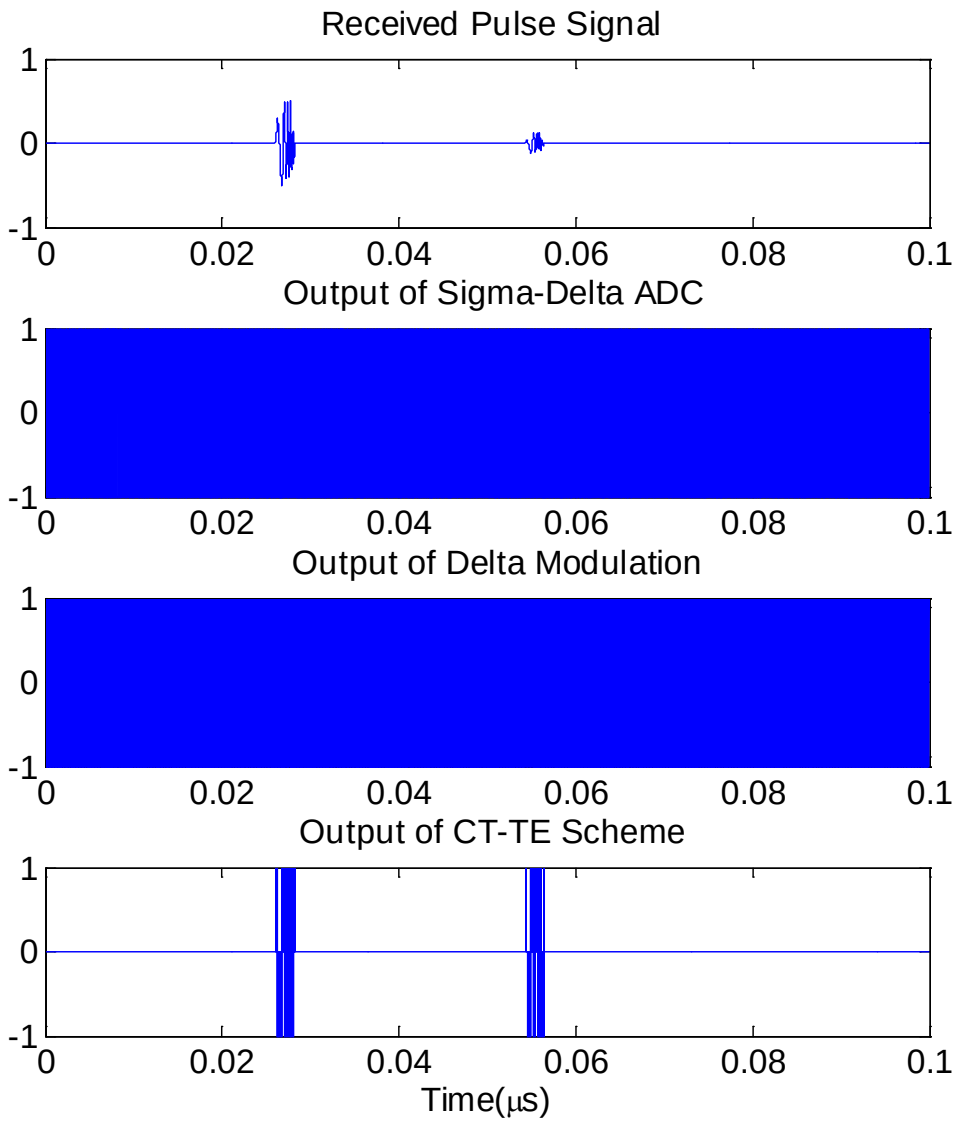

Fig. 8. An illustration of received pulse signal and its corresponding output waveform using different amplitude sampling schemes with memory. Delta modulation and the CT-TE scheme have 5-bit DAC, Sigma-Delta modulation has 1-bit DAC.

Assuming a uniform input amplitude distribution, the probability of metastability error P_{err} by the end of settling time τ is

$$P_{err} = \frac{2\left(2^{Q} - 1\right)V_L}{A_{DC}U\left[1 + \frac{p_2}{p_1 - p_2}e^{-p_1\tau} - \frac{p_1}{p_1 - p_2}e^{-p_2\tau}\right]}, \tag{3.8}$$

where V_L is the valid logic level. Note that a small Q decreases the probability of metastability error.

In order to suppress the metastability in the edge detector unit in Fig. 6, we can employ a double pass-transistor logic (DPL) [62] which has potential for high-speed design due to its low input capacitance. Also, the DPL provides dual logic paths for every logic function. It introduces additional robustness to track amplitude variation.

Comparator offset is also an important issue. A static offset displays compression or extension to each of the piecewise-constant section of $x(t)$, with an extreme case being when the offsets in the two 1-bit ADCs reach to one quantization step Δ. In such a case, the comparator in Fig. 6 may be unstable. While auto-zeroing technique [63] is able to effectively reduce this input offset, ultimately this is limited by circuit non-idealities such as charge injection. Hence, the maximum Q is jointly determined by Eq. (3.5), (3.8), and offset considerations.

The block diagram of hardware implementation of the CT-TE scheme is shown in Fig. 9. The 1-bit ADCs in Fig. 6 are implemented by comparators. The edge detector is implemented by an adder with saturation. Saturation function limits the maximum adder output to be ±1. The output of adder is the ternary timing information, which will be captured by the digital random sampler introduced in the next section. In Fig. 9, an

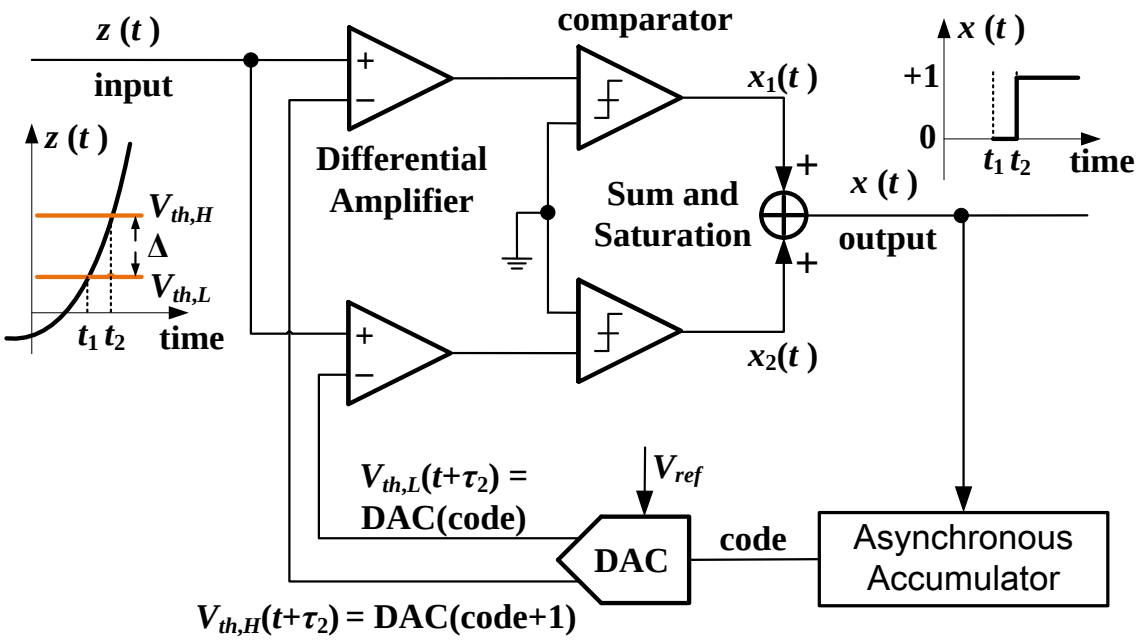

Fig. 9. Block diagram of hardware implementation of the CT-TE scheme.

accumulator is employed to update the DAC input. It is worthy to mentioning that the adder and accumulator are designed in combinational logics which are sensitive to input changes only. Asynchronous sampling mechanism features a reduced duty cycle, and therefore reduced power consumption in capturing pulsed-like signals as only significant amplitude variations are captured by the CT-TE scheme. Quantitative analyses in the context of ECG recording in wireless body sensor networks are provided in Section D.

III.C. Digital Random Sampler

The ternary characteristics of $x(t)$ facilitates digital-assisted CS hardware. Firstly, the dedicated analog mixer for multiplication in state-of-the-art mixed-signal CS front-ends, like random demodulator, PSCS, and MWC, is replaced by a simple register that

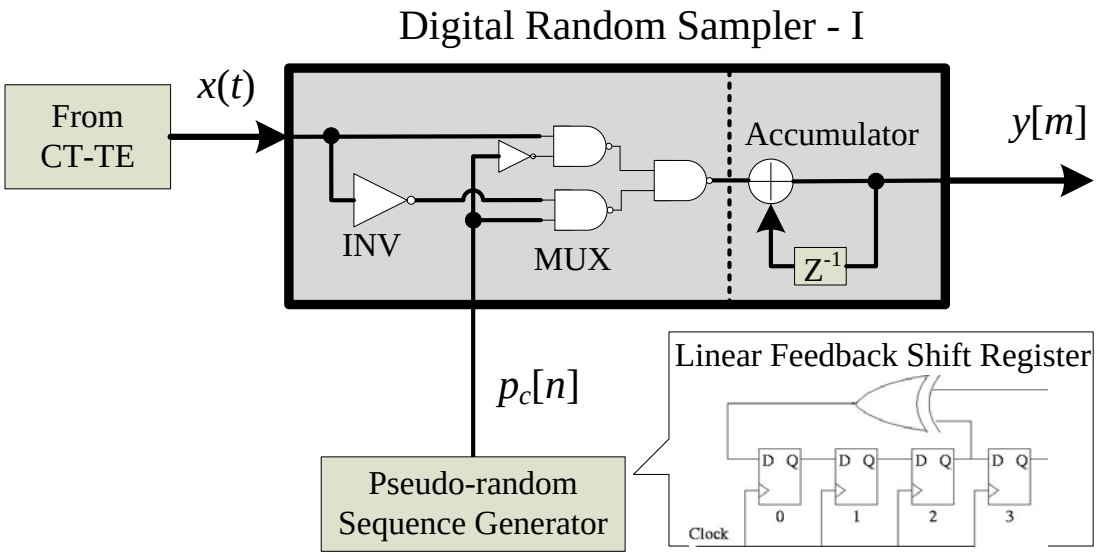

Fig. 10. Block diagram of the first type digital random sampler (DRS-I).

adjusts the sign of chipping sequence according to ternary input. Secondly, inner product of any chipping sequence with zero-valued input is trivial and can be saved. Thirdly, the analog integrator can be replaced by a digital accumulator. The digital circuitry exhibits many advantages, such as low power, ease of massive integration and excellent linearity in compressed measurements generation.

Fig. 10 presents the proposed first type digital random sampler (DRS-I), which replaces the dedicated analog modules with digital circuitry and optimized for ternary input. Note that the CT-TE output is asynchronous to any clock, while the accumulator module in DRS-I is synchronous. Therefore, an asynchronous-to synchronous interface is required. Typically, first-in-first-out (FIFO) block is designed for this interface, which supports asynchronous write, synchronous read and metastability control [65].

DRS-I can be further optimized by taking the piecewise-constant characteristics of ternary input into account, and we name it as DRS-II. Specifically, with a proper Q and τ, output of the CT-TE scheme exhibits ternary piecewise-constant characteristics, i.e. $x(t) = \{-1, 0, 1\}$. A discrete set of time instances, $\boldsymbol{T} = \{T_0, T_1, T_2, \ldots\}$ represents the time instants of each transition edge in $x(t)$. Since $x(t)$ has only three possible values or states, two thresholds are sufficient for the transition edge detection. Note that no clock is involved in either the CT-TE module or transition time detection. In other words, their outputs are fully signal-driven and functions of continuous time. These two circuits are operating in an asynchronous mode.

In this architecture, we explore the time period between two successive transition edges rather than $\boldsymbol{T}$ itself. Let $T_{i \to i+1}$ denote the time period between the i^{th} and $(i+1)^{\text{th}}$ transition. In the following discussion, we focus on one piecewise-constant section. $T_{i \to i+1}$ can be quantized by counting the elapsed clock cycles C_i running at a predefined frequency f_c,

$$C_i = \left\lfloor \frac{T_{i \to i+1}}{\Delta t} \right\rfloor \quad . \tag{3.9}$$

where $\Delta t = 1/ f_c$. Usually f_c is higher than the Nyquist rate of the input signal to provide sufficient timing resolution.

As reviewed in Chapter II, CS front-end modulates sparse signals into incoherent measurements by linear projections and later recovers them from a reduced number of measurements relative to a Nyquist sampling system. The CS measurements generation involves inner product calculation, which includes two operations: randomization and

integration. For a piecewise-constant signal, we have following transformation in each constant section,

$$\sum_{n=1}^{C_i} x[n] \cdot p_c[n] = x[1] \cdot \sum_{n=1}^{C_i} p_c[n] \quad . \tag{3.10}$$

where $p_c[n]$ stands for chipping sequence from the pseudo-random number generator (PRNG), $x[n]$ is the discrete sample from $x(t)$ at the same sampling rate as that in PRNG, which is higher than the Nyquist rate [50]. In the random demodulator, the mixer and integrator have to operate continuously during the entire CS measurements generation. By Eq. (3.10), such an operation can be simplified to the accumulation of the chipping sequence followed by a single multiplication with the first sample of each piecewise-constant section $x[1]$. Additionally, $x[n]$ is ternary, i.e. $x[n] \in \{-1, 0, 1\}$, Eq. (3.10) can be further simplified to (3.11).

$$x[1] \cdot \sum_{n=1}^{C_i} p_c[n] = \begin{cases} \text{sign}\left(x[1]\right) \cdot \sum_{n=1}^{C_i} p_c[n], & \text{if } x[1] \neq 0 \\ 0, & \text{if } x[1] = 0 \end{cases} \quad . \tag{3.11}$$

Equation (3.11) is more favorable in circuit design because the CS measurements generation can be efficiently implemented by digital accumulator rather than a dedicated analog mixer and an integrator in random demodulator (Fig. 2). As shown in [34], the PN sequence demands significant buffering effort before being applied to the mixer, resulting in significant static power overhead. Also, the nonlinear analog mixing greatly affects the signal reconstruction performance [33]. By leveraging the piecewise-constant property, the proposed DRS-II enjoys the advantages of digital circuitry scaling, such as smaller area, lower static power consumption, and excellent linearity, etc.

Moreover, power can be further optimized by shutting down the PRNG during the time period when $x[n] = 0$. As shown in Eq. (3.11), the inner product of 0 with any sequence is trivial. Therefore, we can optimize the PRNG in the DRS-II to be active only for nonzero-valued sections; otherwise it is deactivated. Such a reduced duty cycle of randomization scheme optimizes the operating time of the PRNG. As reported in [34], the combination of PRNG and randomization procedure accounts for nearly half of the entire power in a random demodulator. A smaller duty cycle of high-power modules directly decreases the on-chip power during the CS measurements generation.

Though the aforementioned reduced duty cycle in randomization is attractive, it may prohibit the recovery of the original signal as we abandon all zero-valued sections of $x[n]$ in measurements. Actually, randomization is performed on a concatenated signal with all nonzero-valued sections of $x[n]$ rather than the original one. As a consequence, the timing signal with zero-valued sections is missing in the random sampling stage. The detailed timing information of all zero-valued sections must be included in the CS measurements in order to ensure an exact reconstruction of the original signal.

Recall that $x[n]$ is ternary piecewise-constant with unit amplitude in nonzero-valued sections. The length of a certain zero-valued section (for example i^{th} section) in $x[n]$ can be modulated to the amplitude of its next ($(i+1)^{\text{th}}$ section) nonzero-valued section without blurring any amplitude information. Mathematically, the output of CS measurements can be denoted as,

$$y[m] = \operatorname{sign}\left(x[1]\right) \cdot A_{i+1} \cdot \sum_{n=1}^{C_{i+1}} p_c[n] \quad . \tag{3.12}$$

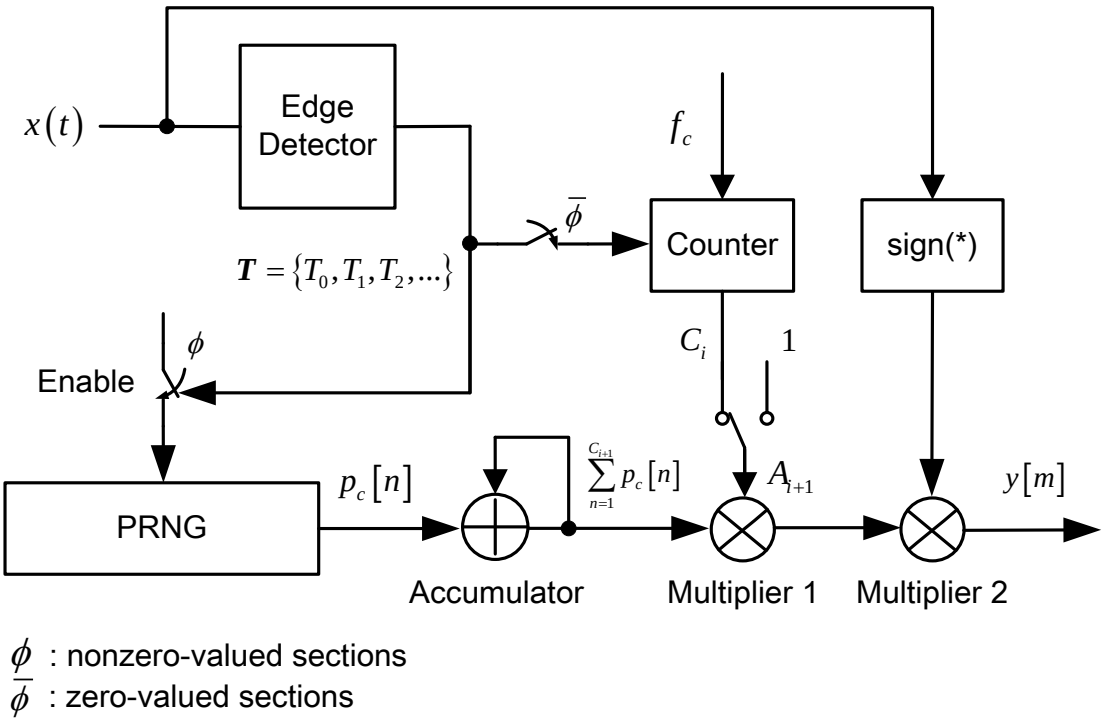

Fig. 11. Block diagram of the proposed second type digital random sampler (DRS-II).

$$A_{i+1} = \begin{cases} C_i, & \text{if } i^{\text{th}} \text{ section is zero} \\ 1, & \text{if } i^{\text{th}} \text{ section is nonzero} \end{cases} . \tag{3.13}$$

where m denotes the measurement index, C_i and C_{i+1} denotes the length of the current zero-valued section (i^{th} section) and that of the next nonzero-valued section ((i+1)$^{\text{th}}$ section), respectively. A_{i+1} is the amplitude of (i+1)$^{\text{th}}$ section.

Fig. 11 shows the block diagram of the proposed second type digital random sampler (DRS-II) in the ACS random sampling stage. The edge detector locates each

transition edge in the input $x(t)$. Depending on the values of piecewise-constant sections, the proposed DRS-II has two operating periods, ϕ and $\bar{\phi}$.

In period ϕ, when nonzero-valued sections are detected, the PRNG is enabled to generate PN sequence while the counter is disabled to save power.

In period $\bar{\phi}$, when zero-valued sections are detected, the PRNG is disabled while the counter is enabled to quantize the length of the current zero-valued section. It means that the PRNG and the accumulator are operating at period ϕ only.

Suppose T_i and T_{i+1} stand for the leading and lagging transition time of a zero-valued section. The DRS-II enters period $\bar{\phi}$ at T_i. The quantized length of this zero-valued section, C_i as shown in Eq. (3.9), is prepared to be modulated to the amplitude of its next nonzero-valued section. In the circuit design, it is equivalent to feed C_i and the accumulated PN sequence to the Multiplier 1 in Fig. 11 according to (3.12). Meanwhile, the PRNG stops and holds the state at T_i in period $\bar{\phi}$.

The DRS-II enters period ϕ at T_{i+1}. The amplitude modulation is carried out by Multiplier 1, and the counter is reset to 0 for the next zero-valued section. The PRNG may resume working or continue holding its current state depending on the value of the upcoming piecewise-constant section. Multiplier 2 adjusts the sign of measurements and finalizes the CS measurements generation. In hardware implementation, Multiplier 2 can be efficiently implemented by a single register that adjusts the input sign. The following Table 1 summarizes the operation of the proposed DRS-II for the ACS front-end.

Table 1. Pseudo-code for the DRS-II operation.

Pseudo Code for the DRS-II Operation

INPUT: the ternary timing information $x(t)$, the PN sequence P_c.

OUTPUT: the CS measurements $y[m]$.

PROCEDURE:

1. Initialize counters i and m to 1, section amplitude $A_{i+1} = 1$.
2. **while** signal $x(t)$, **do**
3. Edge detection to identify i^{th} piecewise-constant section, $x[n]$, $n = 1, 2, \ldots, C_i$.
4. **if** the section value $x[1]$ equals to 0.
5. $\bar{\phi}$: The amplitude of next nonzero-valued section is $A_{i+1} = C_i$, output halts.
6. **else**
7. ϕ: The CS measurements $y[m] = \text{sign}(x[1]) \cdot A_{i+1} \cdot \sum_{n=1}^{C_{i+1}} p_c[n]$, reset $A_{i+1} = 1$, increment m.
8. **end if**
9. Increment i.
10. **end while**
11. **return** y

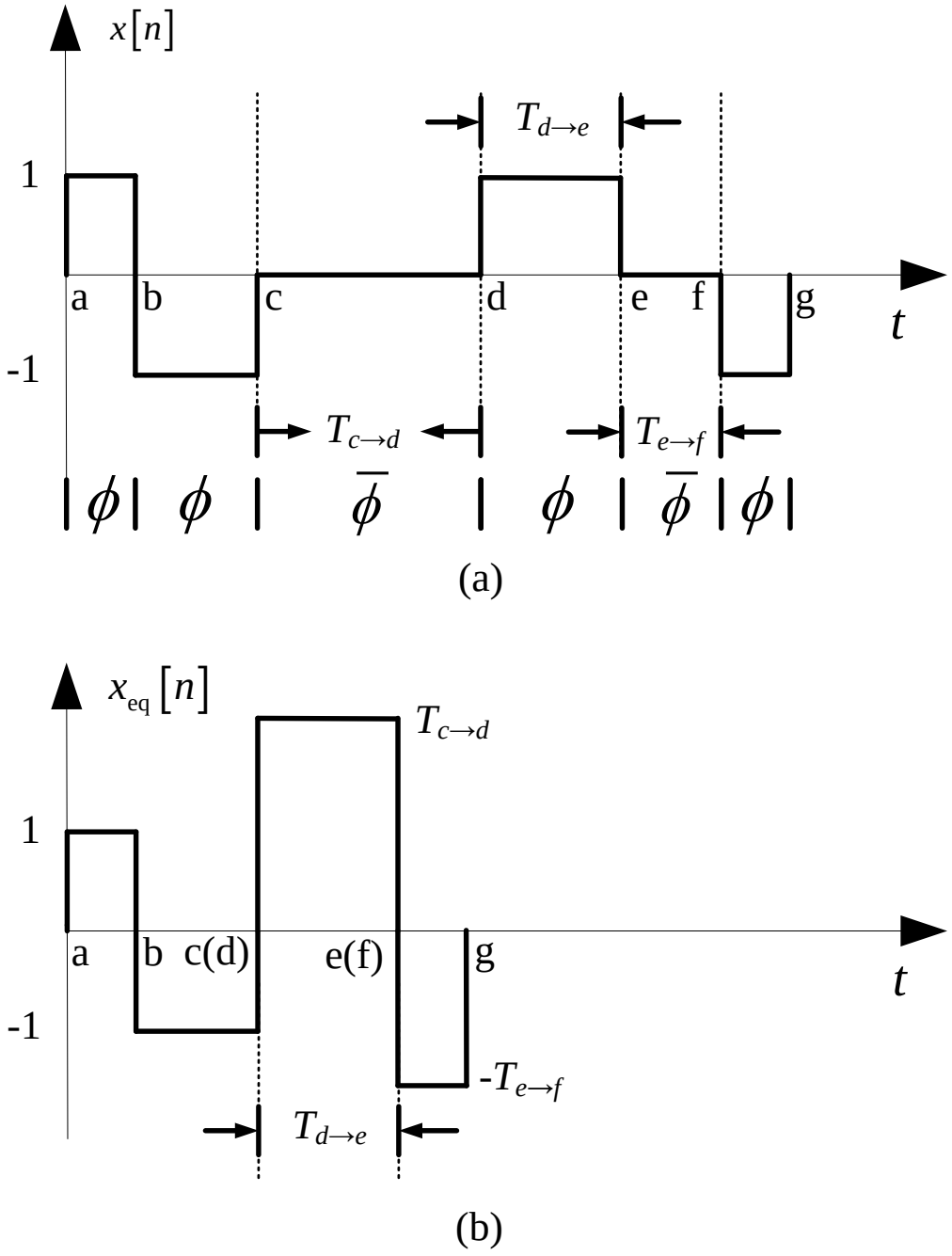

Fig. 12. An example of the equivalent signal in the proposed DRS-II. (a) The original ternary piecewise-constant signal; (b) The equivalent compact signal for randomization.

Since the randomization in the proposed DRS-II is performed on a concatenated signal rather than the original one $x[n]$, it is worthy to look at the equivalent signal $x_{eq}[n]$ in the CS measurements. We refer to $x_{eq}[n]$ as the equivalent compact form of $x[n]$, shown in Fig. 12. Suppose the output of the CT-TE scheme $x(t)$ has a waveform shown in Fig. 12 (a). Then the edge detector finds each transition edge in $x(t)$. In this paper, we assume the edge detector has been properly designed to detect all transition edges. For convenience, we mark them from a to g. The DRS-II enters operating period ϕ during the nonzero-valued sections. At this time, the counter keeps silent and the equivalent compact signal $x_{eq}[n]$ just copies the input to output, like sections (a, b) and (b, c). When zero-valued section (c, d) comes, the DRS-II enters operating period $\bar{\phi}$ and the counter starts calculating its length $T_{c\to d}$, which is later on modulated to the amplitude of its next nonzero-valued section (d, e), as shown in Fig. 12 (b). Similar operations are carried out on section (f, g). The final equivalent compact signal $x_{eq}[n]$ is shown in Fig. 12 (b). Note that, the equivalent compact signal $x_{eq}[n]$ is no longer a ternary-valued signal like $x[n]$. However, $x_{eq}[n]$ is still piecewise-constant and includes all information of the original $x[n]$ in the CS measurements generation.

In order to quantify the duty cycle reduction, we introduce a metric for duty cycle reduction or part-time ratio, and define it as the ratio of total randomization time of the equivalent compact signal $x_{eq}[n]$ over that of the original ternary signal $x[n]$,

$$r_{\text{duty cycle}} = \frac{\sum_{i\in x_{eq}} T_{i\to i+1}}{\sum_{i\in x} T_{i\to i+1}} \quad . \tag{3.14}$$

It is worthy to point out that the ACS front-end has very high power efficiency for pulsed-like signals, e.g. ECG signal, ultra-wide band (UWB) pulse signal, radar signal, ultrasound signal, etc. This is because the ACS front-end targets at the amplitude variations and optimizes the duty cycle of power-demanding modules which otherwise should be always on, such as the ones in random demodulator. Besides, the proposed ACS front-end is not restricted to time-sparse signals only. For example, tone signals also have equivalent compact signals $x_{\text{eq}}[n]$ with the ACS front-end. Then, all signal processing presented previously can be directly applied. However, the power efficiency decreases when a signal is sparse in other domain rather than time domain, because the duty cycle of power-demanding modules increases as the signal activity increases.

III.D. Design Considerations

To analyze the performance of the ACS front-end, a 1-channel version (Fig. 5) is constructed. A typical ECG signal from the MIT-BIH Arrhythmia Database [66] is used as input signal for illustration. In the following simulations, one complete cycle of ECG signal is adopted.

Recall that the CT-TE module operates in an asynchronous mode, and there is no explicit sampling and hold clock. The finite settling time of comparator and DAC limits both the maximum response rate to input variation and the maximum resolution. From (3.5), Q is upper-bounded by the signal's slew rate and circuit settling time τ. Assuming a comparison rate of $1/\tau$ and a full-scale ECG signal of 2 V_{pp} and 100 V/s slew rate, the relationship between the minimum comparison rate and the quantization bit Q is shown in Fig. 13. As Q increases, the required comparison rate of the CT-TE module increases

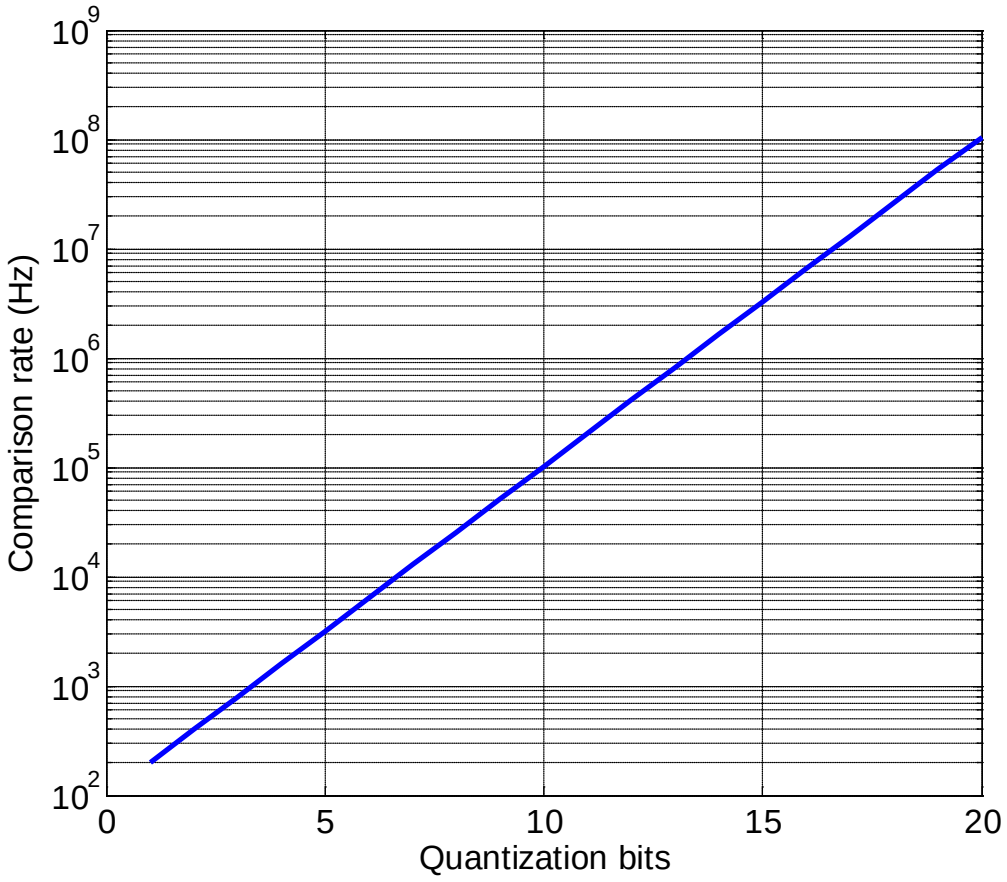

Fig. 13. The relationship between minimal comparison rate and quantization bits for typical ECG signals from MIT-BIH Arrhythmia Database.

exponentially. Therefore, a high-speed CT-TE circuitry is required for a high-resolution ACS front-end. For example, if the comparison rate is set to 100 KHz, the maximum quantization bit Q can be 10. In order to focus on the performance of the proposed ACS front-end, the following analysis assumes that the CT-TE circuitry supports a maximum of 10-bit resolution.

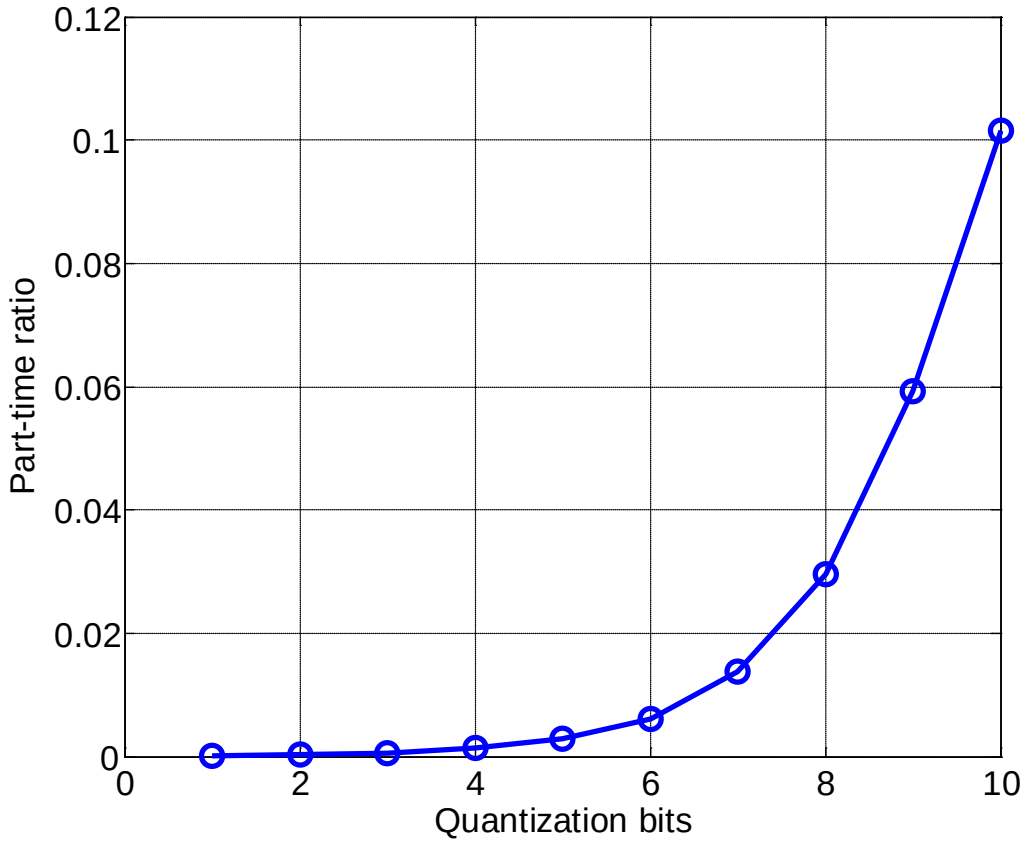

Fig. 14. The relationship between part-time ratio and quantization bits in the proposed ACS front-end for ECG signal.

As shown previously in Fig. 7, the number of significant variations increases as the quantization bit Q goes up due to the comparison window becoming narrow when Q goes large. The part-time randomization strategy discussed in the DRS-II is applicable to the zero-valued sections and thus it is informative to investigate the relationship between the part-time ratio and quantization bit. Fig. 14 shows that the part-time ratio or duty

cycle increases as Q increases due to the detection of small amplitude variations. As the resolution approaches the noise floor, this also increases the part-time ratio. However, even with 10-bit quantization, the part-time ratio is still around 0.1 for the typical ECG signal; suggesting a very efficient ACS front-end implementation.

The highly-digital ACS front-end provides multiple attractive properties for current and future applications. By replacing the dedicated analog modules in random demodulator, such as the mixer and integrator, with their digital counterparts, the ACS front-end will scale well with CMOS processes and provide increased robustness to nonlinearity and aperture effect. The primary advantage of the proposed ACS front-end compared to other digital-assisted CS hardware designs [67] results from the part-time randomization which optimizes the PN generator operation, which is typically the highest-power digital block. In [67], the accumulator keeps on active during the entire CS measurements generation. While in the ACS front-end, accumulator is shut down for all zero-valued sections. Instead, a counter working at the same rate is employed. If accumulator and counter in Fig. 11 have the similar toggling rate, they have comparable power consumption. Then, the reduced duty cycle of PN generator reduces the overall on-chip power consumption. The small part-time ratio result shown in Fig. 14 suggests the potential on power savings in the ACS front-end for pulsed-like input signal.

Focusing on the most significant amplitude variations in ECG signal, Fig. 15 illustrates the original QRS complex and its ternary timing signal $x[n]$ after the CT-TE scheme when $Q = 1$. As shown in Fig. 15, the sparse ternary-valued timing signal can be captured by the DRS-I or DRS-II efficiently at a low sampling rate.

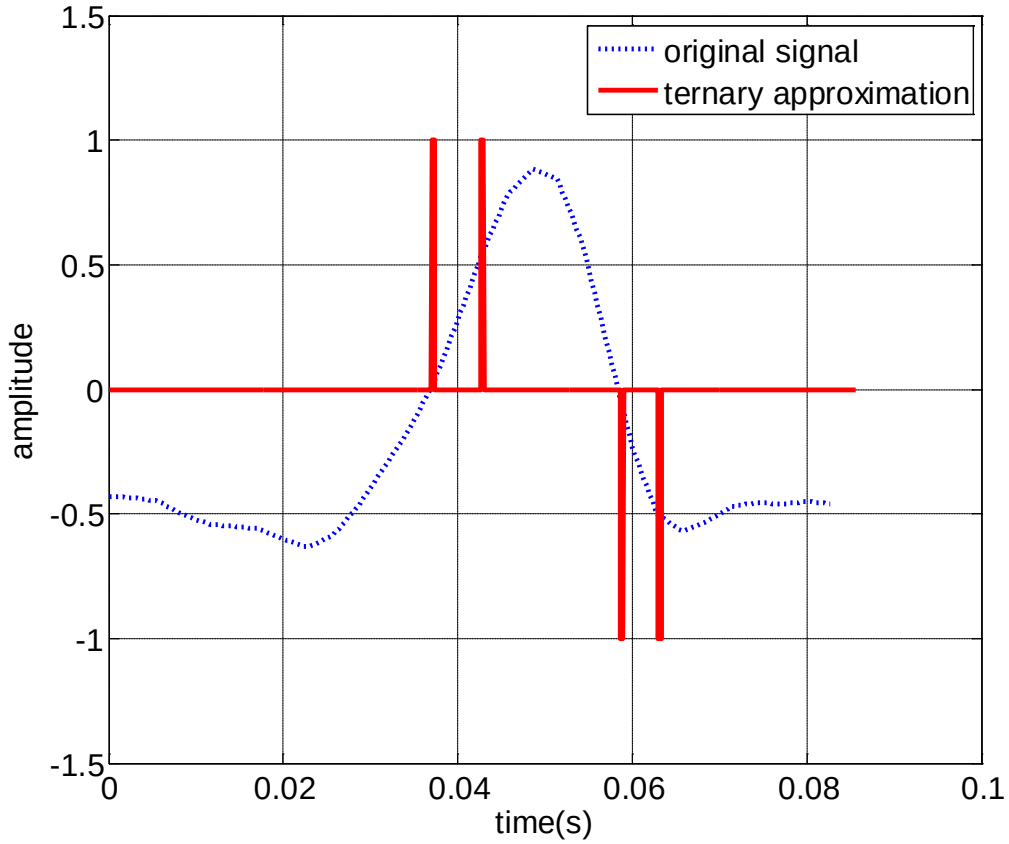

Fig. 15. Original signal waveform of QRS complex in ECG recording and its ternary approximation by 1-bit quantization in the CT-TE scheme.

III.E. Summary

In this chapter, we introduced the ACS front-end. Two essential building blocks, continuous-time ternary encoding (CT-TE) scheme and two types of digital random sampler (DRS) are discussed. The CT-TE scheme employs asynchronous sampling mechanism to convert amplitude variations into high-rate ternary timing signals. DRS captured the ternary timing signals at a sub-Nyquist rate by CS framework. The DRS-I has relatively low cost and is ideal for a massive integration. The DRS-II has a reduced duty cycle of energy-hungry circuits in CS measurements generation.

CHAPTER IV

GROUP-BASED TOTAL VARIATION*

In this chapter, we propose group-based total variation (GTV) for the ACS front-end. Algorithm descriptions and main theorem are presented. Numerical results are provided in the context of ECG recording in wireless body sensor networks (WBSN).

IV.A. Description

The ACS front-end in Chapter III firstly converts input amplitude variations into ternary timing information by the CT-TE scheme, and then employs DRS-I or DRS-II to capture the ternary timing signal or its equivalent compact signal at a sub-Nyquist rate, respectively. Both ternary timing signal and equivalent compact signal are piecewise-constant, which implies sparsity in the gradient domain. For illustration, Fig. 16 shows an example of an equivalent compact signal in the DRS-II and its first-order derivative.

Among many regularization terms on derivative function, total variation (TV) [68] shows some great potential, primarily due to its convexity, discontinuity tolerance and edge-preserving ability [69–73]. The standard TV regularization method was first introduced by Rudin-Osher and Fatemi in [68]. Various follow-ups were proposed that

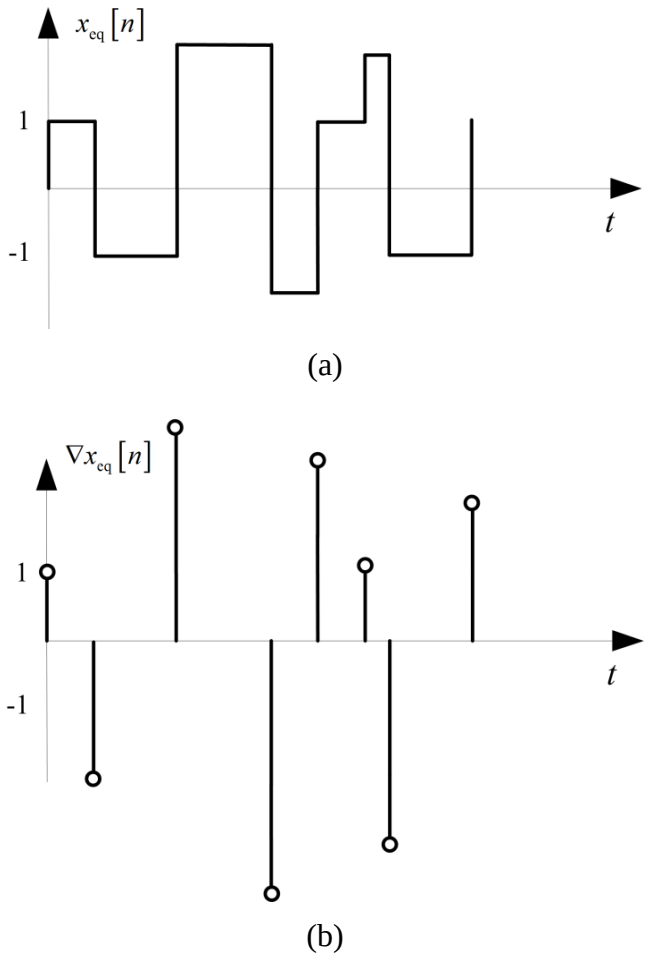

Fig. 16. An illustration of (a) piecewise-constant equivalent compact signal in the DRS-II, and (b) its first-order derivative.

either improved the signal recovery and/or extended the TV method to different kinds of signals [74–79]. Some recent work on the combination of TV framework and CS signal recovery have been reported for image restoration from incomplete samples [80–82].

However, the penalty term in most of existing TV methods mentioned above is element-based and neglected the internal signal structures. Leveraging on the piecewise-

constant characteristics of ternary timing signal, we introduce a group-based TV (GTV) penalty and so-called GTV signal reconstruction algorithm for the sparse signal recovery in this chapter. The idea comes from a fact that pulsed-like signals can be approximated by a piecewise-constant ternary timing signal after the CT-TE scheme processing. The GTV term in the penalty function offers additional benefits to the signal recovery from the incomplete and noise corrupted measurements.

IV.B. Main Theorem

The problem of conventional TV regularization can be formally formulated in Eq. (4.1) [68],

$$\hat{x} = \arg\min_x \left[\frac{1}{2} \left\| y - \mathbf{\Phi} x \right\|_2^2 + \alpha \mathrm{TV}\left(x \right) \right] \quad . \tag{4.1}$$

In (4.1), $\mathbf{\Phi}$ is sensing matrix which can be viewed as a bounded linear operator, and α is the regularized factor that controls the weight between the data fidelity term $\left\| y - \mathbf{\Phi} x \right\|_2^2$ and the TV term TV(x). TV(x) is defined as below,

$$\mathrm{TV}\left(x \right) = \int_\Omega \left| \nabla x \right| du \quad , \tag{4.2}$$

where Ω is feasible set of x. TV(x) measures the variations of x without penalizing the discontinuities, and is also capable of preserving edge information. As shown in (4.2), the conventional TV regularization is element-wise based in the feasible set. It neglects additional the piecewise-constant characteristics in the ternary timing signal output from the CT-TE scheme.

Before introducing the proposed group-based TV (GTV) scheme, we first define the concept of “group” adopted in the GTV algorithm.

Definition 4.1: *In the discrete setting, group is a collection of consecutive points that have the same quantized amplitude information.*

S-member means the maximum group size is *S*. Including both the inter-group and intra-group total variation of $x \in \mathbb{R}^N$, our goal is to minimize the objective function in (4.3) during the signal reconstruction.

$$J(x) = \alpha \mathrm{TV}(x) + \gamma \mathrm{GTV}(x, S) + \left\| y - \mathbf{\Phi} x \right\|_2^2 \quad . \tag{4.3}$$

Thus, we have the following optimization problem,

$$\min_x J(x) \quad , \tag{4.4}$$

subject to the following constraints,

$$\begin{aligned} &\mathrm{TV}(x) = \left\| Dx \right\|_1 \\ &\mathrm{GTV}(x, S) = \sum_{i=1}^{N} \left\| Dx_i^{i+S_i-1} \right\|_1 \\ &S_i = \min(S, g_i) \\ &g_i = \arg\max_g \left(\left\| Dx_i^{i+g} \right\|_\infty \le TH < \left\| Dx_i^{i+g+1} \right\|_\infty \right) \end{aligned} \quad . \tag{4.5}$$

where *D* is the gradient matrix, α and γ are tuning parameters that balance TV and GTV penalties, x_i^j means the string comprising samples *i* through *j* within *x*, g_i is the group size seeing from the i^{th} sample, and *TH* is the threshold for similarity.

We adopt the iteratively reweighted least squares (IRLS) method [83] in sparse recovery. As shown in [83], an l_p-norm ($p \ge 1$) can be approximated by the reweighted l_2-norm at each iteration step. Hence, the optimization problem (4.4) can be approximated by a least squares (LS) problem in each iteration. Note that, even with a linear problem in each iteration, the IRLS is highly nonlinear due to its adaptive algorithm nature.

Comparing with the conventional TV-based method, the *S*-GTV includes a new regularization term GTV(x, S) that measures the intra-group total variation. Since it's the summation of a set of l_1-norm terms, each one can be approximated independently. The difference lies in the weights calculation. In the proposed *S*-GTV scheme, each sample in x has S weights corresponding to its S neighbors. Depending on the limit of group size and signal characteristics, the actual number of neighbors involved in the group-based TV calculation may vary among different elements. Therefore, each point will find its neighbors depending on the criterion shown in (4.5). The *S*-GTV algorithm is described in **Algorithm 4.1** in Table 2.

In initialization, the weight series $W^j(i)$ for the j^{th} neighbor are set to 1, where i=1, 2, …, N and j=1, 2, …, S. In each iteration, an equivalent total variation W_{total} is calculated by least squares approximation. Note that W_{total} includes both the inter-group and intra-group total variation described in (4.5). By tuning the parameters α and γ, we can control the direction of optimization. Specifically, a smaller γ gives more freedom to the optimizer to seek the significant point-wise variations or local variations; while a larger γ leads the optimizer to the piecewise-constant sections or global variations.

It is worthy to point out the sparse recovery of problem (4.4) is $x_{\text{eq}}[n]$ rather than $x[n]$ when DRS-II is employed in the ACS front-end. After amplitude compensation, the equivalent compact signal ($a^*x_{\text{eq}}[n]$) should have integer-valued amplitude because both $\sum p_c$ and $T_{i\rightarrow i+1}$ are integers by default. Therefore, ($a^*x_{\text{eq}}[n]$) is rounded to integers to reconstruct the original ternary piecewise-constant signal $x[n]$. If the absolute amplitude of a certain piecewise-constant section is larger than 1, i.e. $|a^*x_{\text{eq}}[i]|>1$, it implies there is

a zero-valued section before it. Also, the length of that zero-valued section is equal to $|a^*x_{eq}[i]|$ with the same sign of $(a^*x_{eq}[i])$. For those sections with unit amplitude, they are copied to the output directly.

Accurate recovery of zero-valued sections is important, as a small error results in a shift of the peak (e.g. the QRS complex), and may cause a large overall reconstruction error. This work proposes two compensation techniques to ensure sufficient recovery performance. The first technique relies on the intra-group TV penalty in the *S*-GTV scheme. Recall that the iteration process in **Algorithm 4.1** starts from randomized measurements. It is reasonable to use a smaller γ in the first several iterations to figure out a "contour" of the piecewise-constant approximation. After that, a larger γ will help smooth out observation noise and simultaneously expedite the convergence rate. The second technique leverages the property that the PN generator clock rate is larger than the input Nyquist rate. If we have an H times higher clock rate, a single activity in the CT-TE scheme ("+1" or "-1") results in at least H discrete samples and each piecewise-constant section in $x(n)$ should have a minimum of H samples. As will be shown in next section numerical results, it is possible to correct some outliers in the reconstruction result with compensation.

Table 2. *S*-member group-based total variation

Algorithm 4.1: *S*-member Group-Based Total Variation

INPUT: randomization matrix $\mathbf{\Phi}$, received signal y, the threshold TH, the maximal group size S, the maximal iteration number $imax$, and the tuning parameters α and γ.

OUTPUT: the estimation of piecewise-constant signal $\hat{x}$

PROCEDURE:

1. Initialize the estimate signal $x_{t-1} = 0$, the weight $W_{t-1}^{j} = 1$ for j^{th} neighbor, and the iteration count $t = 1$.
2. **while** $t \leq imax$, **do**
3. Find the gradient of x, $x' = Dx$.
4. Perform thresholding, find group size for each sample,

   $g_i = \min\{S, \arg\max_{g} |x'^{i+g}_{i}|_\infty \leq TH < |x'^{i+g+1}_{i}|_\infty\}$.
5. Calculate the weight for the least squares approximation,

   $W_{\text{total}}(i) = \alpha D' W_{t-1}^{1}(i) D + \gamma \sum_{j=1}^{g_i} D_j' W_{t-1}^{j}(i) D_j$, where D_j is j-shifted gradient matrix.
6. Calculate the least squares solution for current iteration,

   $x_t = (\mathbf{\Phi}' * \mathbf{\Phi} + W_{\text{total}})^{-1} * \mathbf{\Phi}' y$
7. Update the weight of all neighbors, $W_t^j = 2*\text{diag}(1/D_j x_t)$
8. Increment t
9. **end while**
10. **return** $\hat{x} \leftarrow x_t$

IV.C. Numerical Results

In order to evaluate the sparse recovery of conventional TV-based methods and the *S*-GTV algorithm, a typical ECG signal from the MIT-BIH Arrhythmia Database [66] is used as a case study for illustration. In the following simulations, one complete cycle is simulated, and we utilize the QRS complex which represents the region with the most significant variations in an ECG signal. Here we define the Sub-Nyquist Sampling Ratio (SSR) in Eq. (4.6), where f_{Nyq} is the Nyquist rate and f_s is the actually sampling rate.

$$\text{SSR}=\frac{f_s}{f_{\text{Nyq}}} \quad . \tag{4.6}$$

Setting the SSR to 0.18, from Fig. 17 to Fig. 19, we shows the sparse recovery of the equivalent compact signal $x_{\text{eq}}[n]$ using the conventional TV method and the proposed *S*-GTV scheme at different signal-to-noise ratios (SNRs). In the noise-free case, Fig. 17 (a) shows that both the conventional TV method and the *S*-GTV scheme can exactly recover $x_{\text{eq}}[n]$. However, as shown in Fig. 17 (b), by evaluating the mean squared error (MSE) at each iteration step, the proposed *S*-GTV scheme exhibits a faster convergence relative to the conventional TV approach. This is because as the minimizer approaches to the optimum, the GTV term regularizes the objective function to a direction that favors the piecewise-constant estimation, expediting the convergence rate. In Fig. 17 (b), an error floor is observed in both the conventional TV and *S*-GTV scheme due to the small additive offset introduced in matrix inversion in Step 6 of **Algorithm 4.1** that ensures the inverse operation is tractable in the numerical calculation.

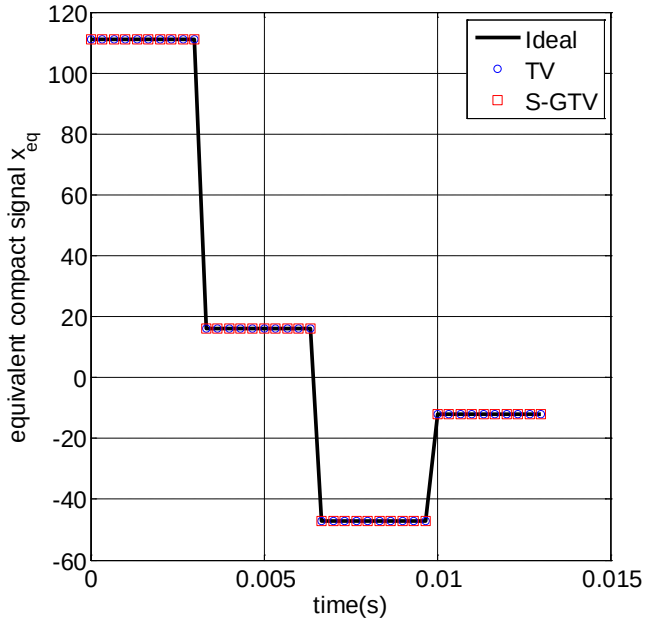

(a)

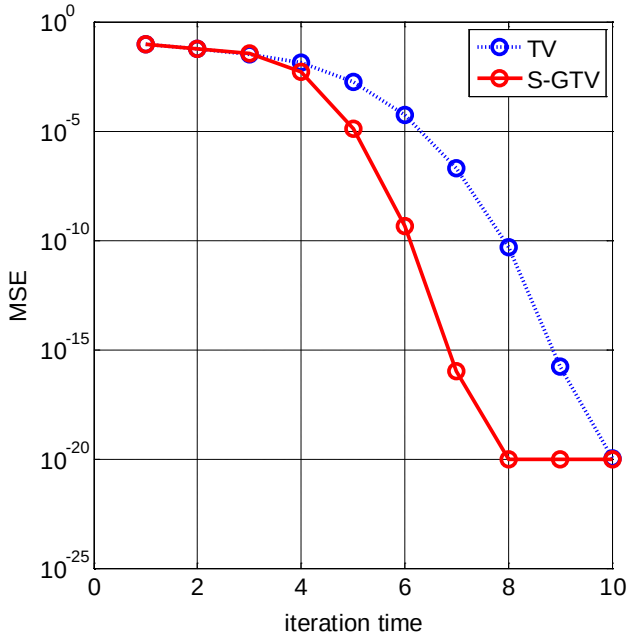

(b)

Fig. 17. Sparse recovery of piecewise-constant signal $x_{eq}[n]$ by TV-based method and *S*-GTV scheme in noise-free case. (a) Waveform recovery; (b) MSE versus iteration time.

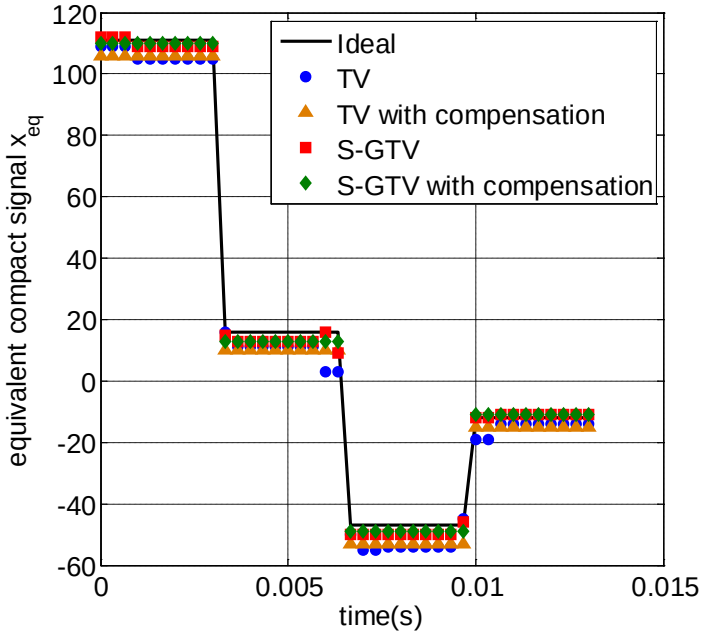

(a)

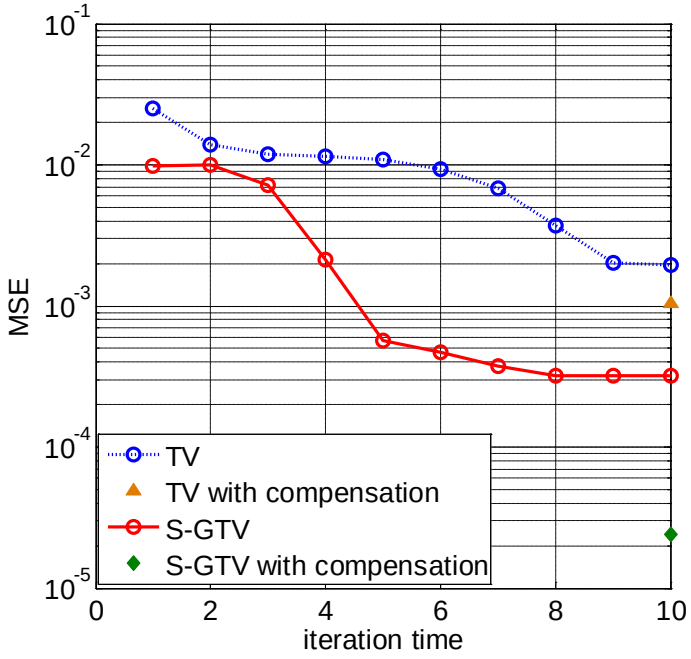

(b)

Fig. 18. Sparse recovery of piecewise-constant signal $x_{eq}[n]$ by TV-based method and *S*-GTV scheme when SNR=40dB. (a) Waveform recovery; (b) MSE versus iteration time.

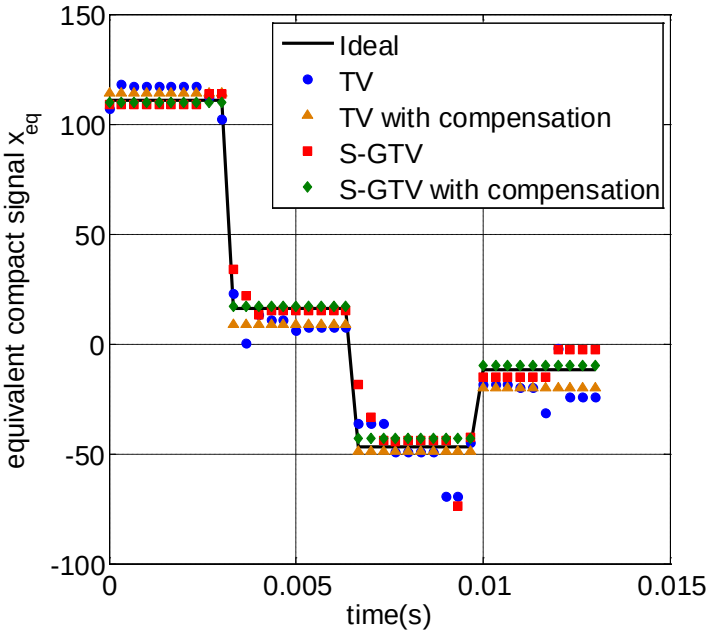

(a)

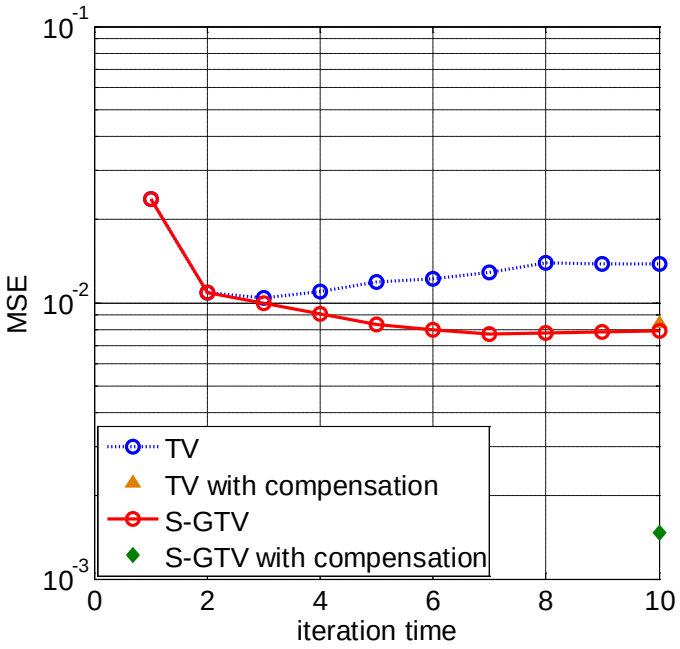

(b)

Fig. 19. Sparse recovery of piecewise-constant signal $x_{eq}[n]$ by TV-based method and *S*-GTV scheme when SNR=20dB. (a) Waveform recovery; (b) MSE versus iteration time.

Fig. 18 shows that the *S*-GTV algorithm exhibits better MSE performance in comparison to the conventional TV-based method when SNR decreases to 40dB. This difference results from the combination of intra-group and inter-group TV penalties in the *S*-GTV scheme. Although group TV penalty cannot eliminate outliers completely in the piecewise-constant sections due to noise, the proposed compensation techniques ensure an accurate recovery of the equivalent compact signal $x_{\text{eq}}[n]$. In Fig. 18, MSE displays an 11.3dB improvement with the *S*-GTV scheme with compensation.

Fig. 19 shows that both the conventional TV approach and the *S*-GTV algorithm have very limited MSE performance without compensation when noise increases to 20dB SNR. Compared to the conventional TV approach, the *S*-GTV scheme is good at recovering large piecewise-constant sections. While outliers do exist in the sparse recovery result, the *S*-GTV scheme with compensation is able to guarantee the demodulation process of ternary timing information. By exploiting the characteristics of the equivalent compact signal, we can roughly categorize the entire recovery into three groups: one group with amplitude less than -1, one group with amplitude larger than 1, and one that includes all others. For the first two groups, the amplitude of consecutive samples can be averaged, which represents the length of the zero-valued section before it. While for the third group, the amplitude is around 1 or -1.

Fig. 20 illustrates the sparse recovery with the compensation technique when SNR=20dB and the ideal noise-free case. These results suggest that the proposed *S*-GTV scheme achieves an accurate sparse signal recovery of ternary timing information with the compensation techniques. Once the ternary timing signal is obtained, the original

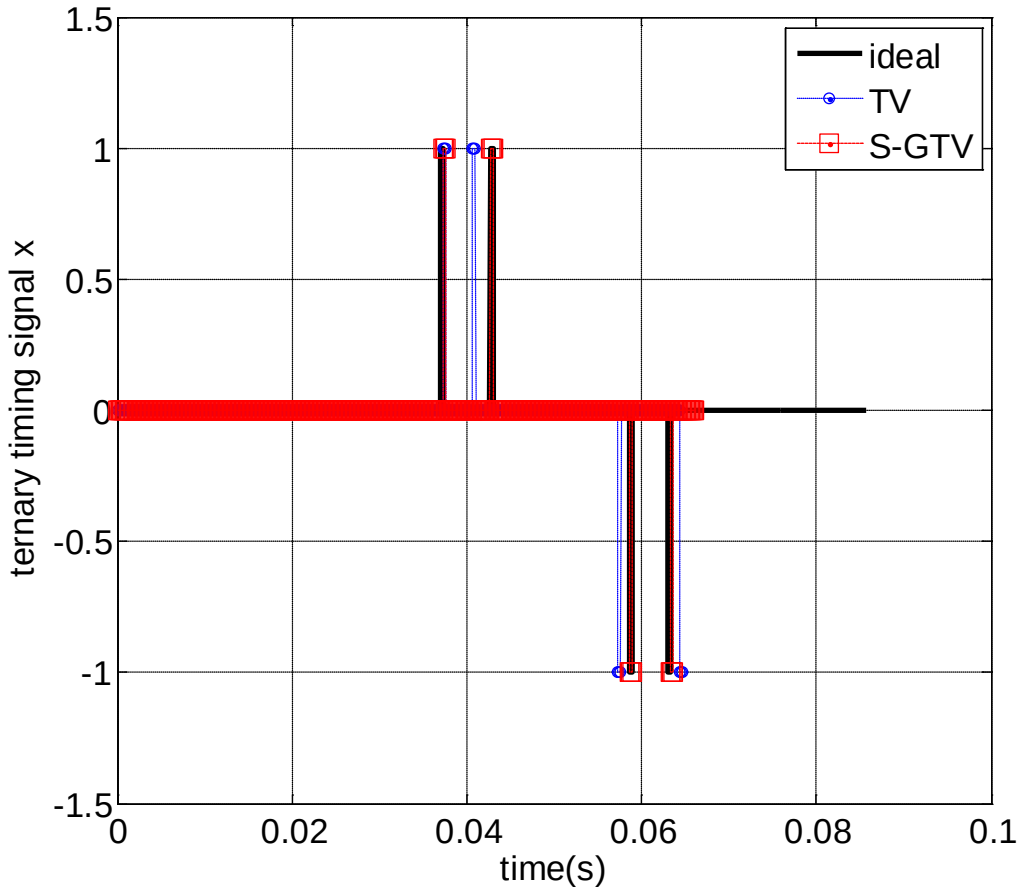

Fig. 20. Recovery of ternary timing signal $x[n]$ from the equivalent compact signal $x_{eq}[n]$ with compensation techniques.

signal can be reconstructed by integration followed by advanced smoothing techniques because of bandlimited ECG signal. For illustration, we adopt an accumulator for digital integration followed by low-pass filter (LPF) in the following simulations.

Fig. 21 shows the waveform reconstructions of the QRS complex by the ACS front-end with 3-bit and 5-bit CT-TE schemes, respectively. In the proposed ACS front-

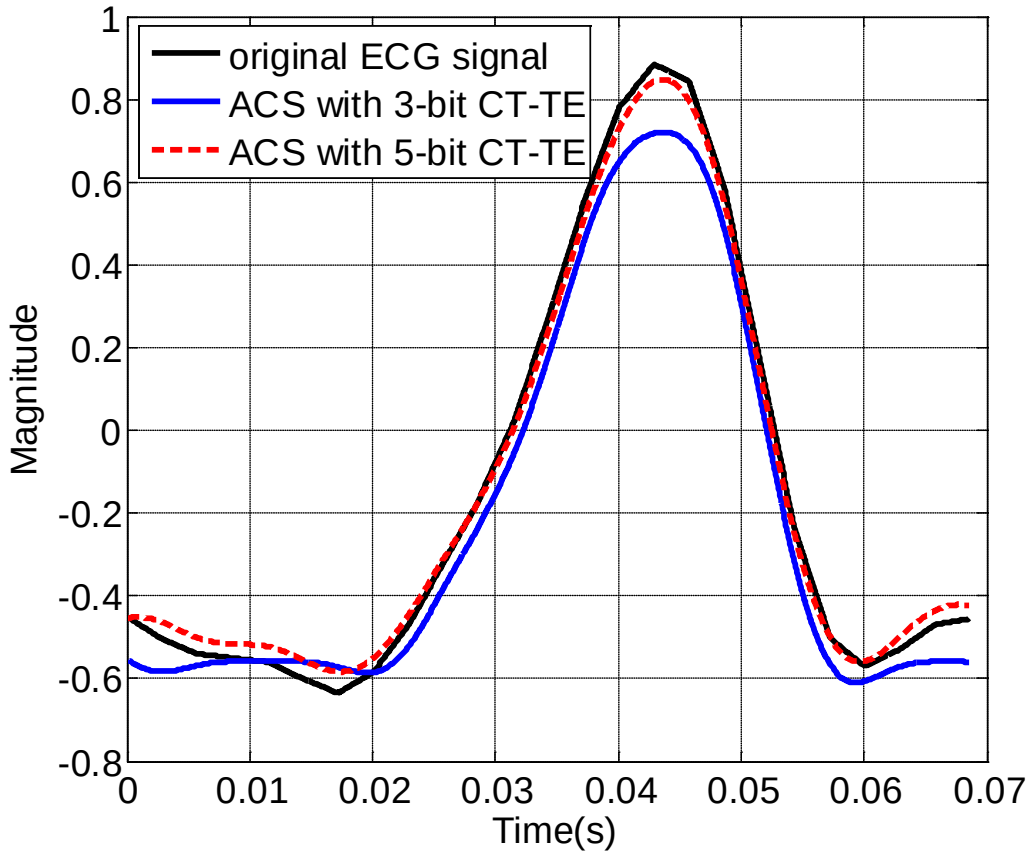

Fig. 21. Reconstruction of QRS complex waveform by the proposed ACS front-end with different number of quantization bits in the CT-TE scheme.

end, the CT-TE scheme also introduces quantization noise similar to the conventional ADCs. The differences between ideal ECG waveform and the reconstructed ones are caused by the quantization noise and observation noise. Increasing the CT-TE resolution improves the QRS waveform reconstruction. In Fig. 21, the MSE of reconstruction is

0.429 and 0.062 for 3-bit and 5-bit CT-TE scheme, respectively, with a SSR of 0.18, i.e. 6-fold data volume reduction compared with the Nyquist-rate sampling scheme.

Heart rate detection is a basic function in ECG recording systems and many heart diseases like arrhythmia can be identified from an abnormal heart rate. In Fig. 22, a sequence of 3 heart beat cycles is adopted to evaluate the heart rate detection with 3-bit and 5-bit CT-TE scheme in the ACS front-end when SSR is set to 0.18 and SNR is 20dB. As shown in Fig. 22, both the 3-bit CT-TE and 5-bit CT-TE scheme of the ACS front-end enable sub-Nyquist sampling with a CS technique and the sparse reconstructions provide reliable heart rate detection with a simple thresholding scheme. It is worthy to point out that the proposed ACS front-end can be initialized to 3-bit quantization to enable heart rate detection at a very low data rate, as suggested by Fig. 14, which shows the duty cycle reduction at different CT-TE resolution. Once an abnormal heart rate is identified, more quantization bits can be dynamically assigned to increase the resolution for further analysis. Such a need-based strategy increases the autonomy of the ACS front-end in an ECG recording system and optimizes the power consumption from a system perspective.

IV.D. Summary

We present the proposed group-based total variation (GTV) signal reconstruction scheme in this chapter. The newly introduced GTV penalty in the objective function provides better signal reconstruction and faster convergence rate when compared with conventional TV approach. The performance of GTV algorithm is studied in the ECG recording of wireless body sensor networks.

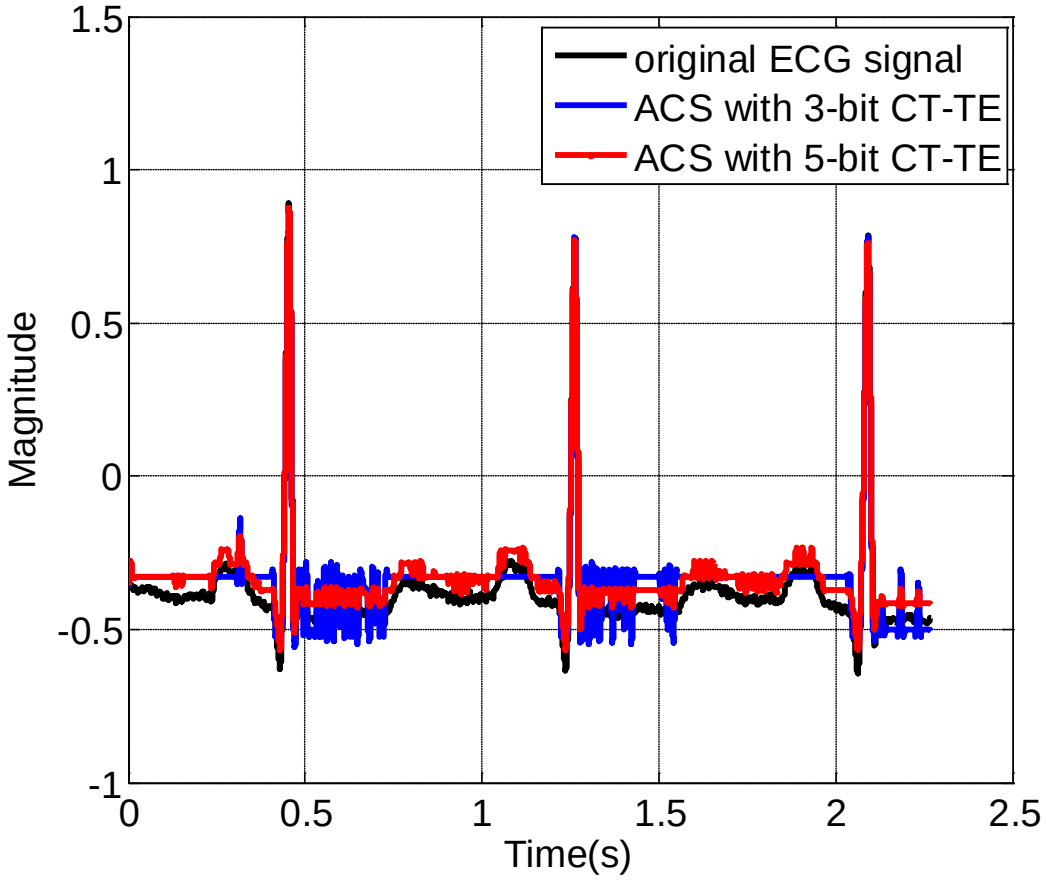

Fig. 22. Reconstruction of 3-cycle ECG waveform by the proposed ACS front-end with different number of quantization bits in the CT-TE scheme.

CHAPTER V

SPLIT-PROJECTION LEAST SQUARES

In this chapter, we present a low-complexity sparse signal reconstruction scheme called split-projection least squares (SPLS) for the proposed ACS front-end. Algorithm descriptions are provided in Section A. Main theorem, including derivations of statistics of the SPLS estimator and optimal threshold for ternary-valued amplitude detection is presented in Section B. Section C compares the computational complexity with state-of-the-art CS signal reconstruction schemes. And Section D discusses the hardware design. Numerical simulations are provided in Section E. Finally, Section F makes conclusions.

V.A. Description

In Chapter II, Section D, we briefly reviewed two popular signal reconstruction approaches in CS framework, i.e. basis pursuit and matching pursuit. Both approaches are equivalent to an l_1-norm optimization problem that is known to have computational complexity in polynomial time and probability guaranteed performance in the signal reconstruction. However, both of them have some known limitations. For example, greedy methods like matching pursuit are usually faster than convex relaxation and also friendly to some non-convex constraints. However, its performance is sensitive to heavy observation noise [51]. Basis pursuit is more noise robust. But the algorithm is generally much slower, and the computational cost is appreciably greater than direct processing of the Nyquist-rate samples. These drawbacks limit the CS technique to applications where both good noise robustness and low-cost real-time signal reconstruction are necessities,

for example, high-performance but low-power diagnostic ultrasound imaging and radar detection, etc.

Scrutiny to basis pursuit and matching pursuit reveals that they both are general signal recovery approaches and are applicable to any kind of sparse signals, structured or unstructured, without a requirement on knowledge of sparse signal support and/or amplitude. However, we do have a *prior* on the amplitude of ternary timing signal, i.e. {+1, 0, –1}, when the proposed CT-TE scheme is employed together with the DRS-I in the ACS front-end. The ternary amplitude *prior* motivates the development of following low-complexity split-projection least squares (SPLS) algorithm, which reconstructs the ternary timing signal from compressed measurements generated by the DRS-I.

V.B. Main Theorem

Let us denote x to be a K-sparse ternary signal from $\mathbb{R}^N$, and $y \in \mathbb{R}^M$ to be the CS measurements $y = \mathbf{\Phi}x + w$, where $\mathbf{\Phi}$ is an $M \times N$ ($M << N$) sensing matrix, $\mathbf{\Phi} = [\varphi_1, \varphi_2, \varphi_3, \ldots, \varphi_N]$, and φ_i denotes the i^{th} column of $\mathbf{\Phi}$. Here, w is Gaussian noise, $w \sim \mathcal{N}(0,\ \sigma^2)$.

Define a window Ω of length L to sweep along the columns of $\mathbf{\Phi}$. At each time, a windowed portion of the columns is selected. Let $\mathbf{\Phi}$ be split into (N/L) mutually exclusive sub-matrices,

$$\mathbf{\Phi} = \left(\mathbf{\Phi}^{(1)}, \mathbf{\Phi}^{(2)}, \cdots, \mathbf{\Phi}^{(N/L)}\right) \ . \tag{5.1}$$

For the i^{th} sub-matrix in (5.1), $\mathbf{\Phi}$ can be represented by two $M \times N$ matrices $\mathbf{\Phi}_{\Omega}^{(i)}$ and $\mathbf{\Phi}_{\bar{\Omega}}^{(i)}$ according to the specific window $\Omega = \{S, S+1, \ldots, S + L - 1\}$, $S \in [1, N - L+1]$. We drop the index i for convenience, then

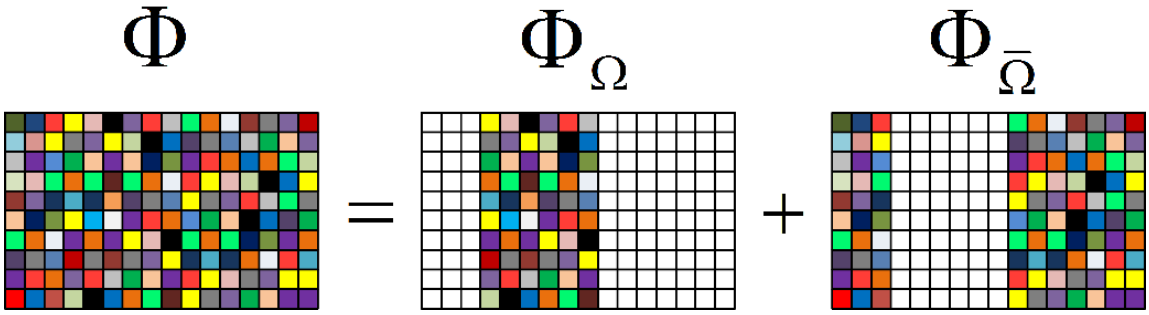

Fig. 23. An illustration of matrix splitting. A sensing matrix is split into two complementary matrices by a sweeping window.

$$\mathbf{\Phi} = \mathbf{\Phi}_{\Omega} + \mathbf{\Phi}_{\bar{\Omega}} \ , \tag{5.2}$$

$$\mathbf{\Phi}_{\Omega} = \begin{pmatrix} \mathbf{0}_{M\times(S-1)} & [\mathbf{B}_2]_{M\times L} & \mathbf{0}_{M\times(N-S-L+1)} \end{pmatrix} \ , \tag{5.3}$$

$$\mathbf{\Phi}_{\bar{\Omega}} = \begin{pmatrix} [\mathbf{B}_1]_{M\times(S-1)} & \mathbf{0}_{M\times L} & [\mathbf{B}_3]_{M\times(N-S-L+1)} \end{pmatrix} \ , \tag{5.4}$$

where sub-matrices $\mathbf{B}_1$, $\mathbf{B}_2$, and $\mathbf{B}_3$ are formed from the columns of $\mathbf{\Phi}$ according to Ω. Fig. 23 illustrates a matrix is split into two complementary matrices by a window.

Similarly, we also segment x based on Ω, yielding

$$x = \begin{pmatrix} [x_1^T]_{1\times(S-1)} & [x_2^T]_{1\times L} & [x_3^T]_{1\times(N-S-L+1)} \end{pmatrix}^T \ . \tag{5.5}$$

Combining Eqs. (5.2)-(5.5), the measurement can be rewritten as, shown in Fig. 24.

$$y = \mathbf{B}_2 x_2 + \left(\mathbf{B}_1 x_1 + \mathbf{B}_3 x_3\right) + w \ , \tag{5.6}$$

At each time, the windowed unknowns in x_2 are estimated. Note that $\mathbf{\Phi}$ has full column rank due to the RIP constraint on the sensing matrix [24]. $\mathbf{B}_2^T\mathbf{B}_2$ is invertible when $L \leq M$. The first derivative of the log-likelihood function with respect to x_2 is,

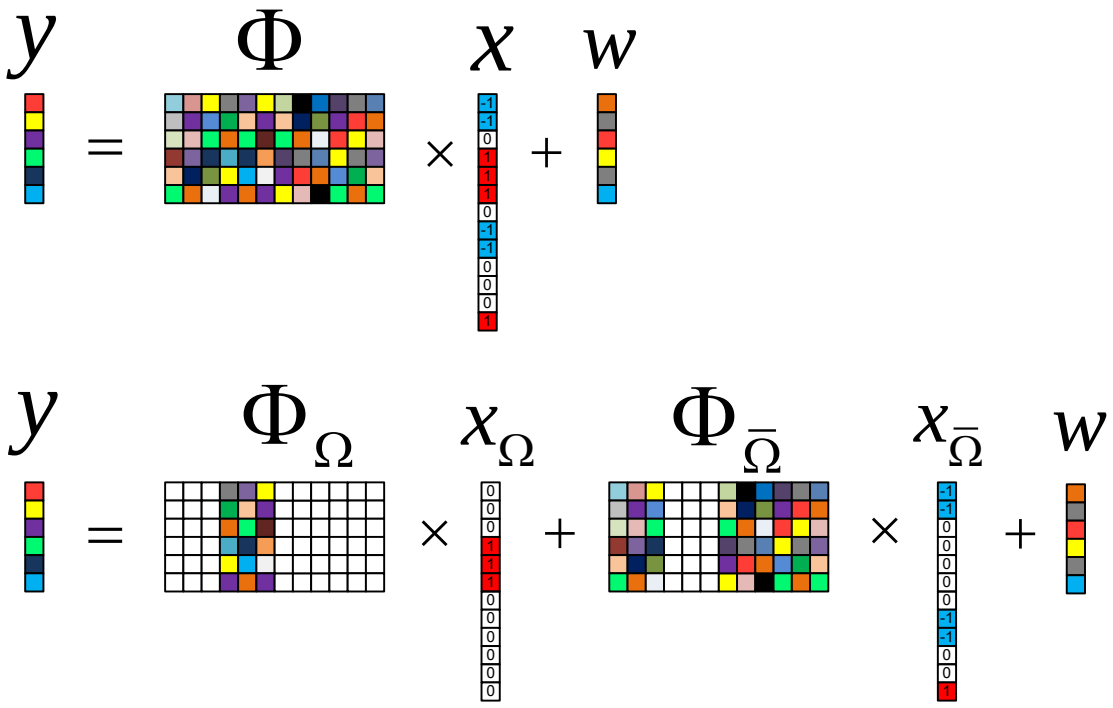

Fig. 24. An illustration of split projection on sensing matrix in the CS front-end.

$$\frac{\partial \ln \Pr\left(y; x_2\right)}{\partial x_2} = \frac{\mathbf{B}_2^T \mathbf{B}_2}{\sigma^2} \cdot \left\{ \left(\mathbf{B}_2^T \mathbf{B}_2\right)^{-1} \mathbf{B}_2^T y - \tilde{x}_2 \right\} \quad , \tag{5.7}$$

where $\tilde{x}_2 = x_2 + (\mathbf{B}_2^T \mathbf{B}_2)^{-1} \mathbf{B}_2^T (\mathbf{B}_1 x_1 + \mathbf{B}_3 x_3)$ is the expectation of the estimator $\hat{x}_2 = (\mathbf{B}_2^T \mathbf{B}_2)^{-1} \mathbf{B}_2^T y$. Note that if $\mathbf{B}_2^T \mathbf{B}_1$ and $\mathbf{B}_2^T \mathbf{B}_3$ are 0, or x_1 and x_3 are 0, the proposed SPLS estimator becomes a minimum-variance unbiased (MVU) estimator, which is unbiased and whose variance achieves the Cramér–Rao Lower Bound (CRLB), well known to be,

$$\mathrm{CRLB}\left(\hat{x}_2\right) = \left(I_{x_2}\right)^{-1}, \quad \text{where } I_{x_2} = \sigma^2 \left(\mathbf{B}_2^T \mathbf{B}_2\right)^{-1} \quad . \tag{5.8}$$

Table 3. Split-projection least squares (SPLS)

Algorithm 5.1: Split-Projection Least Squares (SPLS)

INPUT: sensing matrix $\mathbf{\Phi}$, compressed signal y, the length of window L, and the dimension of input sparse signal N.

OUTPUT: the estimate of input sparse signal $\hat{x}$

PROCEDURE:

1. Initialize the first split by setting S=1. The column indexes in the window is Ω=$\{S, S+1,\ldots, S+L-1\}$, and initialize the estimate of input signal $\hat{x} = \emptyset$.
2. **while** $S < N$
3. Draw sub-matrix $\mathbf{B}_2$ from $\mathbf{\Phi}$ based on the window Ω.
4. Obtain the SPLS estimate, $\hat{x}_2 = (\mathbf{B}_2^T\mathbf{B}_2)^{-1}\mathbf{B}_2^T y$.
5. Amplitude detection, $\bar{x}_2 = \mathrm{TH}(\hat{x}_2)$
6. Prune interference, $y = y - \mathbf{B}_2\bar{x}_2$.
7. Stack the section estimate, $\hat{x} = [\hat{x};\ \bar{x}_2]$.
8. Update the starting point of window, $S = S + L$.
9. **end while and return** $\hat{x}$

Equation (5.8) assumes all nonzero signal elements fall inside of the window Ω. It is generally not true. We continue the discussion for when $\mathbf{B}_2^T\mathbf{B}_1$ and $\mathbf{B}_2^T\mathbf{B}_3$ are not 0, or x_1 and x_3 are not 0 in next section. The entire signal estimate is formed by stacking each section estimate along the signal dimension. Note that each section estimate is non-

adaptive, and they are independent to each other, which is fundamentally different from the iteratively reweighted least squares (IRLS) algorithm [83]. The independence of each section recovery enables a fully parallel architecture in hardware implementation for real-time signal reconstruction. To further lower down interference from the nonzero elements outside of the projection window, we may prune the detected nonzero elements (interference) from the measurements before the recovery of remaining sections, as shown in Step 6 in Table 3, **Algorithm 5.1**. We will compare the performance difference of the SPLS algorithm with and without interference prune in Section E.

V.C. Statistics of the Estimator

In general, $\mathbf{B}_2^T\mathbf{B}_1$ and $\mathbf{B}_2^T\mathbf{B}_3$ are not 0, or x_1 and x_3 are not 0. Let $\mathbf{B}_2$ be $M\times L$, $\mathbf{B}_1$ be $M\times P$, $\mathbf{B}_3$ be $M\times R$, where $N = L+P+R$.

Suppose $\mathbf{\Phi}$ is taken from a Gaussian process, $\mathbf{\Phi} \sim \mathcal{N}(0,\ \sigma_\Phi^2)$. According to (5.7), the SPLS estimator is biased in general due to the interference from nonzero elements outside of the split projection window. However, incoherent sampling principle in the CS framework constrains the absolute value of any two different column inner products in the sensing matrix $\mathbf{\Phi}$. We adopt a conservative assumption for analysis, given by,

$$\left\langle \varphi_i, \varphi_j \right\rangle = \begin{cases} M\sigma_\Phi^2, & \text{if } i = j \\ d_{ij}\varepsilon, & \text{if } i \neq j \end{cases}, \tag{5.9}$$

where ε is a small value, and $d_{ij} = \pm 1$ is the sign indicator for correlation. Suppose $\mathbf{\Phi}$ is taken from a Gaussian process, i.e., $\mathbf{\Phi} \sim \mathcal{N}(0,\ \sigma_\Phi^2)$. In [84], the authors have shown the product of two independent Gaussian variables, $Z = XY$, $X\sim\mathcal{N}(0,\sigma_X^2)$, $Y\sim\mathcal{N}(0,\sigma_Y^2)$, has the following distribution,

$$f_Z(Z) = \frac{2Z}{\pi\sigma_X^2\sigma_Y^2} \cdot K_0\left(\frac{2Z}{\sigma_X\sigma_Y}\right) \quad , \tag{5.10}$$

where $K_0(Z)$ is the first kind modified Bessel function with order 0. The expectation and variance of the product are also given by [84],

$$E(Z) = 0 \qquad \mathrm{Var}(Z) = \sigma_X^2\sigma_Y^2$$

Therefore, $\mathbf{B}_2^T\mathbf{B}_2$ can be rewritten as,

$$\mathbf{B}_2^T\mathbf{B}_2 = \begin{pmatrix} M\sigma_\Phi^2 & & d_{ij}^{22}\varepsilon \\ & \ddots & \\ d_{ij}^{22}\varepsilon & & M\sigma_\Phi^2 \end{pmatrix}$$

$$= M\sigma_\Phi^2 \cdot \mathbf{I}_L + \varepsilon(\mathbf{1}_L - \mathbf{I}_L) \otimes \mathbf{D}^{2,2} \quad , \tag{5.11}$$

where $\mathbf{I}_L$ is $L \times L$ identify matrix, $\mathbf{1}_L$ is an $L \times L$ matrix with all elements equal to 1, $\mathbf{D}^{2,2}$ is the sign indicator matrix for the matrix product of $\mathbf{B}_2^T$ and $\mathbf{B}_2$, and $\otimes$ denotes element-wise matrix multiplication. The inverse of Eq. (5.11) is

$$\begin{aligned} \left(\mathbf{B}_2^T\mathbf{B}_2\right)^{-1} &= \left[M\sigma_\Phi^2 \cdot \mathbf{I}_L + \varepsilon(\mathbf{1}_L - \mathbf{I}_L) \otimes \mathbf{D}^{2,2}\right]^{-1} \\ &= \left[\mathbf{I}_L + \frac{\varepsilon}{M\sigma_\Phi^2}(\mathbf{1}_L - \mathbf{I}_L) \otimes \mathbf{D}^{2,2}\right]^{-1} \cdot \left(M\sigma_\Phi^2 \cdot \mathbf{I}_L\right)^{-1} \\ &= \left[\mathbf{I}_L + \frac{\varepsilon}{M\sigma_\Phi^2}(\mathbf{1}_L - \mathbf{I}_L) \otimes \mathbf{D}^{2,2}\right]^{-1} \cdot \frac{1}{M\sigma_\Phi^2}\mathbf{I}_L \\ &\approx \left[\mathbf{I}_L - \frac{\varepsilon}{M\sigma_\Phi^2}(\mathbf{1}_L - \mathbf{I}_L) \otimes \mathbf{D}^{2,2}\right] \cdot \frac{1}{M\sigma_\Phi^2}\mathbf{I}_L \quad . \end{aligned} \tag{5.12}$$

The last approximation is valid for small ε, because

$$\left[\frac{\varepsilon}{M\sigma_\Phi^2}(\mathbf{1}_L - \mathbf{I}_L) \otimes \mathbf{D}^{2,2}\right]^n \to \mathbf{0}, \text{ as } n \to \infty$$

Similarly for $\mathbf{B}_2^T\mathbf{B}_1$ and $\mathbf{B}_2^T\mathbf{B}_3$, we have the expectation of the SPLS estimator,

$$\begin{aligned} E\left(\hat{x}_2\right) &= x_2 + \left(\mathbf{B}_2^T\mathbf{B}_2\right)^{-1}\mathbf{B}_2^T\left(\mathbf{B}_1 x_1 + \mathbf{B}_3 x_3\right) \\ &= x_2 + \frac{1}{M\sigma_\Phi^2}\cdot\left[\mathbf{I}_L - \frac{\varepsilon}{M\sigma_\Phi^2}\left(\mathbf{1}_L - \mathbf{I}_L\right)\otimes\mathbf{D}^{2,2}\right]\cdot\left(\varepsilon\cdot\mathbf{D}_{L\times P}^{2,1}\cdot x_1 + \varepsilon\cdot\mathbf{D}_{L\times Q}^{2,3}\cdot x_3\right) \\ &= x_2 + \frac{\varepsilon}{M\sigma_\Phi^2}\left(\mathbf{D}_{L\times P}^{2,1}x_1 + \mathbf{D}_{L\times Q}^{2,3}x_3\right) + O\left(\varepsilon^2\right) \\ &\le x_2 + \frac{\varepsilon}{M\sigma_\Phi^2}\left(\left|x_1\right|_0 + \left|x_3\right|_0\right) + O\left(\varepsilon^2\right) \quad . \end{aligned} \tag{5.13}$$

Therefore, with projection window Ω, the expectation bias is upper-bounded by

$$\left|E\left(\hat{x}_\Omega\right) - x_\Omega\right| \le \frac{\varepsilon}{M\sigma_\Phi^2}\cdot\left|x_{\bar{\Omega}}\right|_0 + O\left(\varepsilon^2\right) \quad . \tag{5.14}$$

For small ε, the expectation of the SPLS estimator is asymptotically approaching the true value x_2 or x_Ω as M increases.

We now analyze the covariance of the SPLS estimator which is expressed by,

$$\begin{aligned} \mathrm{COV}\left(\hat{x}_2\right) = \left(\mathbf{B}_2^T\mathbf{B}_2\right)^{-1}\mathbf{B}_2^T\cdot E(&\mathbf{B}_1 x_1 x_1^T\mathbf{B}_1^T + \mathbf{B}_3 x_3 x_3^T\mathbf{B}_3^T + \mathbf{B}_1 x_1 x_3^T\mathbf{B}_3^T \\ &+ \mathbf{B}_3 x_3 x_1^T\mathbf{B}_1^T + ww^T)\cdot\mathbf{B}_2\left(\mathbf{B}_2^T\mathbf{B}_2\right)^{-1} \end{aligned} \quad . \tag{5.15}$$

The terms, $E(\mathbf{B}_1 x_1 x_1^T\mathbf{B}_1^T)$, $E(\mathbf{B}_3 x_3 x_3^T\mathbf{B}_3^T)$, $E(\mathbf{B}_1 x_1 x_3^T\mathbf{B}_3^T)$, and $E(\mathbf{B}_3 x_3 x_1^T\mathbf{B}_1^T)$ are all $M\times M$, representing the contribution of the nonzero elements outside of the chosen window to the CS measurements. Two extreme cases are considered to derive the upper and lower bounds of the covariance for a K-sparse input.

(1) All K nonzero elements fall inside of the window Ω.

In this case, the SPLS estimator is MVU as shown in (5.8), and it follows that,

$$\mathrm{COV}\left(\hat{x}_2\right) = \left(\mathbf{B}_2^T\mathbf{B}_2\right)^{-1}\mathbf{B}_2^T\cdot\mathbf{I}_{M\times M}\cdot\sigma^2\cdot\mathbf{B}_2\left(\mathbf{B}_2^T\mathbf{B}_2\right)^{-1}$$

$$= \frac{\sigma^2}{M\sigma_\Phi^2} \cdot \left[\mathbf{I}_L - \frac{\varepsilon}{M\sigma_\Phi^2} (\mathbf{1}_L - \mathbf{I}_L) \otimes \mathbf{D}^{2,2} \right] \quad . \tag{5.16}$$

(2) All K nonzero elements fall outside of the window Ω.

Without losing generality, we assume that there are k_1 and k_3 nonzero elements in x_1 and x_3, respectively, with $k_1 + k_3 = K$. Let supp$\{x_1\}$ denote the indices of nonzero elements in x_1. The cardinality of supp$\{x_1\}$, |supp$\{x_1\}$|, is k_1. Now, consider

$$\begin{aligned}
& E\left(\mathbf{B}_1 x_1 x_1^T \mathbf{B}_1^T\right) \\
&= E\left[\left(\mathbf{B}_1 x_1\right) \cdot \left(\mathbf{B}_1 x_1\right)^T \right] \\
&= E\left[\sum_{i \in \text{supp}\{x_1\}} \varphi_i x[i] \cdot \sum_{j \in \text{supp}\{x_1\}} \varphi_j^T x[j] \right] \\
&= \sum_{\substack{i,j \in \text{supp}\{x_1\} \\ i=j}} \varphi_i \varphi_i^T E\left(x^2[i]\right) + \sum_{\substack{i,j \in \text{supp}\{x_1\} \\ i \neq j}} \varphi_i \varphi_j^T E\left(x[i]x[j]\right) \\
&= \sum_{\substack{i,j \in \text{supp}\{x_1\} \\ i=j}} \varphi_i \varphi_i^T + \sum_{\substack{i,j \in \text{supp}\{x_1\} \\ i \neq j}} \varphi_i \varphi_j^T E\left(x[i]x[j]\right) \quad .
\end{aligned} \tag{5.17}$$

The last equation holds for ternary output as adopted in the ACS front-end with DRS-I. The derivation above can be extended to the general case when x comes from a finite set, such as QPSK, 16-QAM, and so on. We have,

$$E\left(\mathbf{B}_1 x_1 x_1^T \mathbf{B}_1^T\right) = k_1 \sigma_\Phi^2 \left[\mathbf{I}_L + \frac{\varepsilon}{M\sigma_\Phi^2} (\mathbf{1}_L - \mathbf{I}_L) \otimes \mathbf{D}^{1,1} \right] \quad . \tag{5.18}$$

Equation (5.18) holds if x has 0 mean. Similarly,

$$E\left(\mathbf{B}_3 x_3^T x_3 \mathbf{B}_3^T\right) = k_3 \sigma_\Phi^2 \left[\mathbf{I}_L + \frac{\varepsilon}{M\sigma_\Phi^2} (\mathbf{1}_L - \mathbf{I}_L) \otimes \mathbf{D}^{3,3} \right]$$

$$E\left(\mathbf{B}_1 x_1^T x_3 \mathbf{B}_3^T\right) = E\left(\mathbf{B}_3 x_3^T x_1 \mathbf{B}_1^T\right) = \mathbf{0}$$

Therefore, the covariance of the SPLS estimator is

$$\mathrm{COV}\left(\hat{x}_2\right)=\left[\left(K\sigma_{\Phi}^2+\sigma^2\right)\mathbf{I}_L+\frac{\varepsilon}{M}\left(\mathbf{1}_L-\mathbf{I}_L\right)\otimes\left(k_1\mathbf{D}^{1,1}+k_3\mathbf{D}^{3,3}\right)\right]\cdot \frac{1}{M\sigma_{\Phi}^2}\left[\mathbf{I}_L-\frac{\varepsilon}{M\sigma_{\Phi}^2}\left(\mathbf{1}_L-\mathbf{I}_L\right)\otimes\mathbf{D}^{2,2}\right]$$

$$=\frac{K\sigma_{\Phi}^2+\sigma^2}{M\sigma_{\Phi}^2}\cdot\mathbf{I}_L-O\left(\varepsilon^2\right)\ . \tag{5.19}$$

Based on Eq. (5.19), the variance of the SPLS estimator for the case when there are k nonzeros outside of the window is,

$$\mathrm{Var}\left(\hat{\theta}\right)=\frac{k\sigma_{\Phi}^2+\sigma^2}{M\sigma_{\Phi}^2},\ \text{ where } k\in\left[0,K\right].\ . \tag{5.20}$$

Therefore, the variance of the SPLS estimator is bounded by

$$\frac{\sigma^2}{M\sigma_{\Phi}^2}\le\mathrm{Var}\left(\hat{x}\right)\le\frac{K\sigma_{\Phi}^2+\sigma^2}{M\sigma_{\Phi}^2}\ , \tag{5.21}$$

where K is the number of nonzero elements in x.

We perform amplitude detection on the estimate $\hat{x}$ to exploit its ternary structure, i.e. $x\in\{-1, 0, 1\}$. We derive an appropriate threshold in the following. With Gaussian noise, p estimates of x, $(x)_1$, $(x)_2$, $(x)_3$, … , $(x)_p$, are normal with mean $\bar{x}_p$, and standard deviation Std(x_p). Consider the t-value given by [85], [86],

$$t=\frac{\bar{x}_p-x}{\mathrm{Std}\left(x_p\right)/\sqrt{p}}\ . \tag{5.22}$$

The new test statistic t in Eq. (5.22) follows a Student's t-distribution with $(p-1)$ degree of freedom. The probability density function of t is

$$\Pr(t) = \frac{\Gamma\left(\frac{p}{2}\right)}{\sqrt{(p-1)\pi}\,\Gamma\left(\frac{p-1}{2}\right)}\left(1+\frac{t^2}{p-1}\right)^{-\frac{p}{2}} \quad , \tag{5.23}$$

where Γ is the gamma function. A number T_α can be chosen to have a $100(1-\alpha)\%$ confidence interval, i.e., $\Pr(-T_\alpha < t < T_\alpha) = 1-\alpha$,

$$\Pr\left(\overline{x}_p - T_\alpha \cdot \frac{\mathrm{Std}(x_p)}{\sqrt{p}} < x < \overline{x}_p + T_\alpha \cdot \frac{\mathrm{Std}(x_p)}{\sqrt{p}}\right) = 1-\alpha \quad . \tag{5.24}$$

The endpoints of this confidence interval and the resulting optimal thresholds *TH* for hypothesis testing are then obtained as

$$TH = \overline{x}_p \pm T_\alpha \cdot \frac{\mathrm{Std}(x_p)}{\sqrt{p}} \quad . \tag{5.25}$$

V.D. Complexity and Hardware

As shown in **Algorithm 5.1**, the SPLS scheme yields an over-determined least squares (LS) problem in each section estimate, which offers good noise robustness as will be demonstrated in numerical simulations in Section E. The SPLS scheme achieves low complexity as shown in Table 4, where various state-of-the-art CS estimators, such as basis pursuit [24], orthogonal matching pursuit (OMP) [42], stage-wise OMP (StOMP) [44], Bayesian compressive sensing (Bayesian CS) [54] and smoothed-L0 [55] are compared. The SPLS estimator has three matrices multiplications with complexity of $O(ML^2)$, $O(L^2)$, $O(ML)$, respectively, and one matrix inverse calculation of complexity of $O(L^3)$. Noting that $M << N$ and $L < M$, the complexity of the SPLS estimator is $O(NML)$, which exhibits a low computational complexity among state-of-the-art CS

Table 4. Complexity comparison of state-of-the-art CS signal reconstruction algorithms.

Algorithm Name	**Computational Complexity**
l_0 optimization	NP hard
Basis Pursuit (BP)	$O(N^3)$
Orthogonal Matching Pursuit (OMP)	$O(NK^2)$
Stage-wise OMP (StOMP)	$O(N\log(N))$
Bayesian CS (BCS)	$O(NM^2)$
Smoothed-L0 (SL0)	$O(N^2)$
Split-Projection Least Squares (SPLS)	$O(NML)$

estimators. Note that the SPLS algorithm is not a general CS signal reconstruction algorithm, being specialized to sparse ternary-valued signals, which enables the low complexity reconstruction. In this paper, these ternary-valued signals are output of the DRS-I in the ACS front-end. It's worthy to point out that some other time-to-information conversion schemes also have ternary-valued outputs, such as time encoding machine (TEM) [58], Delta modulation [59], and integrate-and-fire scheme [60], to name a few.

Fig. 25 provides the block diagram of the SPLS scheme, where multiple parallel least squares (LS) estimators are employed to offer a good balance between complexity and real-time processing requirements. This is a unique feature in the SPLS scheme enabled by the independence between each window-based section recovery. In addition,

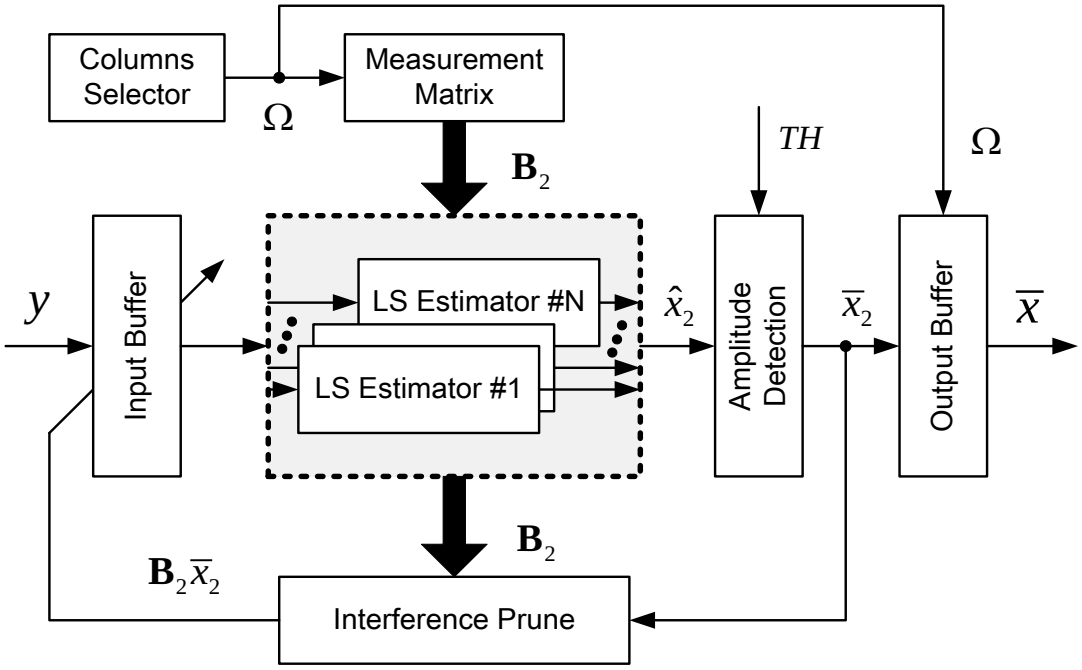

Fig. 25. Block diagram of the SPLS signal reconstruction scheme.

the recovered sections are used to prune the interference in estimating the remaining sections.

LS estimator is the most computation-intensive block in Fig. 25, which involves multiple matrix multiplications and one matrix inversion. Due to the RIP condition, the matrix for inversion is Hermitian and positive-definite. In literature, some popular very-large-scale integration (VLSI) architectures for inversion of a Hermitian, positive-definite matrix include QR decomposition [87], Cholesky decomposition [88], etc. We are inspired by the recent work in large-scale multiple-input multiple-output (MIMO)

system [89] that our matrix $\mathbf{A} = \mathbf{B}_2^T \mathbf{B}_2$ has a main diagonal and small value on all off-diagonal elements. It motivates the following *k*-term approximation to matrix inversion.

Let us define **A** = **D**+**E**, where **D** is diagonal matrix and **E** is off-diagonal matrix. We have the following Eq. (5.26) if $\mathbf{E}^n \to 0$, when $n \to \infty$.

$$\begin{aligned} \mathbf{A}^{-1} &= \left(\mathbf{D}+\mathbf{E}\right)^{-1} \\ &= \left[\mathbf{D}\left(\mathbf{I}+\mathbf{D}^{-1}\mathbf{E}\right)\right]^{-1} \\ &= \left(\mathbf{I}+\mathbf{D}^{-1}\mathbf{E}\right)^{-1}\mathbf{D}^{-1} \\ &= \sum_{n=0}^{\infty}\left(-\mathbf{D}^{-1}\mathbf{E}\right)^n \mathbf{D}^{-1} \quad . \end{aligned} \tag{5.26}$$

Denote the *k*-term approximation as

$$\tilde{\mathbf{A}}_k^{-1} = \sum_{n=0}^{k-1}\left(-\mathbf{D}^{-1}\mathbf{E}\right)^n \mathbf{D}^{-1} \quad . \tag{5.27}$$

As an example, we have $\tilde{\mathbf{A}}_1^{-1} = \mathbf{D}^{-1}$ for 1-term approximation. And for 2-term approximation, it is $\tilde{\mathbf{A}}_2^{-1} = \mathbf{D}^{-1} - \mathbf{D}^{-1}\mathbf{E}\mathbf{D}^{-1}$.

The residual error due to a general *k*-term approximation is

$$\begin{aligned} \Theta_k &= \sum_{n=k}^{\infty}\left(-\mathbf{D}^{-1}\mathbf{E}\right)^n \mathbf{D}^{-1} \\ &= \frac{\left(-\mathbf{D}^{-1}\mathbf{E}\right)^k}{1+\mathbf{D}^{-1}\mathbf{E}}\mathbf{D}^{-1} \\ &= \left(-\mathbf{D}^{-1}\mathbf{E}\right)^k \mathbf{A}^{-1} \quad . \end{aligned} \tag{5.28}$$

Hence, the LS estimate of x_2 with *k*-term approximation to matrix inversion is,

$$\begin{aligned}\tilde{x}_2 &= \tilde{\mathbf{A}}_k^{-1}\mathbf{B}_2^T y \\ &= (\mathbf{A}^{-1} - \Theta_k)\mathbf{B}_2^T y \\ &= (\mathbf{I} - \Theta_k \mathbf{A})\mathbf{A}^{-1}\mathbf{B}_2^T y \\ &= (\mathbf{I} - \Theta_k \mathbf{A})\,\hat{x}_2 \quad . \end{aligned} \tag{5.29}$$

Equation (5.29) shows that the approximation error on LS estimate depends on the residual error term $\Theta_k\mathbf{A}$. The following theorem upper bounds the probability that a k-term approximation error exceeds a given threshold α, where $\alpha > 0$.

Theorem 5.1 *Let* $\mathbf{B}_2 \in \mathbb{R}^{M\times L}$ *follow i.i.d. real standard normal distributed. Then, for an integer* $k > 0$ *and any* $\alpha > 0$*, we have*

$$\Pr\left(\left\|\Theta_k \mathbf{A}\right\|_F^2 > \alpha\right) \le \frac{\sqrt{3}L^2\left(M+2\right)}{M^2\alpha^{1/k}} \quad , \tag{5.30}$$

where $\|\cdot\|_F$ *denotes Frobenius norm.*

Proof. The expect value of squares of Frobenius norm of the residual error term $\Theta_k\mathbf{A}$ is

$$\begin{aligned}\mathbf{E}\left(\left\|\Theta_k \mathbf{A}\right\|_F^2\right) &= \mathbf{E}\left(\left\|(-\mathbf{D}^{-1}\mathbf{E})^k\right\|_F^2\right) = \mathbf{E}\left(\left\|(\mathbf{D}^{-1}\mathbf{E})^k\right\|_F^2\right) \\ &\le \mathbf{E}\left(\left\|\mathbf{D}^{-1}\mathbf{E}\right\|_F^{2k}\right) \quad . \end{aligned} \tag{5.31}$$

The last inequality in (5.31) is true according to the sub-multiplicative property of Frobenius norm. Recall **D** is a real diagonal matrix,

$$d_{ii} = \varphi_i^T \varphi_i \quad . \tag{5.32}$$

Similarly, **E** is a real matrix with each element is,

$$e_{ij} = \varphi_i^T \varphi_j, \quad i \ne j \quad . \tag{5.33}$$

Therefore, Eq. (5.31) can be rewritten as

$$\begin{aligned}\mathbf{E}\left(\left\|\Theta_k\mathbf{A}\right\|_F^2\right) &\le \mathbf{E}\left(\left\|\mathbf{D}^{-1}\mathbf{E}\right\|_F^{2k}\right)\\ &= \mathbf{E}\left(\sum_{i=1}^{L}\sum_{j=1}^{L}\left|\frac{e_{ij}}{d_{ij}}\right|^{2k}\right)\\ &= \sum_{i=1}^{L}\sum_{j=1}^{L}\mathbf{E}\left(\left|\frac{e_{ij}}{d_{ij}}\right|^{2k}\right)\\ &= \sum_{i=1}^{L}\sum_{j=1}^{L}\mathbf{E}\left(\left|\frac{\varphi_i^T\varphi_j}{\varphi_i^T\varphi_i}\right|^{2k}\right)\\ &\le \sum_{i=1}^{L}\sum_{j=1}^{L}\sqrt{\mathbf{E}\left(\frac{1}{\left|\varphi_i^T\varphi_i\right|^{4k}}\right)\mathbf{E}\left(\left|\varphi_i^T\varphi_j\right|^{4k}\right)}\quad . \end{aligned} \tag{5.34}$$

The last equation follows the Cauchy-Schwarz inequality. Since $\mathbf{B}_2$ is from real standard normal distribution, d_{ii} follows Chi-squared distribution with M degrees of freedom, i.e. $d_{ii} \sim \chi_k^2$. For 1-term approximation, i.e. k = 1, we have the following expectation according to the moment generating function,

$$\mathbf{E}\left(|\varphi_i^T\varphi_i|^4\right) = M\left(M+2\right)\left(M+4\right)\left(M+6\right)$$

$$\mathbf{E}\left(|\varphi_i^T\varphi_j|^4\right) = 3M\left(M+2\right)$$

Hence, for 1-term approximation, Eq. (5.34) can be rewritten as

$$\begin{aligned}\mathbf{E}\left(\left\|\Theta_2\mathbf{A}\right\|_F^2\right) &\le \sum_{i=1}^{L}\sum_{j=1}^{L}\sqrt{\mathbf{E}\left(\frac{1}{\left|\varphi_i^T\varphi_i\right|^4}\right)\mathbf{E}\left(\left|\varphi_i^T\varphi_j\right|^4\right)}\\ &= \left(L^2-L\right)\sqrt{\frac{3M\left(M+2\right)}{M\left(M+2\right)\left(M+4\right)\left(M+6\right)}}\end{aligned}$$

$$\leq \frac{\sqrt{3}L^2\left(M+2\right)}{M^2} \quad . \tag{5.35}$$

According to Markov's inequality, for any $\alpha > 0$, we have,

$$\begin{aligned}
\Pr\left(\left\|\Theta_k \mathbf{A}\right\|_F^2 > \alpha\right) &\leq \Pr\left(\left\|\mathbf{D}^{-1}\mathbf{E}\right\|_F^{2k} > \alpha\right) \\
&= \Pr\left(\left\|\mathbf{D}^{-1}\mathbf{E}\right\|_F^2 > \alpha^{1/k}\right) \\
&\leq \frac{\mathbf{E}\left(\left\|\mathbf{D}^{-1}\mathbf{E}\right\|_F^2\right)}{\alpha^{1/k}} \\
&\leq \frac{\sqrt{3}L^2\left(M+2\right)}{M^2\alpha^{1/k}} \quad .
\end{aligned}$$

□

Theorem 5.1 suggests that it's possible to constrain the probability of a large residual error caused by inversion approximation to arbitrarily small by increasing the sampling rate *M*. Recall that in the SPLS estimator, *L* is set smaller than *M*. The *k*-term approximation approach in matrix inversion has bounded error probability when *M* scales faster than L^2.

Now we calculate the hardware cost for the SPLS. The 2-term approximation method has *L* divisions, and 2*($L^2 - L$) multiplications without an addition. As a low-cost matrix inversion scheme, Cholesky decomposition is selected for comparison which has *L* divisions, 1/3**L**($L^2 - 1$) multiplications and 1/3**L**($L^2 - 1$) additions. It is clear 2-term approximation has much lower computational complexity (and thus lower hardware cost) compared with Cholesky decomposition.

V.E. Numerical Results

Define signal-to-noise ratio (SNR) as the ratio of signal power P_{signal} and noise power P_{noise}. Also, define the sub-Nyquist sampling ratio (SSR) as the ratio of the actual sampling rate f_s to the Nyquist rate $f_{Nyquist}$,

$$\text{SNR} = \frac{P_{\text{signal}}}{P_{\text{noise}}} \quad . \tag{5.36}$$

$$\text{SSR} = \frac{f_s}{f_{Nyquist}} \quad . \tag{5.37}$$

A ternary timing signal with a sparsity of 0.2% is captured by the DRS-I to examine the statistics of the SPLS estimator. According to the reliable sampling rate in CS framework formulated in Eq. (2.13), we sweep the SSR from 4% to 7% and observe the resulting signal reconstruction performance. Fig. 26 compares the analyzed bias and variance to the simulation at 0dB SNR, which can be typical in radar detection and ultrasound imaging systems. Simulation results illustrate an inverse relationship between the bias and variance of the estimator and the sampling rate, which matches the analysis in Section C. The difference is caused by the worst case assumption made in the theoretical analysis. Fig. 26 also indicates a small bias and variance even with heavy observation noise. It is because the SPLS scheme converts each section recovery to an over-determined LS problem, which is known to be noise robust. Although interference from nonzero elements outside of the projection window presents in the LS estimate, it is small compared with the unit amplitude, which supports ternary amplitude detection.

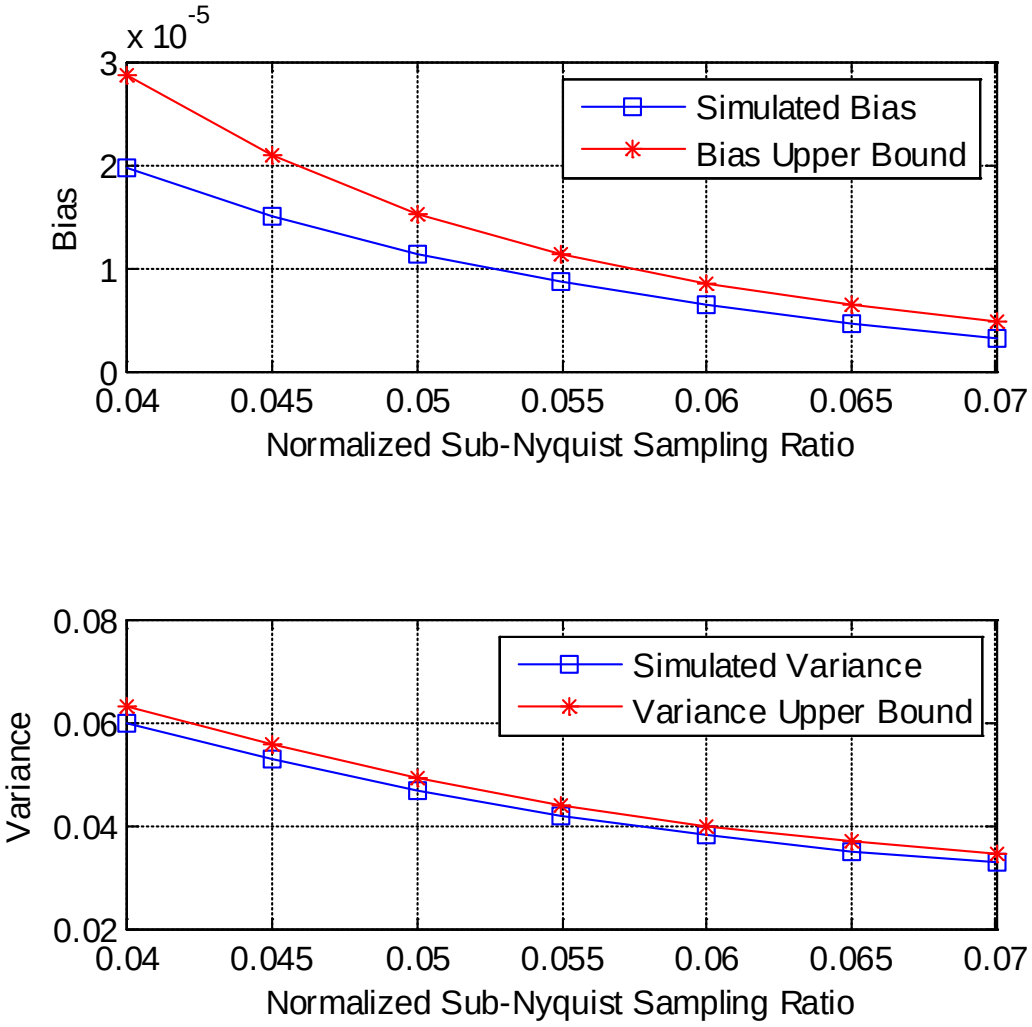

Fig. 26. Comparison of analysis and simulated bias and variance of the proposed SPLS scheme at 0dB SNR for a sparse ternary timing signal with a sparsity of 0.2%.

For low SNR applications, we simulate the signal recovery in an SNR of 5dB. A ternary sparse signal with a dimension of 10000, and a sparsity of 0.38% is simulated. M is set to 1300, i.e. an equivalent SSR of 13%. Fig. 27 shows the SPLS estimation result from compressed and noise-corrupted measurements. As a reference, the maximum bias on expectation and optimal ternary-valued amplitude detection threshold are also shown using black and red line, respectively. In Fig. 27, the maximum bias on expectation decreases along the signal dimension due to the interference prune step which reduces the interference from nonzeros outside of current projection window. The variance of each section estimate also decreases along the signal dimension. The optimal ternary amplitude detection is derived from Eq. (5.25). In Fig. 27, the SPLS scheme reconstructs the original ternary sparse signal after amplitude detection even with heavy noise. It is because the SPLS estimator utilizes a "tall" matrix $\mathbf{\Phi}_\Omega$ which leads to an over-determined problem in each section recovery, and thus is robust to the heavy noise.

Amplitude detection can be performed on each section estimate when the input comes from a finite set, i.e. $x \in \{-1, 0, 1\}$. The thresholds in (5.25) are selected for the SPLS estimator. For comparison, the threshold is set to ±0.5 for the conventional sparse recovery algorithms as these CS estimators are able to yield an exact (but noisy) signal recovery with high probability. In other words, they are unbiased with a high probability, allowing simple choice of threshold following reconstruction. It has been demonstrated in [90], both theoretically and numerically, that the basis pursuit de-noise (BPDN), the Dantzig selector, and the OMP all have MSE proportional to the oracle estimator MSE which coincides with the unbiased Cramer-Rao bound for exactly K-sparse deterministic

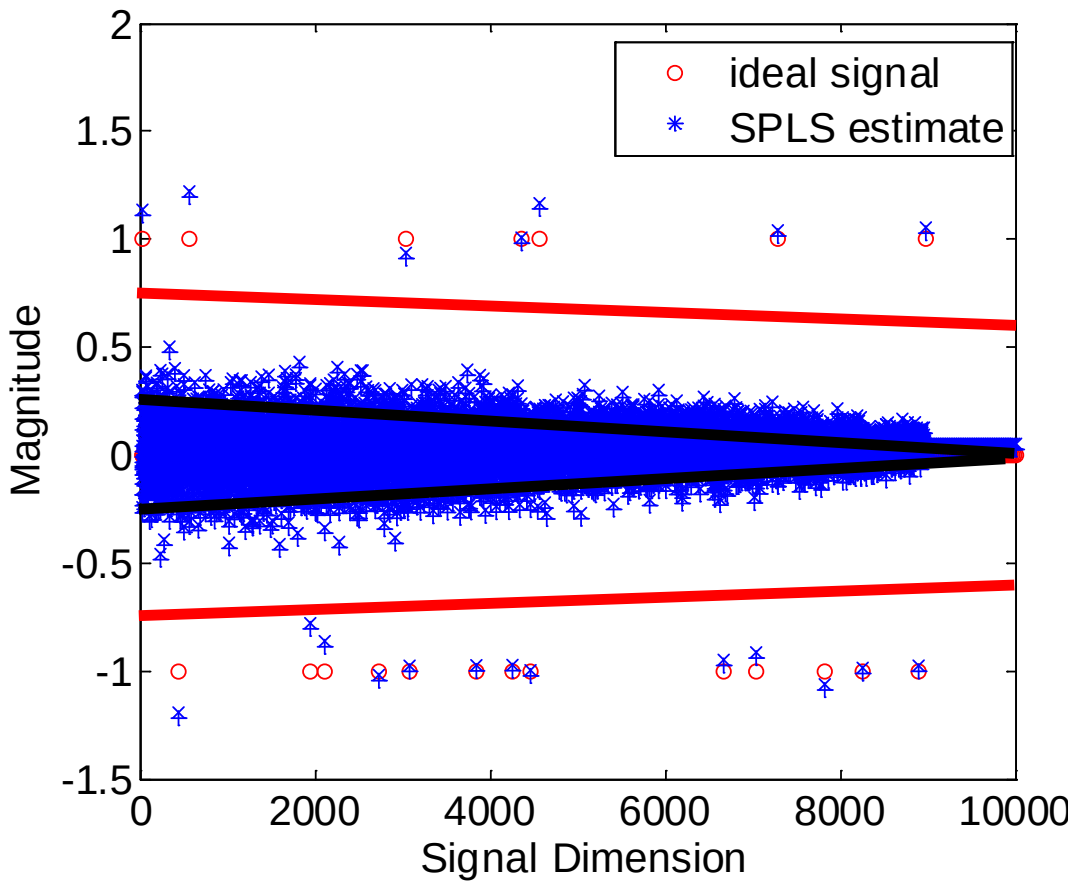

Fig. 27. SPLS estimation result at 5dB SNR with a sub-Nyquist sampling ratio of 13% for ternary input with sparsity of 0.38%.

signals. The oracle estimator performs an optimal least squares estimate by including the prior knowledge of the sparse signal support [91].

The ternary sparse signal comes from the proposed CT-TE scheme. To study the effectiveness of the SPLS signal reconstruction scheme in recovering different kinds of

ternary sparse signals from the compressed samples, we introduce a clustering parameter (CP) as the minimum number of nonzero elements in a cluster. By varying CP, different ternary signals are emulated, e.g., dense and scattered distribution signal models. We set the signal dimension to be 10,000, with a sparsity of 0.2%. The SSR is set to 0.08. Three window sizes L equal to 10, 20 and 40 are simulated. 100,000 iterations are carried out for Monte Carlo simulations.

Fig. 28 illustrates the error rate (ER) vs. CP parameterized by different window sizes in the split projection. The ER improves slightly when CP increases in both the noise free and 5dB SNR cases. The improvement is due to the fact that a larger CP has a more concentrated distribution of the nonzero elements. This helps reduce the possibility of a large number of nonzero elements falling outside of a selected split projection window, and therefore reduces the probability of large interference. Similar results are observed from different split projection window sizes, i.e., ER improves as L increases.

Nevertheless, the CP influence on ER is marginal in the SPLS scheme as shown in Fig. 28. The ER performance remains almost unchanged even for CP = 1, which has the most scattering distribution of nonzero elements. This indicates that the SPLS scheme is not constrained on the clustering signal model, and can be applied to the general ternary output of the CT-TE scheme, even though additional benefit does occur for cases with more concentrated nonzero elements.

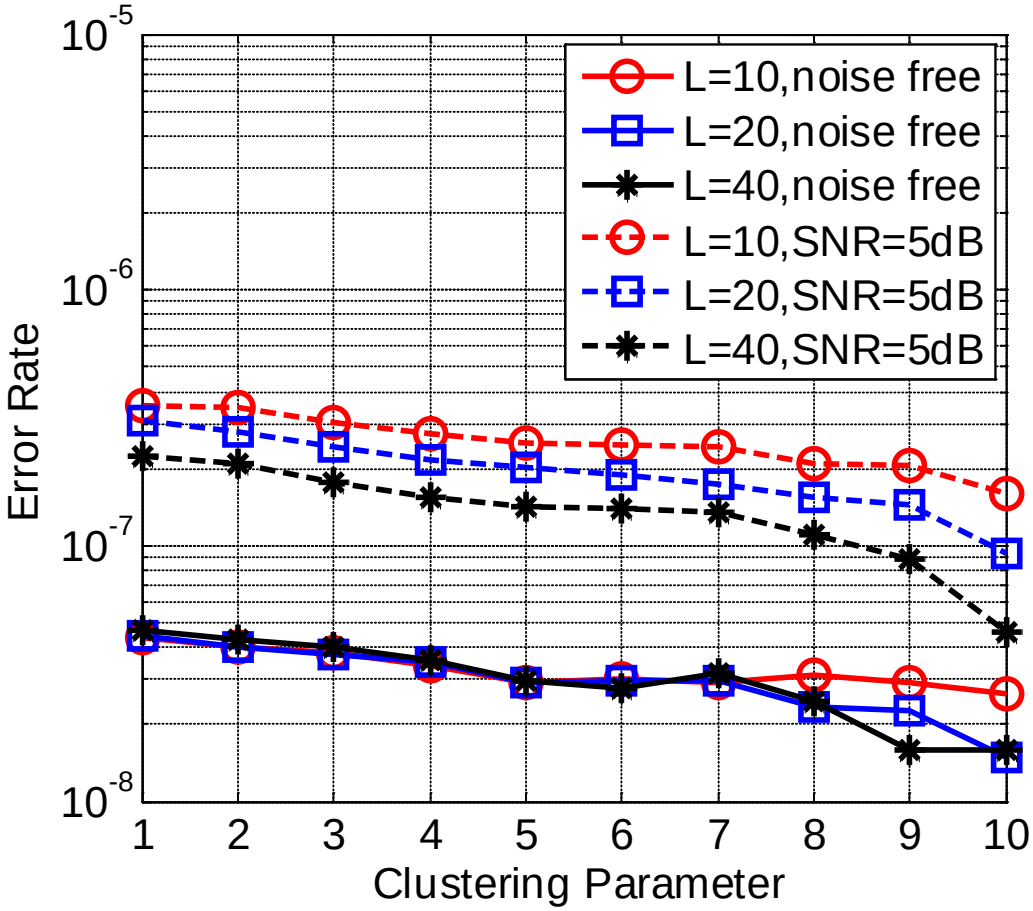

Fig. 28. Error rate (ER) performance parameterized by different clustering parameters (CP) and window sizes in the Split-Projection Least Squares (SPLS) scheme.

The split projection window size has a relatively larger impact on ER compared with CP, especially for the noisy case. This is because both noise and interference affect the ER performance. Consider each column of the measurement matrix as a signal representation atom. A larger L has some benefits. For example, it provides a larger dictionary to interpret the compressed measurements in each split projection recovery, which reduces the possibility of fitting noise and interference. When both the noise and interference are strong, fitting them degrades the ER performance, and also reduces the interference caused by the nonzero elements outside of the split projection window.

Note that the computational complexity of the SPLS scheme is $O(MNL)$. A larger L naturally increases the computational cost.

Fig. 29 shows the ER performance after amplitude detection. For conventional signal recovery algorithms, the threshold is set to ±0.5 due to ternary amplitude. While for the SPLS estimator, the threshold is determined by (5.25). Fig. 29 demonstrates the SPLS scheme has the best ER after amplitude detection among all the other CS signal recovery schemes in low SNR region because each section recovery is a local over-determined problem which is robust to heavy observation noise.

We next examine the finite word-length effect (also known as fixed-point effect) to the SPLS scheme. Finite word-length effect stems from the quantization process of coefficients and internal results in a DSP system. Quantization is a necessary step when implementing a floating-point algorithm into a fixed-point hardware, for example, field-programmable gate array (FPGA), application-specific integrated circuit (ASIC), etc. Fixed-point quantization degrades system performance and needs careful investigation.

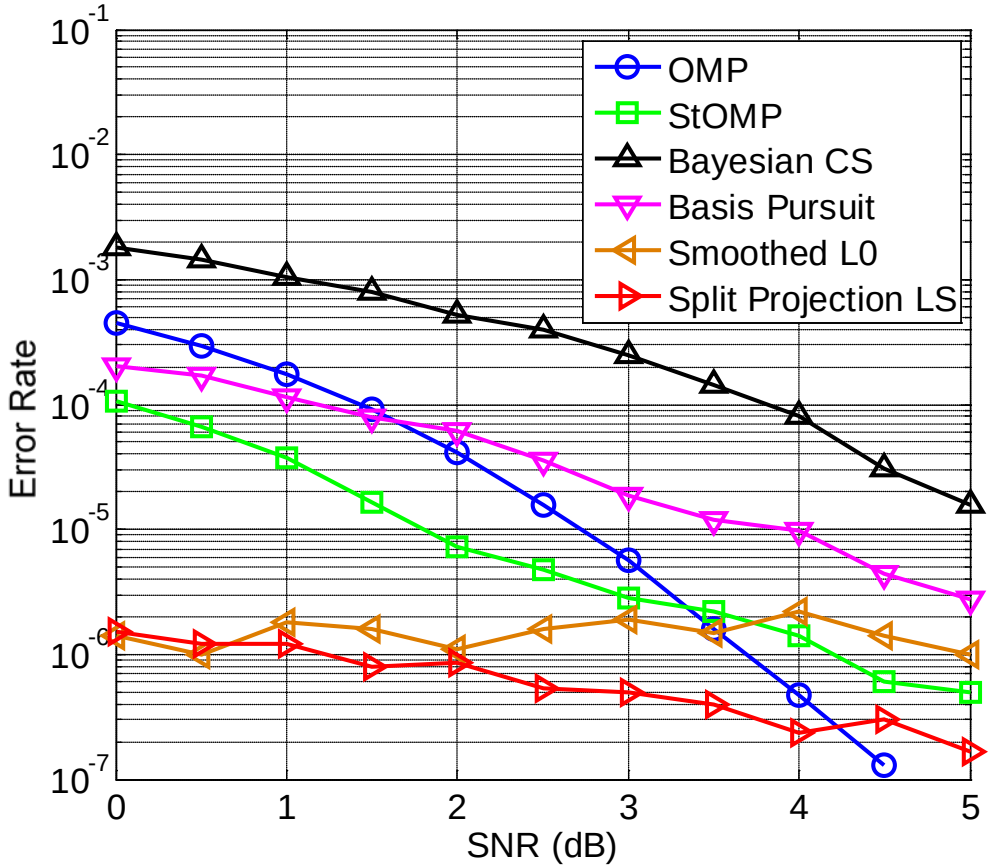

Fig. 29. ER of recovered ternary signal after amplitude detection at a SSR of 6%. 10000 independent simulations of a ternary sparse signal with dimension of 10000. Popular CS signal reconstruction algorithms are compared.

The proposed SPLS scheme employs standard LS estimator for each independent section recovery. As discussed in Section B, the SPLS is an MVU estimator when the projection window includes all nonzero elements. We study the *k*-term approximation to matrix inversion in a stand-alone LS problem.

Let's choose $\mathbf{B}_2$ from standard normal distribution with a dimension of 10000 by 100. And follow LS approach to solve the linear problem, $y = \mathbf{B}_2 x + w$, where x is a random ternary signal, w is Gaussian noise, with distribution $w \sim \mathcal{N}(0,\ \sigma^2)$.

Fig. 30 shows the Mean Squared Error (MSE) of LS estimate parameterized by the number of quantization bits Q at a 10dB SNR, which is defined in (5.36). Cholesky decomposition and floating point result are included for comparison. In Fig. 30, we can see that fixed-point Cholesky decomposition achieves floating point performance when Q is larger than 13 at a 10dB SNR. While error floors appear in the *k*-term approximation method when Q is larger than 10. It is because a finite term approximation in (5.27) introduces residual error. And a higher k results in less residual error and less MSE. However, Fig. 30 indicates that the MSE improvement by using more approximation terms becomes marginal when k is larger than 2.

Fig. 31 shows the MSE of LS estimate versus SNR when using 10-bit word length in fixed-point representation. At relatively high SNR (SNR $\geq$ 10dB), 10-bit quantization is insufficient to keep the MSE performance as both approximation scheme and Cholesky decomposition have error floors on the MSE of LS estimate. However, at low SNR region (SNR $\leq$ 10dB), 2-term approximation has a similar MSE performance in comparison to Cholesky decomposition.

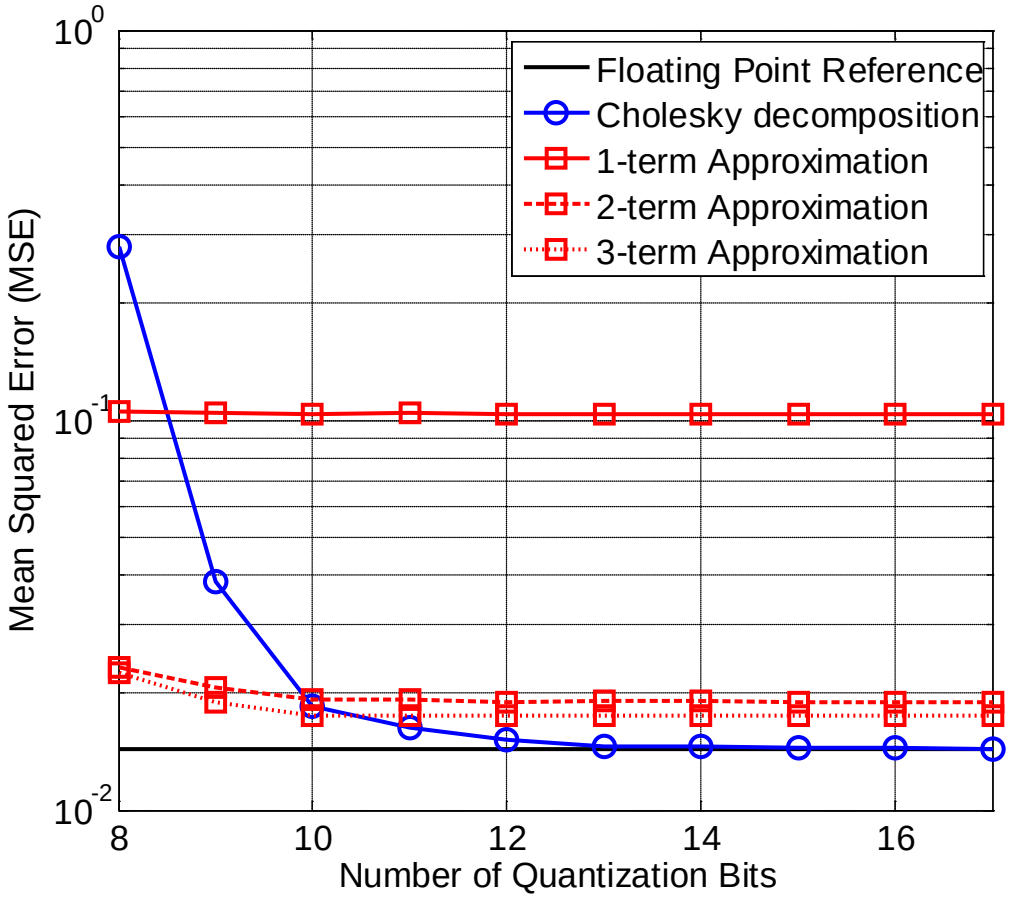

Fig. 30. Mean squared error (MSE) of least squares estimate parameterized by the number of quantization bits Q at 10dB signal-to-noise ratio (SNR).

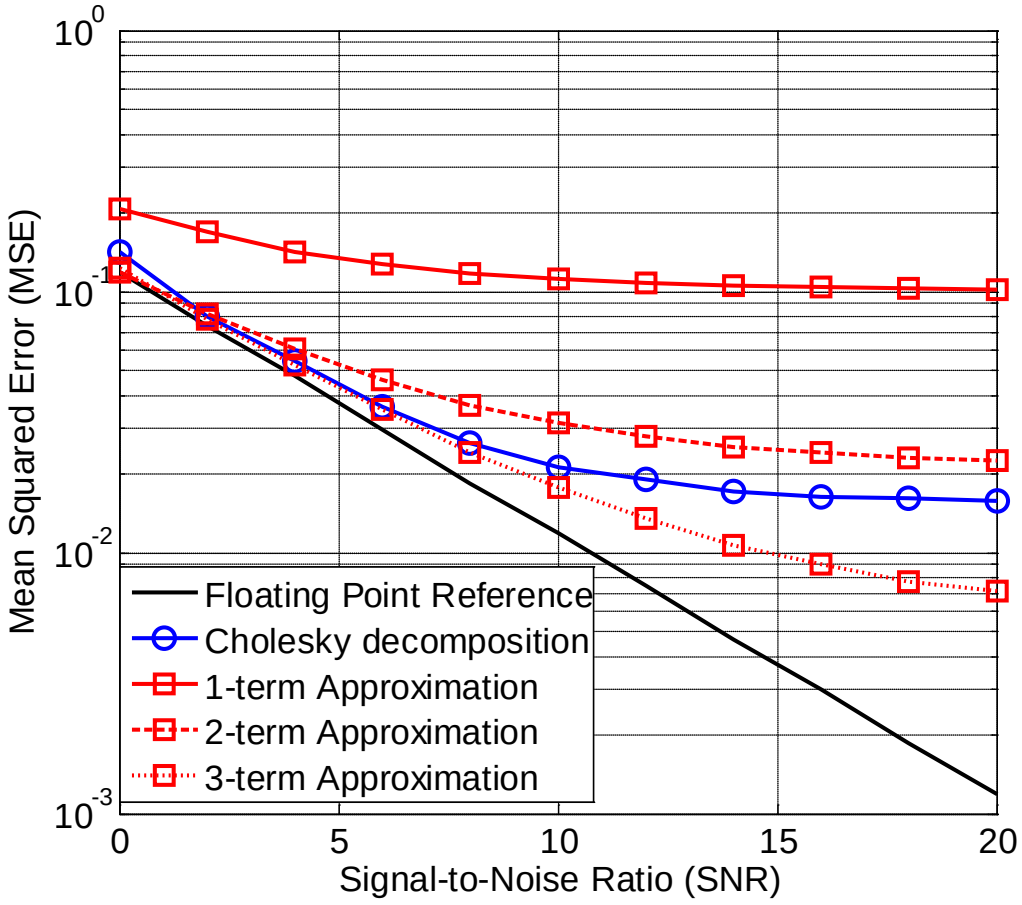

Fig. 31. MSE of LS estimate versus SNR when using 10-bit word length in fixed-point representation.

Combining Fig. 30 and Fig. 31, a 2-term approximation can be a good alternative to Cholesky decomposition at low SNR region considering it has quadratic (rather than cubic) multiplication growth to the problem size and no addition. In the rest simulations we adopt 10-bit 2-term approximation to matrix inversion.

Fig. 32 illustrates the error rate versus CP parameterized by different windowing sizes in the split projection when 2-term approximation to matrix inversion is applied. The error rate improves slightly when CP increases in both the noise free and 5dB SNR cases. The improvement is due to the fact that a larger CP has a more concentrated distribution of nonzero elements. This helps reduce the possibility of a large number of nonzero elements falling outside of a selected split projection window, and reduces the probability of large interference in LS estimate. Similar results are also observed from different window sizes, i.e., the error rate performance improves as L increases. For comparison, orthogonal matching pursuit (OMP) in [42] is also included. OMP has identical error rate among different CPs.

V.F. Summary

In this chapter, we proposed a low-complexity signal reconstruction algorithm called split-projection least squares (SPLS). The SPLS exploits the ternary amplitude *prior* and the nonlinear splits CS signal reconstruction into a series of independent LS problems. We derived the statistics of the SPLS estimator and analyzed computational complexity. In hardware implementation, we presented a k-term approximation method to matrix inversion that exhibits lower cost but comparable performance when compared with conventional Cholesky decomposition.

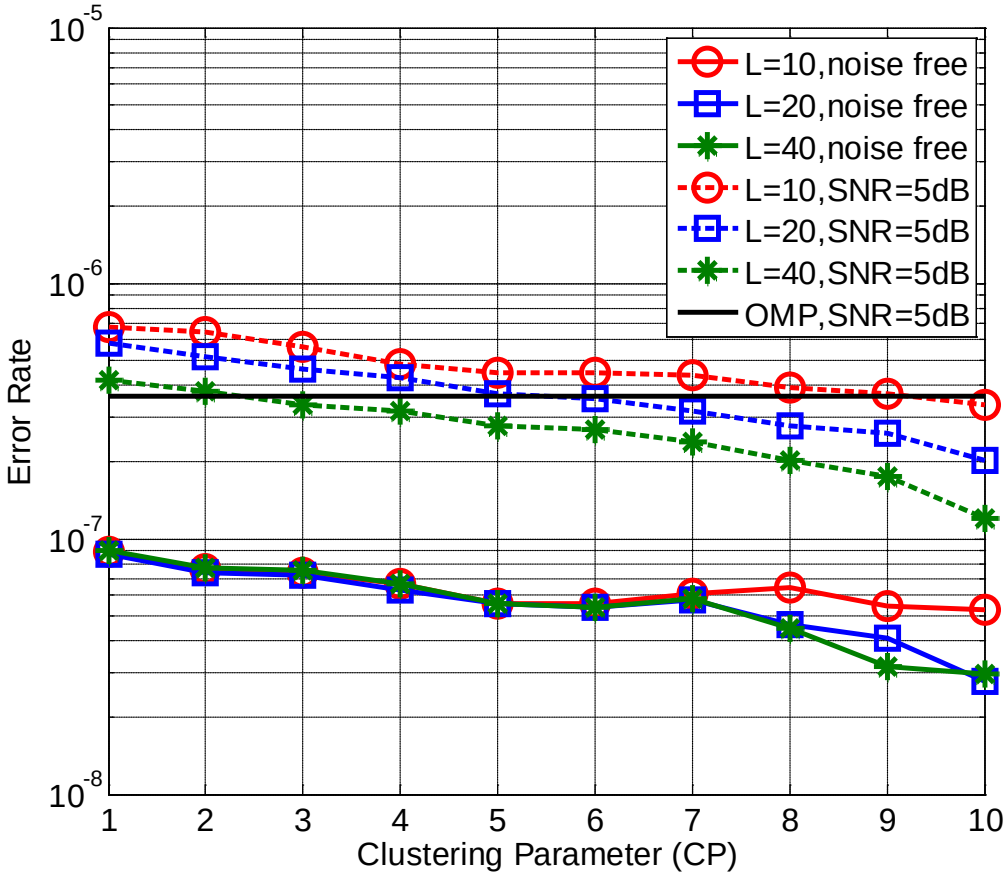

Fig. 32. Error rate performance parameterized by different clustering parameters and windowing sizes in split-projection least squares when 2-term approximation to matrix inversion is applied.

CHAPTER VI

APPLICATION EXPERIMENTS*

In this chapter, we study the performance of the proposed ACS front-end and SPLS signal reconstruction algorithm in two low-power and noise-sensitive applications. The first one is interference-robust radar system with in-band wireless communication interference. We propose a multi-channel filter banks ACS scheme for the interference-robust radar front-end. The related work is published in [95], [101], [105]. The second application is portable diagnostic ultrasound imaging system. We propose a compressed ultrasound beamformer to support a large transducer array in a low-power diagnostic ultrasound system. The related work is published in [106].

VI.A. Interference-Robust Radar with In-Band Interference

VI.A.1. Radar Background

We first review the background of conventional monostatic pulsed radar system. Monostatic radar indicates that the same antenna is used to transmit and receive. Pulsed radar means the transmitting signal is discrete pulse rather than continuous waveform. The block diagram of a monostatic pulsed radar system is shown in Fig. 33 [93]. T/R

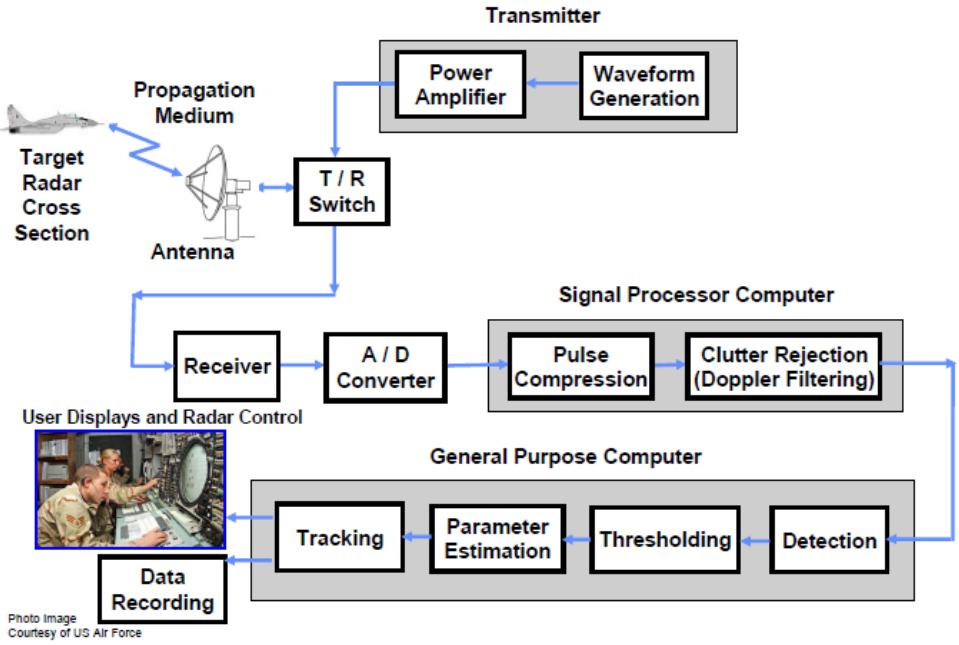

Fig. 33. Block diagram of a monostatic pulsed radar system. Taken from [93].

switch alternately switches the antenna between the transmitter and receiver so that only one antenna needs to be used. In the receive signal chain, receiver module contains low-noise preamplifier, mixer, IF amplifier.

Target ranging is formulated by a time-delay problem in radar systems. Suppose a monostatic pulsed radar transmits a pulse at time t_0. The echo pulse is received at time t_1 with a time delay of $T_R = t_1 - t_0$. For a monostatic pulsed radar system, the distance between radar and target can be estimated by

$$R = c * T_R / 2 \quad , \tag{6.1}$$

where c is the velocity of light in free space. Fig. 34 illustrates the signal waveform in the time delay ranging process of a pulsed radar system [92].

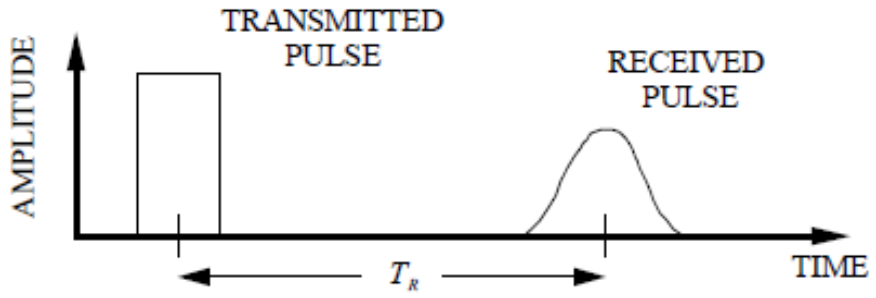

Fig. 34. Illustration of the signal waveform in the time delay ranging process of a pulsed radar system. Taken from [92].

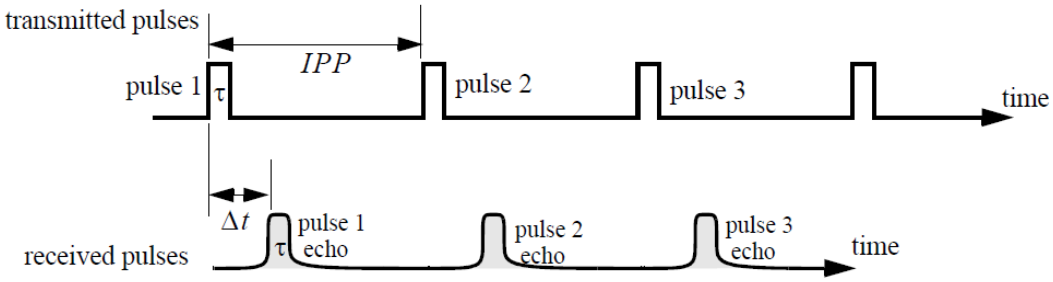

Fig. 35. Transmitted and received pulses in a pulsed radar system. Taken from [92].

Generally, a pulsed radar transmits and receives a train of pulses, as illustrated by Fig. 35. Inter-pulse period (IPP) is T, and pulse width is τ. The distance corresponding to the two-way time delay is known as the radar unambiguous range $R_u = c*T/2$.

Range resolution ΔR is a radar metric that describes its ability to detect targets in close proximity to each other as distinct objects. Radar systems are normally designed to operate between a minimum range R_{min}, and maximum range R_{max}. The distance between R_{min} and R_{max} is divided into I range bins or gates, each of width ΔR.

$$\Delta R = \frac{R_{\max} - R_{\min}}{I} \quad . \tag{6.2}$$

Targets separated by at least ΔR will be completed resolved in range. Targets within the same range bin can be resolved in cross range (azimuth) utilizing signal processing techniques. In a two-way system, ΔR should be greater or equal to $c*\tau/2$. Since the radar bandwidth B is equal to $1/\tau$, we have

$$\Delta R = \frac{c\tau}{2} = \frac{c}{2B} \quad , \tag{6.3}$$

As suggested by Eq. (6.3), in order to achieve fine range resolution one must minimize the pulse width τ. However, this will reduce the average transmitted power and increase the operating bandwidth. Achieving fine range resolution while maintaining adequate average transmitted power can be accomplished by using pulse modulation techniques. One example is linear-frequency modulated (LFM) pulse, whose bandwidth is determined by the highest chirp frequency rather than pulse width. Fig. 36 shows a LFM pulse example with 6.67μs pulse width and 3MHz bandwidth.

Since the transmitted pulses are known at the receiver side, target detection in a monostatic pulsed radar can be considered as the deterministic signal detection with unknown arrival time n_0, or equivalently the pulse delay. A generalized likelihood ratio test (GLRT) might be employed as a detector. We now consider the detection problem,

$$\begin{aligned} H_0 &: x[n] = w[n] \\ H_1 &: x[n] = s[n - n_0] + w[n] \end{aligned} \quad , \tag{6.4}$$

where $n = 0, 1, \ldots, N - 1$ is the observation interval, $s[n]$ is a known deterministic signal that is nonzero over the interval $[0, M - 1]$, n_0 is the unknown delay, and $w[n]$ is white

Gaussian noise (WGN) with variance σ^2. Suppose the observation interval should include the signal for all possible delays. A GLRT would decide H_1 if

$$L(x) = \frac{p(x;\hat{n}_0, H_1)}{p(x;H_0)} > \gamma \quad , \tag{6.5}$$

where $\hat{n}_0$ is maximum likelihood estimator (MLE) by solving (6.6) over all possible n_0,

$$\hat{n}_0 = \arg\max_{n_0} \sum_{n=n_0}^{n_0+M-1} x[n]s[n-n_0] \quad . \tag{6.6}$$

The threshold γ is found from a specified probability of false alarm P_{FA},

$$P_{FA} = \int_{\{x:L(x)>\gamma\}} p(x;H_0)dx = \alpha \quad . \tag{6.7}$$

Hence, we decide H_1 if

$$L_G(x) = \frac{\frac{1}{(2\pi\sigma^2)^{\frac{N}{2}}} \exp\left[-\frac{1}{2\sigma^2}\sum_{n=0}^{N-1}\left(x[n]-s[n-\hat{n}_0]\right)^2\right]}{\frac{1}{(2\pi\sigma^2)^{\frac{N}{2}}} \exp\left[-\frac{1}{2\sigma^2}\sum_{n=0}^{N-1}x^2[n]\right]} > \gamma$$

$$\Leftrightarrow L_G(x) = \prod_{n=\hat{n}_0}^{\hat{n}_0+M-1} \exp\left[-\frac{1}{2\sigma^2}\left(-2x[n]s[n-\hat{n}_0] + s^2[n-\hat{n}_0]\right)\right] > \gamma \quad . \tag{6.8}$$

Taking logarithms we have test statistic $T(x)$ and we decide H_1 if

$$T(x) = \max_{n_0 \in [0, N-M]} \sum_{n=n_0}^{n_0+M-1} x[n]s[n-n_0] > \gamma' \quad . \tag{6.9}$$

If H_1 is claimed, the n_0 yielding maximum $T(x)$ is the time-delay estimation; otherwise H_0 is claimed, and no target is found. Note that $T(x)$ in (6.9) is uniformly most

powerful (UMP). It is a derivation of estimator-correlator, and therefore it is suboptimal in Neyman-Pearson (NP) sense as it *incoherently* combines the data.

The case of unknown arrival time n_0 and unknown amplitude A can also be derived. It is usually the case when target's radar cross section (RCS) is fluctuating. The test statistic in this case is shown in Eq. (6.10). We decide H_1 if $T(x) > \gamma'$.

$$T(x) = \max_{n_0 \in [0, N-M]} \left| \sum_{n=n_0}^{n_0+M-1} x[n] s[n-n_0] \right| \quad . \tag{6.10}$$

Note that (6.10) is not UMP as $T(x)$ depends on A. Also, it is suboptimal in the NP sense.

VI.A.2. Multi-Channel Filter Banks ACS Front-End

We now study the performance of the ACS front-end in radar system. Equation (6.3) suggests that the radar range resolution is proportional to the transmitted signal bandwidth. However, a high bandwidth pulse requires a very high sampling rate that introduces significant design challenges, such as high power consumption in the high-speed ADC, large volumes of data to be stored, transmitted and processed in a real-time. Noise is another fundamental limitation to the accurate radar measurements. There are two types of noise inevitable in any radar systems, thermal noise and quantization error.

Let z denote the received baseband radar signal, which consists of a pulsed reflection signal s, thermal noise n, and quantization error q. Thus we have,

$$z = s + n + q \quad . \tag{6.11}$$

In order to quantify the accuracy of the time-delay estimation, we investigate the root mean square (rms) of the difference between the estimated value and the true one. It has been shown in [94] that rms error in a time-delay measurement can be expressed as,

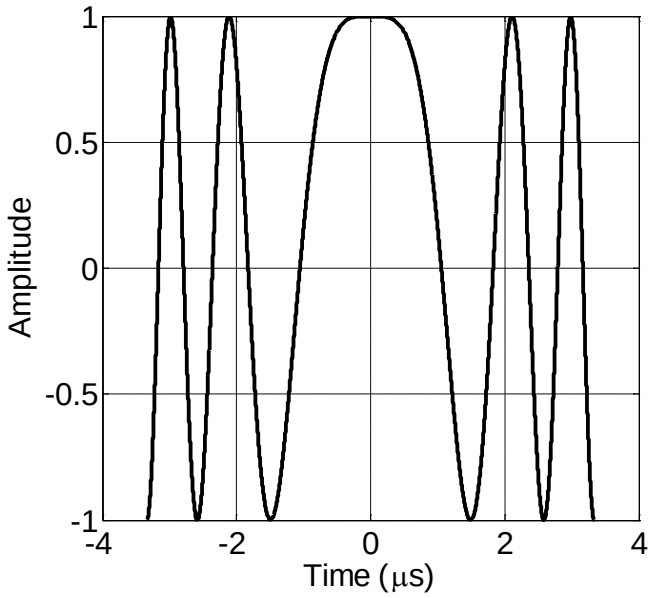

(a)

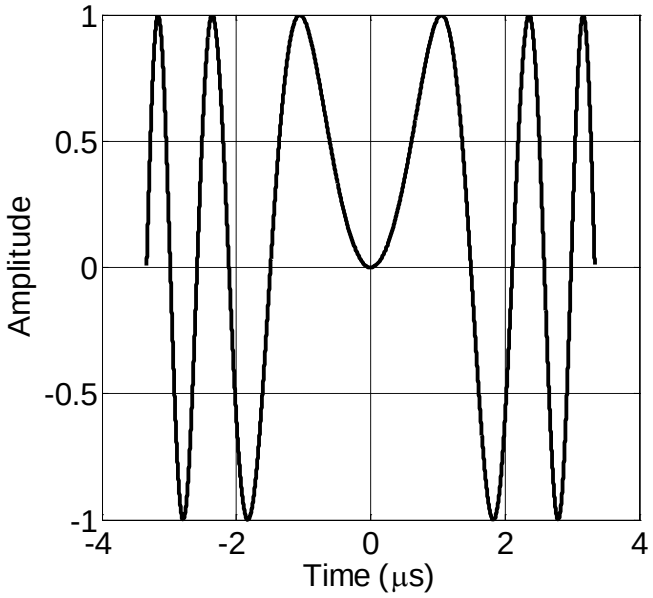

(b)

Fig. 36. Linear-frequency modulated (LFM) pulse with 6.67μs pulse width and 3MHz bandwidth (a) real part; (b) imaginary part.

$$T_{\text{rms}} = \frac{1}{\beta\left(2E / N_0\right)^{1/2}} \quad . \tag{6.12}$$

where E and N_0 is signal and noise power, β is the effective bandwidth defined as,

$$\beta^2 = \frac{\int_{-\infty}^{\infty} (2\pi f)^2 \left|S(f)\right|^2 df}{\int_{-\infty}^{\infty} \left|S(f)\right|^2 df} \quad . \tag{6.13}$$

and $S(f)$ is the spectrum of pulse signal. In an ideal ADC, quantization error is uniformly distributed between $-\Delta/2$ and $+\Delta/2$. In this case, the quantization error is modeled as the white noise with a power spectrum density (PSD) of

$$\text{PSD}(q) = \frac{\Delta^2}{12 f_s} \quad . \tag{6.14}$$

Note that thermal noise n and quantization error q are independent. We have rms of time-delay measurement in Eq. (6.15) where Q_0 is quantization noise power.

$$T_{\text{rms}} = \sqrt{\frac{N_0 + Q_0}{2\int_{-\infty}^{\infty} (2\pi f)^2 \left|S(f)\right|^2 df}} \quad . \tag{6.15}$$

Based on Eq. (6.15), an accurate time delay measurement implies increasing the frequency of transmitted pulses and/or decreasing the thermal and quantization noise. Equation (6.14) shows one can decrease the quantization noise by either increasing the sampling rate f_s or decreasing the quantization step Δ. Specifically, increasing the ADC resolution by 1 bit can decrease the quantization noise power by 6 dB. Also, doubling the oversampling rate decreases the quantization noise power by 3dB.

Comparing to the conventional ADCs, the ACS provides an alternative way to sample the radar signals. In the random sampling stage, the proposed CT-TE scheme

modulates pulse variations into high-speed ternary timing signals. Since CT-TE scheme gives the sampling efforts to the signal with most significant variations, it is efficient for the pulsed radar signals that are sparse in time domain. The oversampling architecture helps mitigate the quantization error generated by the low (ternary) resolution ADC. In addition, the asynchronous comparators allow the analog-to-digital conversion to be free from the clock jitter which is a fundamental limitation for high-speed ADCs. The large data resulted from the oversampling is reduced by a simplified digital CS technique. This results in excellent linearity and an overall sub-Nyquist sampling in the ACS front-end. The power consumption of the random sampler is also optimized by digital-assisted circuits and small duty cycle of power-demanding modules. In the reconstruction stage, the SPLS scheme recovers the ternary timing signals. After that, a linear detector or square law detector is selected depending on different target models. Fig. 37 shows the block diagram of radar system using ACS with an emphasis on the receive signal chain.

Fig. 38 shows the quantitative effect of thermal noise and quantization error on T_{rms}. A LFM pulse with 3MHz bandwidth and 6.7μs pulse width (Fig. 36) is simulated. Fig. 38 (a) and (b) show two cases when thermal noise and quantization noise are dominant, respectively. A Nyquist ADC and the CT-TE scheme with an oversampling ratio (OSR) of 1000 are simulated. For fair comparison, T_{rms} of the Nyquist ADC with OSR adjustment is also provided. In Fig. 38 (a), T_{rms} decreases by 1dB when the SNR increases by 2dB in both schemes. Fig. 38 (b) shows that increasing one quantization bit will reduce T_{rms} by 3dB. These results are expected given (6.15). This work is originally published in [95].

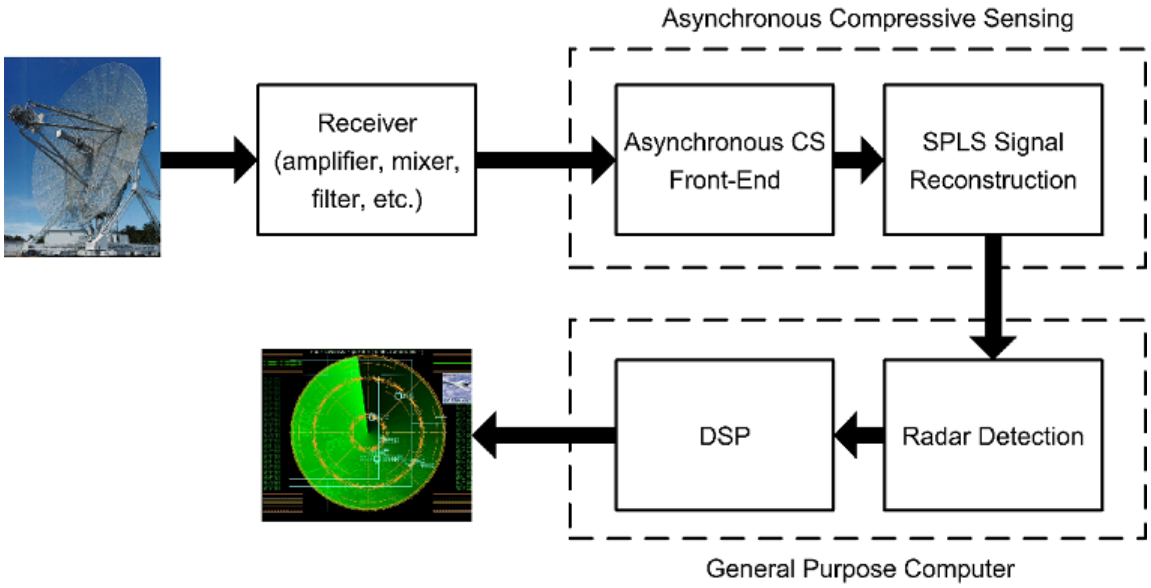

Fig. 37. Block diagram of radar receive signal chain using the proposed ACS front-end.

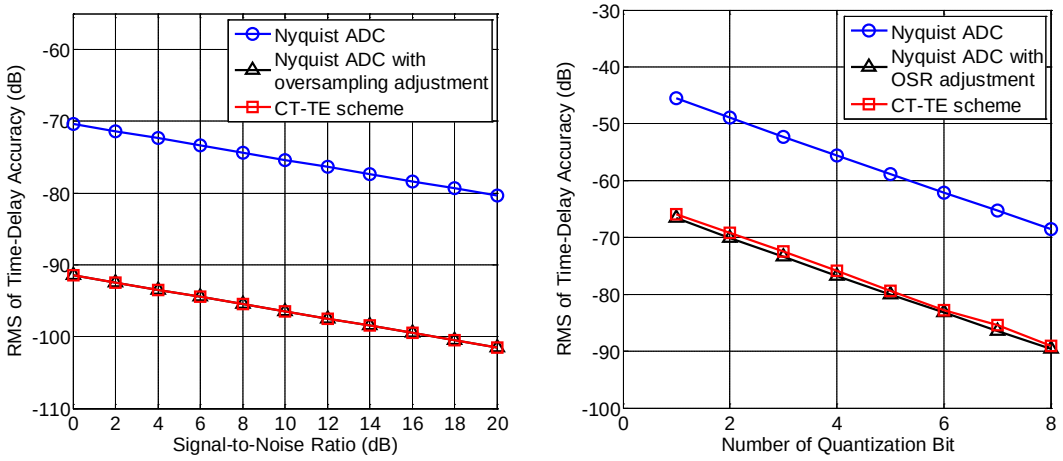

(a) (b)

Fig. 38. Quantitative effect of thermal noise and quantization noise on the rms error of time-delay estimation, GLRT detector is employed in both cases: (a) thermal noise is dominant; (b) quantization error is dominant.

The growing use of radar and communications motivates the development of a system that allows co-existence of both radar and wireless communications in the same spectrum allocation. Secure, resilient, and innovative spectrum-sharing technologies are necessary to enable new capabilities in wireless broad-band communications for general public and enhance spectrum availability for essential government services. Efficient coexistence of wireless data communications with the radar systems is imperative for public safety, homeland security, and national defense purposes [96].

A proper receiver architecture shall allow the coexistence of broadband wireless data communications with high-performance radar, enabling simultaneous vehicle-to-vehicle/internet broadband communications and collision avoidance (shown in Fig. 39), target/threat acquisition for military environments, and ultimately the potential for wide-spread autonomous vehicle transportation.

Proposed receiver solutions include parallel architectures such as filter banks to notch out the undesired interference [97], and advanced signal processing algorithms like spatial signal processing via MIMO [98]. Both solutions face challenges related to the power and complexity of the front-end implementation due to the multiple parallel signal processing channels. Given that a high-resolution radar system requires broadband transmit signals, and that the Shannon sampling theorem orders a sampling rate of at least twice the signal's bandwidth to avoid image aliasing, an excessive data volume appears at the outputs of conventional Nyquist-rate ADCs, which not only imposes challenges in the integration of a very large number of high-speed, high-resolution, and low-power ADCs, but also in the high-speed data links for digital processing.

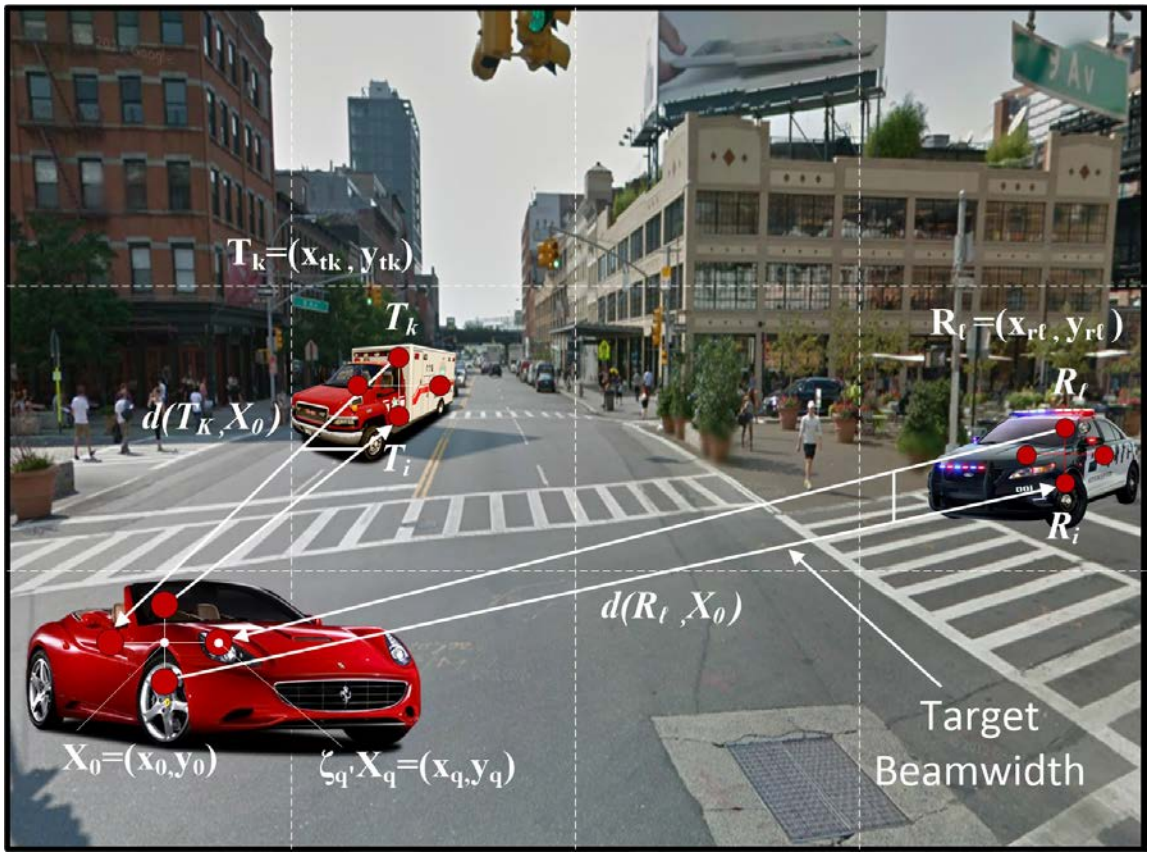

Fig. 39. Radar system with arbitrarily-spaced antennas in a vehicle-to-vehicle communications and collision avoidance application.

Some compressive sensing (CS) based data compression schemes are reported for radar systems [99], [100]. A random demodulator front-end is implemented in [99], which consists of a dedicated mixer and an integrator. In this architecture the mixer must operate at or above the Nyquist rate for sufficient randomization, resulting in significant dynamic power. Also, the integrator also produces considerable static power during the

charge accumulation stage. Since both of the mixer and integrator are active throughout measurement generation, the random demodulator approach consumes an excessive amount of power. In addition, the dedicated analog circuitry has to display high linearity, as non-linear distortion affects the reconstruction performance in the sparse recovery stage [33]. An alternative underspread linear system [100] also achieve sub-Nyquist sampling in radar system at expense of an active channel count of no fewer than four times the band number, resulting in increased overhead. Besides, challenges are faced in the *T*-periodic waveforms generation hardware.

In this section, a low-power filter-bank multi-channel ACS front-end is presented for an interference-robust radar with reduced data volume at the mixed-signal interface. Asynchronous operation exploits sparsity of the received signal when using pulsed radar signals. The integration of CS technique achieves sub-Nyquist sampling at the front-end. For signal recovery, the SPLS algorithm is adopted that exhibits very low complexity and good noise robustness compared with state-of-the-art CS estimators. Because low latency data processing is very important in all collision avoidance technologies, the above advantages let the SPLS algorithm become a strong candidate in a vehicle-to-vehicle collision avoidance radar system with in-band wireless interference. Numerical results demonstrate the proposed radar receiver is robust to the in-band interference and achieves 8-fold data compression compared with conventional Nyquist-rate ADCs. Although this paper studies the filter-bank based approach for interference-robust single antenna radar, the proposed ACS as a generic sub-Nyquist ADC is also applicable to MIMO radars that have an inherent multi-channel architecture.

Table 5. Specifications for vehicle-to-vehicle collision avoidance radar systems.

Parameter	**Value**
MAX Unambiguous Range	90 meter
Range Resolution	0.02 meter
Transmit Pulse	LFM: 8GHz bandwidth 1.25ns pulse width
Peak Transmit Power	70mW
Carrier Frequency	6GHz
Target Type	Swerling-2 type
In-band Interference Power	-50dBm ~ -70dBm

VI.A.3. Numerical Results

In order to convey the architecture and signal processing ideas, and to facilitate comparison with alternative approaches, we consider some specific representative radar and communications parameters. The related work is original published in [101],

A maximum unambiguous range of 90 meters is chosen for the braking/stopping distance at a speed of 100km/hour, which is around 80 meters [102]. Meanwhile, a range resolution of 0.02m is desired in city parking, demanding an 8GHz bandwidth LFM pulse. With a detection probability (Pd) of 0.9 and a false alarm probability (Pfa) of 10^{-6}, the parameters of the proposed collision avoidance vehicle-to-vehicle radar system are listed in Table 5. A 6GHz carrier frequency expands the radar pulse in a 2GHz~10GHz

spectrum where wireless communication signals (such as WLAN and cellular) are also present as interference with an assumed power level from -50dBm to -70dBm.

Analog filter banks are employed to notch out wireless interference while providing multiple channels for parallel processing. The filter bank consists of 20 2^{nd}-order filters that divide signal bandwidth into 20 equally spaced sub-bands of 400MHz each. Fig. 40 illustrates the filter bank spectrum response and output waveforms of each channel when radar signals and wireless interference are present simultaneously. For illustration, Fig. 40 shows the interference is falling in the 19^{th} channel with a power much stronger than the radar signals. The output of the 19^{th} channel and its neighbors are contaminated, whereas channels far away from the interference, e.g., the 1^{st}~17^{th} channels, are not strongly affected by the interference. The analog filter bank is also robust to clock jitter which is a fundamental limitation in high bandwidth systems [103].

We develop the ACS scheme as a sub-Nyquist sampling module [64] for pulsed-type broadband radar signals, which includes the CT-TE scheme and DRS-I. Fig. 41 shows the front-end architecture with emphasis on the mixed-signal interface. Fig. 9 shows the CT-TE scheme, where $z(t)$ and $y[n]$ are the input and output, respectively, and $p_c[n]$ is a pseudorandom sequence for CS. The CT-TE scheme is employed to convert the signal variations into high-speed ternary timing signals [64]. Asynchronous operation exploits the sparsity of radar echoes in a sparsely scattering environment. Power efficiency is improved by decreasing the circuit's duty cycle with on-demand activation. In addition, the adder and accumulator in DRS-I (Fig. 10) are asynchronous logic that exhibit reduced duty cycle in capturing the impulsive signals as shown in Fig. 40.

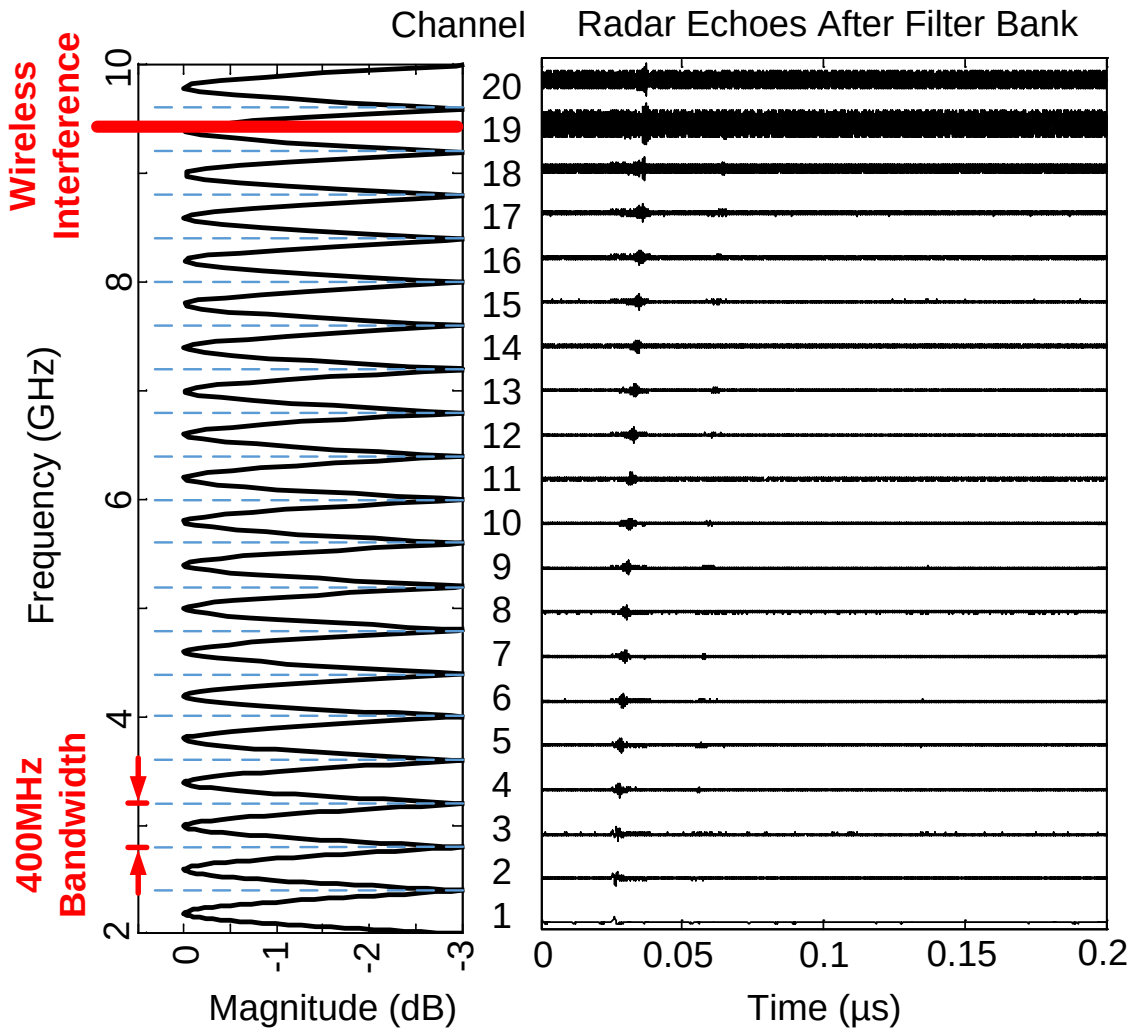

Fig. 40. Response of a 20-channel analog filter bank when pulsed radar signals and interference from wireless communication systems are present simultaneously. Wireless interference is in the 19th channel.

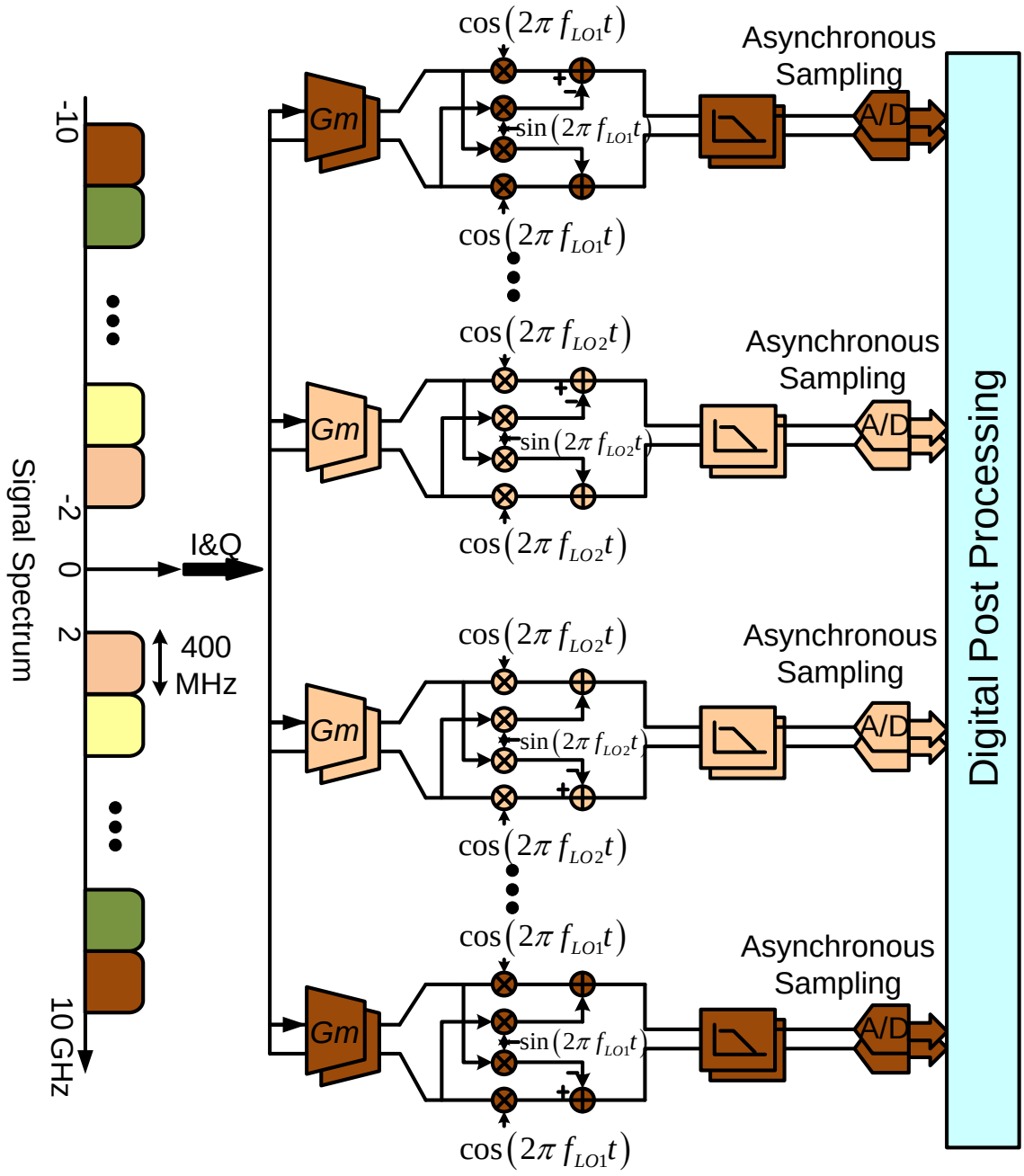

Fig. 41. Front-end architecture of the proposed interference-robust radar with emphasis on the mixed-signal interface.

An interference-robust radar with parameters in Table 5 is simulated. To evaluate the interference robustness, we define the signal-to-interference ratio (SIR) as the power ratio of interference to signal.

Fig. 42 compares error rate (ER) of ternary timing signal recovery via different CS reconstruction algorithms (basis pursuit [24], orthogonal matching pursuit (OMP) [42], stage-wise OMP (StOMP) [44], Bayesian compressive sensing (Bayesian CS) [54] and smoothed-L0 [55]) in a heavy noise radar scenario (0dB~5dB SNR). The ternary timing signal from the CT-TE scheme has an average sparsity of 0.38%, with an SSR of 0.13 in the simulations, or approximate 8-fold data volume compression. In Fig. 42, the SPLS estimator has the best ER performance over the entire SNR range. This important performance advantage comes from the use of a "tall" matrix $\mathbf{B}_2$ in each recovery which leads to an over-determined problem for each section estimate, yielding good noise robustness. The optimal thresholds in (5.25) are selected for the SPLS estimator. The threshold is ±0.5 for the conventional sparse recovery algorithms because these CS estimators are able to yield an exact signal recovery with high probability. In other words, they are unbiased with a high probability.

Fig. 43 shows the RMS of time-delay estimation error in the proposed interference-robust radar receiver as a function of the number of channels, with different wireless interference strengths parameterized by SIR. Fig. 44 shows the radar curves when the SNR is 6dB. The figures show that there is an optimal number of channels for a given interference strength to achieve an optimal time-delay estimation error, and the corresponding joint of probability of detection (Pd) and probability of false alarm (Pfa).

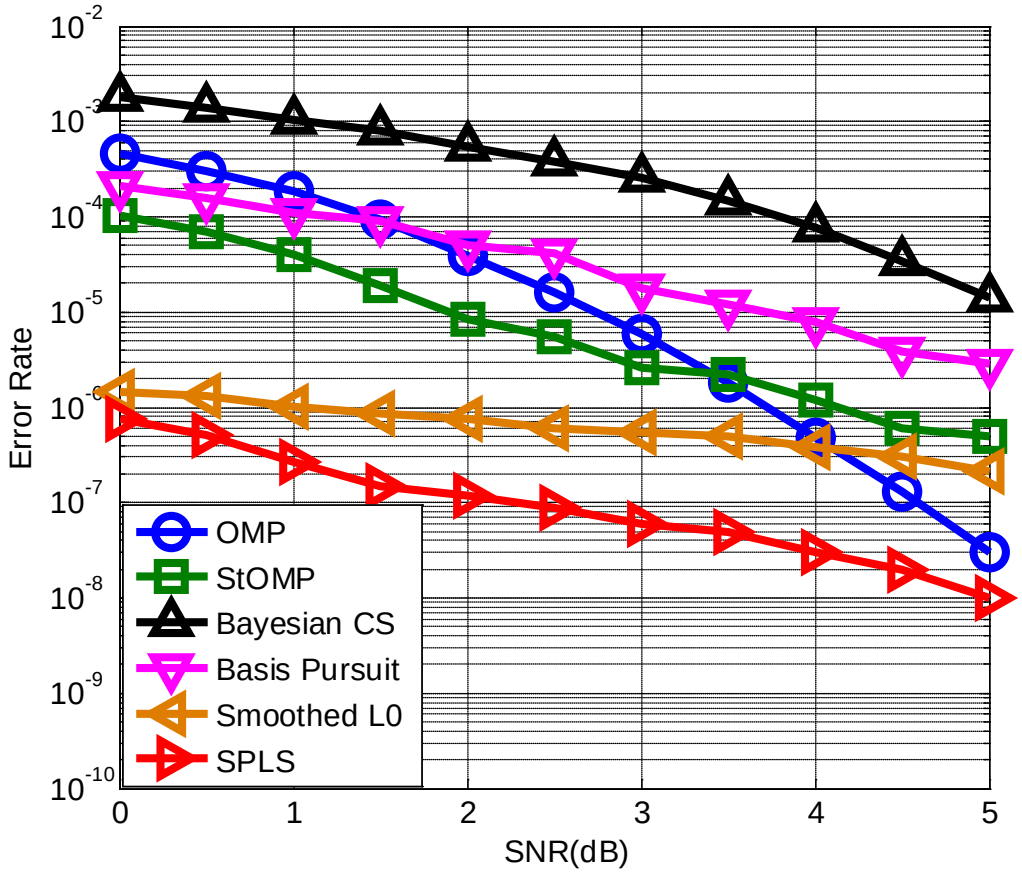

Fig. 42. Error rate (ER) of the recovered signal after amplitude detection using different CS signal reconstruction algorithms at a sub-Nyquist sampling ratio (SSR) of 13%.

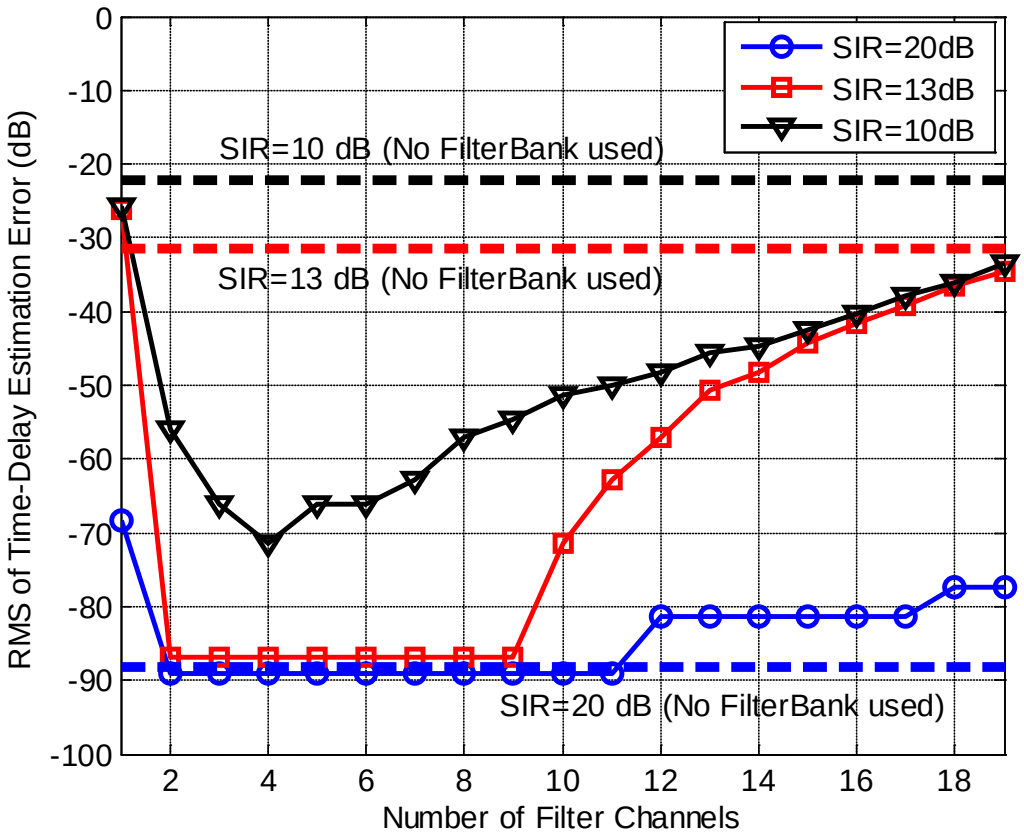

Fig. 43. RMS time delay estimation error performance as a function of the number of channels used, parameterized by the radar signal to interference power ratio (SIR).

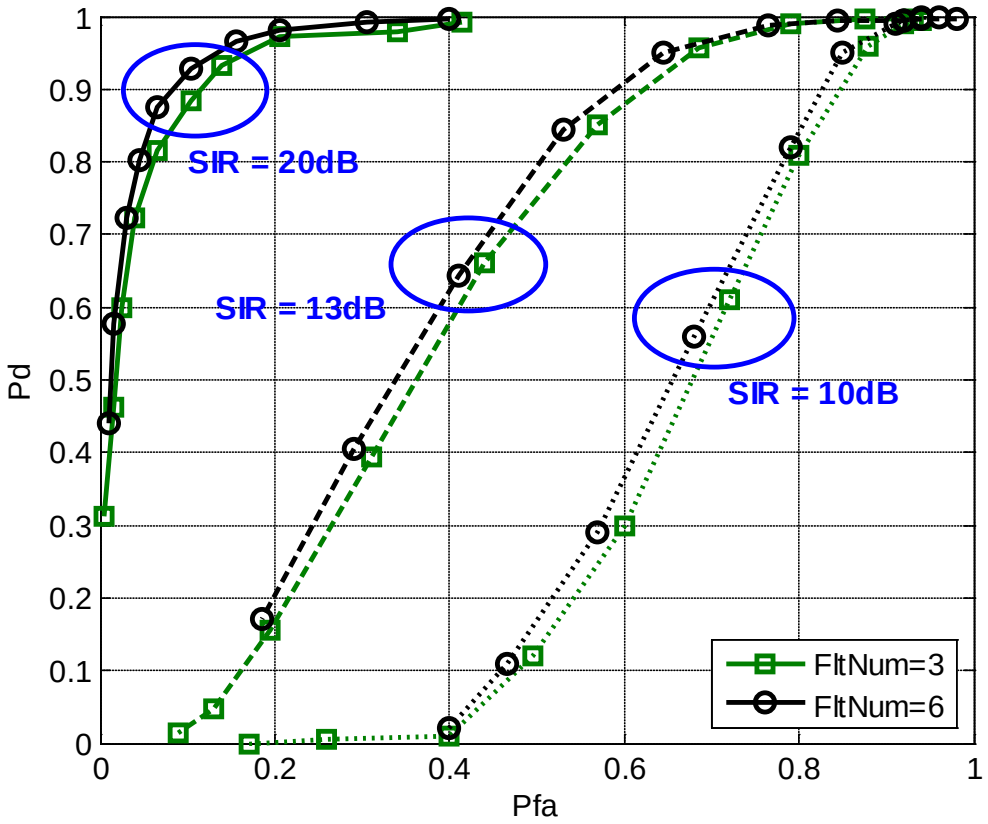

Fig. 44. Probability of detection (Pd) vs. Probability of false alarm (Pfa) parameterized by radar signal power to communication interference power ratio (SIR) and the number of filters (FltNum) used from the receiver filter-bank.

Fig. 43 and Fig. 44 show that there is an optimal number of channels for a given interference and SNR levels to achieve a desired T_{rms} and combination of Pd and Pfa. The probability of false alarm will be reduced by taking at least 6 detections (which brings the Pfa from 0.1 (see Fig. 44) to the target Pfa of 10-6 (see Table 5). This can be easily accomplished in practice in a multi-antenna radar configuration where all the antennas independently obtain range estimates. Better performance can also be obtained in MIMO radar as it is well explained in the extensive study [104] that reveals that the Pfa will be improved by at least two orders of magnitude by a simple 4-by-4 MIMO setting. These enhanced techniques will be essential in a vehicle-to-vehicle radar system with fast changing scenarios.

VI.B. Low-Power Portable Diagnostic Ultrasound Imaging

VI.B.1. Ultrasound Imaging Background

Diagnostic ultrasound imaging systems have many important advantages, for example, wide view angle, and they are noninvasive with no radiation [107], in contrast with other popular medical imaging techniques such as endoscopy, tomography, and x-rays. However, the ultrasound acoustic wave propagation experiences considerable attenuation and speckle distortion when imaging human tissues, resulting in a very low

signal-to-interference-plus-noise ratio (SINR). To accomplish high-quality imaging, conventional diagnostic ultrasound systems usually employ a large transducer array and a beamformer in both the transmitter and receiver [107]. While digital beamforming at the receiver is inherently more flexible and potentially more accurate, this requires Nyquist sampling over all sensors, and fine time resolution for time-delay compensation in the beamformer. Fig. 45 illustrates the architecture of a conventional digital beamformer with interpolation filters. Some commercial ultrasound analog front-ends employ sigma-delta ADCs, which include oversampling technique in the sampling stage. This architecture is typically implemented in a relatively large form factor and has high power consumption [107].

The growing use of ultrasound in daily clinical imaging and emergency healthcare motivates the development of portable and low-cost diagnostic ultrasound systems. State-of-the-art solutions are restricted to a small transducer array ($\leq$ 32 elements) and a low carrier frequency ($\leq$ 4MHz) [108]. Imaging quality in portable ultrasound reflects the fact that the carrier frequency limits both lateral and axial resolution, and that the transducer size limits the maximum angular resolution [109].

The multiple parallel data channels architecture requires high power for data conversion and presents an excessive data volume at the mixed-signal interface. Nyquist rate sampling of each transducer element is compulsory in a conventional digital beamforming architecture, and a high carrier frequency requires high-speed ADCs to avoid image aliasing. As a result, the aggregated data volume becomes formidable for a portable ultrasound system, and it is a significant challenge to increase the image quality

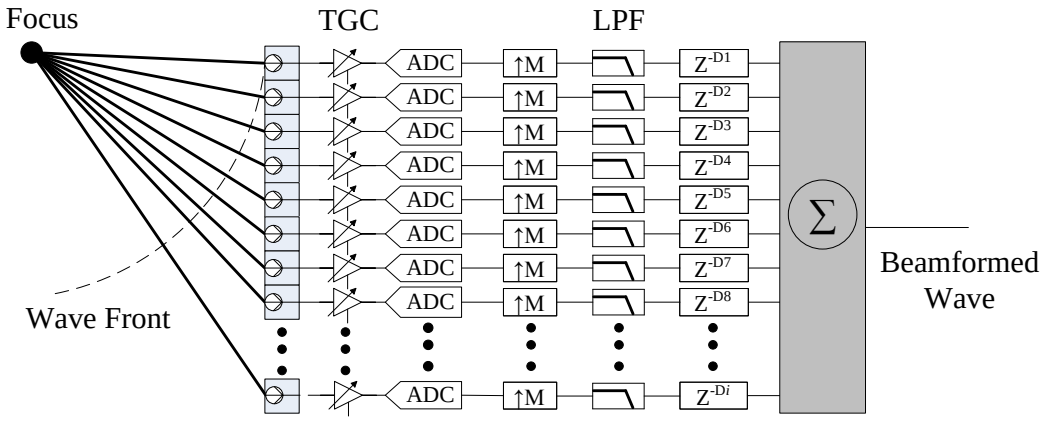

Fig. 45. Architecture of the digital ultrasound beamformer with interpolation filters.

in such systems. For example, data volume at the ADC outputs easily exceeds 30Gbps in an ultrasound system with 128 transducers, 10MHz carrier frequency and 12-bit ADCs. This very high data rate requires high-speed links between the analog front-end and digital processing unit, which further increases the system power and circuit area.

Various approaches to front-end data volume compression have been reported for ultrasound imaging systems [110–112], [106]. The authors in [110] exploit the fact that ultrasound signals are modulated onto a carrier so sampling of its baseband equivalent reduces the data volume; this approach requires two signal processing channels for I/Q processing for every transducer element and is subject to the Nyquist criterion. In [111], the authors compressed the raw RF ultrasound data and/or the baseband data using JPEG and JPEG2000 techniques. This technique also requires Nyquist sampling as the first stage. In [112], a sub-Nyquist sampling front-end was proposed by modeling ultrasound

signals in a finite rate innovation framework. This achieves 8-fold data compression at the expense of a collection of dedicated pre-conditioning filters ahead of the ADCs. In [106], the authors adopt compressive sensing for the ultrasound signals, utilizing a group-based total variation signal reconstruction algorithm that is relatively high-cost and adds considerable computational overhead if used with a large transducer array.

VI.B.2. Asynchronous Compressed Beamformer

In this sub-section, we present a low-complexity low-power asynchronous compressed beamformer (ACB) for portable diagnostic ultrasound. Fig. 46 illustrates the architecture of the proposed ACB. Leveraging the asynchronous sampling and CS framework, we optimize the hardware complexity and power consumption of the entire signal processing chain, including front-end sampling, mid-end beamforming, and back-end signal recovery for image display. Specifically, asynchronous sampling improves energy efficiency by reducing the duty cycle of the front-end circuits as the hardware is only active on demand. The CT-TE (shown in Fig. 9) scheme converts signal variations to high-rate ternary timing signals [64], which eliminates interpolation filters and/or CORDIC units needed in a conventional digital beamformer. The DRS-I is employed and optimized to exploit the sparsity of the ultrasound echoes, which exhibits many advantages such as low power, ease of massive integration, and excellent linearity compared with other popular CS front-ends [37], [50]. A signal reconstruction algorithm is also introduced called split-projection least squares (SPLS). This avoids the typical CS-based high-cost and nonlinear signal reconstruction, and relies instead on a series of low-complexity and independent l_2-norm problems that are easily solved via LS

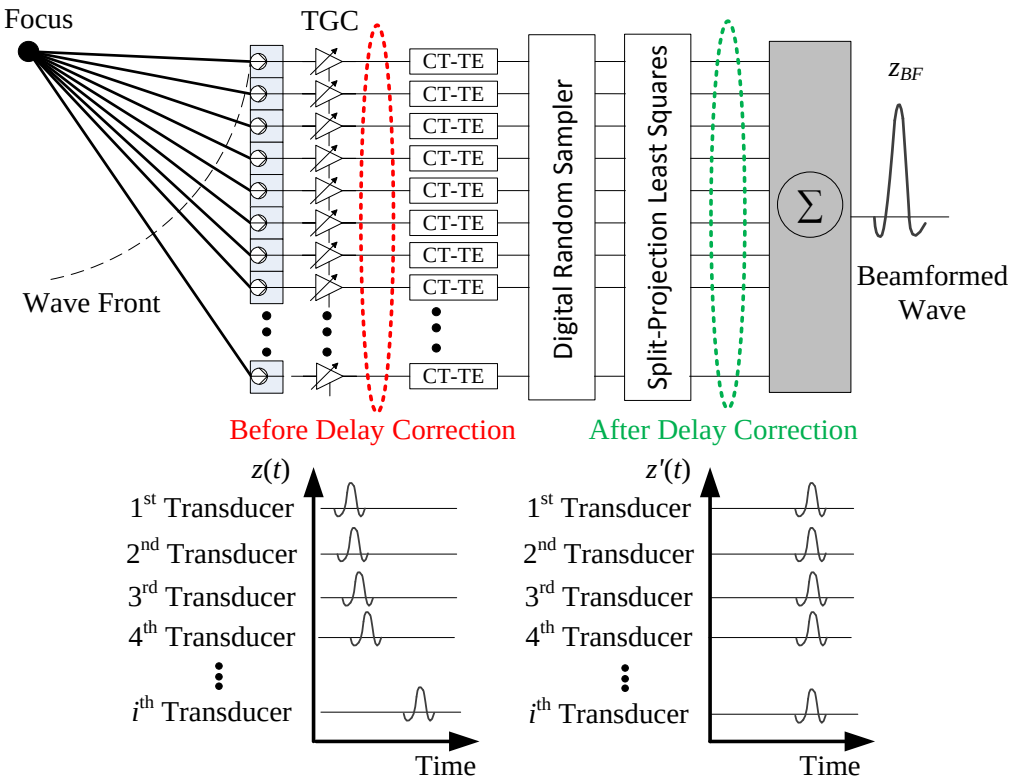

Fig. 46. Architecture of the proposed asynchronous compressed beamformer (ACB) for portable diagnostic ultrasound imaging systems.

estimators. The SPLS algorithm significantly decreases the computational cost in signal reconstruction, as is desired for real-time ultrasound signal processing and display.

Diagnostic ultrasound systems employ a large transducer array and beamforming for good imaging quality. In every scan, part or all of the transducer elements are stimulated to emit ultrasound. The geometry of the ultrasound transducers is such that each element hears from a particular focus point at different time instants. Before beamforming via coherent summation, these delay variances are compensated based on

the Euclidian distance difference. Let $z_i(t)$ and t_{Di} denote the signal from the i^{th} transducer element and the associated delay compensation, respectively. Then, the beamformed signal is

$$z_{BF}(t) = \sum_i z_i(t - t_{Di}) \quad . \tag{6.16}$$

Equation (6.16) is commonly implemented in digital circuits in a modern diagnostic ultrasound system where dedicated digital modules should be employed for fine timing resolution before time delay compensation, such as interpolation filters [107], or CORDIC units [110]. The number of these digital modules is proportional to the transducer array size. Therefore, a large number of parallel channels complicates the digital design and increases power consumption.

Recently, the CT-TE scheme has been proposed to convert the pulsed signal variations to high-speed ternary timing signals, that results in a low sampling rate by exploiting sparsity in time [64], [106]. The adder and accumulator in the DRS-I (Fig. 10) are both asynchronous logic. As studied in [64], the CT-TE scheme works at a high rate to satisfy the signal slew rate requirement. Such a high-speed operation, potentially even higher than the Nyquist rate, is an excellent fit for diagnostic ultrasound because the resulting high-rate timing signals remove the need for interpolation filters or CORDIC units processing.

The high-rate ternary timing signal actually has a low information rate due to the sparsity of ultrasound echo signals in a scattering environment. Thus the CS framework can be integrated into the front-end for data compression. Due to the ternary state of $x(t)$, a multi-channel DRS-I is employed and optimized in the proposed ACB, which is shown

in Fig. 47. Specifically, the inner product of ternary timing signal $x(t)$ and chipping sequence $p_c[n]$ is implemented by a shift register and an accumulator. This brings the scaling benefits of digital circuitry, including low power, ease of massive integration, and excellent linearity, and is considerably less complex that other CS sampling schemes such as the random demodulator [50] or modulated wave converter [37]. We emphasize that the time delay compensation is carried out on $p_c[n]$ rather than $x(t)$ in the proposed ACB scheme. This can be implemented via a first-in-first-out (FIFO) module to store the random sequence output from the linear feedback shift registers (LFSR). The delay compensator in each transducer selects the correct tap for the chipping sequence. This architecture enables an identical randomized measurement matrix $\mathbf{\Phi}$ across the entire transducer array. This unique feature offers dramatic savings in computational cost for multi-channel CS signal recovery, which will be analyzed in detail in the following.

The proposed DRS-I employs a FIFO module to buffer the high-rate chipping sequence and to adjust the proper time delay between each transducer element. The FIFO depth should be sufficiently large to accommodate the largest possible time delay between any two transducer elements during the dynamic focusing. Denoting Δr as the largest possible difference in path length between any two transducer elements during the dynamic focusing, the required FIFO depth is

$$\text{FIFO depth } 1 = \frac{\Delta r}{c} \cdot \frac{1}{T_1} = \frac{\Delta r}{c} f_{Nyquist} \cdot \text{OSR}_1 \ , \tag{6.17}$$

where c is ultrasound speed which is assumed to be a constant for analysis, T_1 is the clock period of the chipping sequence, $f_{Nyquist}$ is the Nyquist sampling rate, and OSR_1 is

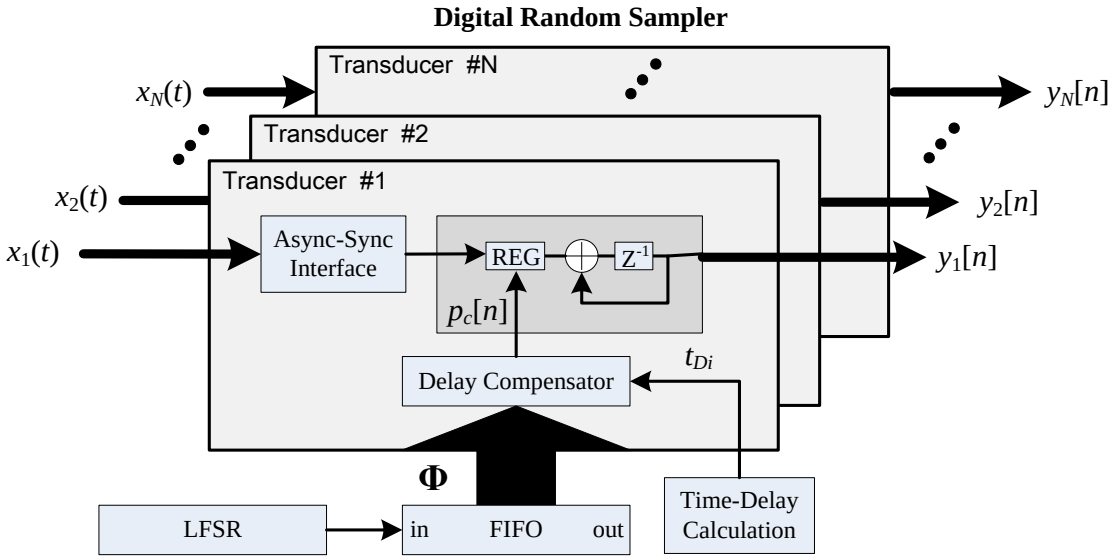

Fig. 47. Block diagram of the multi-channel first type digital random sampler (DRS-I) in the proposed asynchronous compressed beamformer.

the oversampling ratio applied in the high-rate CT-TE scheme relative to $f_{Nyquist}$. As will be discussed in next sub-section, an OSR_1 of 500 is generally sufficient for a 12-bit CT-TE ultrasound scheme. The conventional digital ultrasound beamformer in Fig. 45 employs an interpolation filter and a FIFO module in each channel for time-delay compensation, which requires an accumulated FIFO depth of

$$\text{FIFO depth } 2 = \frac{\Delta r}{c} \cdot \frac{1}{T_2} \cdot Num = \frac{\Delta r}{c} f_{Nyquist} \cdot \text{OSR}_2 \cdot Num \quad . \tag{6.18}$$

where OSR_2 is the interpolation rate and *Num* is the number of transducer elements. OSR_2 has a rule of thumb value of 16 or larger for fine timing resolution [107]. Comparing Eqs. (6.17) and (6.18), we see that the proposed multi-channel DRS-I has

better trade-off in terms of FIFO hardware cost when employing a large transducer array, e.g., say the number of transducer elements is larger than or equal to 32.

The optimized DRS-I module is even more promising for a multi-channel compressive sensing ultrasound system as only one matrix inverse, e.g., $(\mathbf{B}_2^T\mathbf{B}_2)^{-1}$, is mandatory in each section recovery for the entire transducer array, whereas complexity increases linearly with the number of transducer elements for other CS sampling schemes [111], [112], [106]. This is because the proposed multi-channel DRS-I applies time-delay compensation to the random sensing matrix rather than the input, resulting in an identical measurement matrix $\mathbf{\Phi}$ for different transducer elements, as illustrated in Fig. 47.

VI.B.3. Numerical Results

The point spread function (PSF) and contrast-to-noise ratio (CNR) of an ultrasound imaging system using the CT-TE scheme and the DRS-I are evaluated using the Field II MATLAB toolbox [113], [114]. We choose a transducer center frequency of 3MHz, a sampling rate of 100MHz, 128 transducer elements with kerf of 0.1mm, element height of 5mm, and element width of one wavelength. The gap between two adjacent transducer elements is called kerf. Define the sub-Nyquist sampling ratio (SSR) as the ratio of the actual sampling rate in the DRS-I to the Nyquist sampling rate, given by SSR = f_s / $f_{Nyquist}$. We define the signal-to-noise ratio (SNR) as the power ratio of the signal and the observation noise.

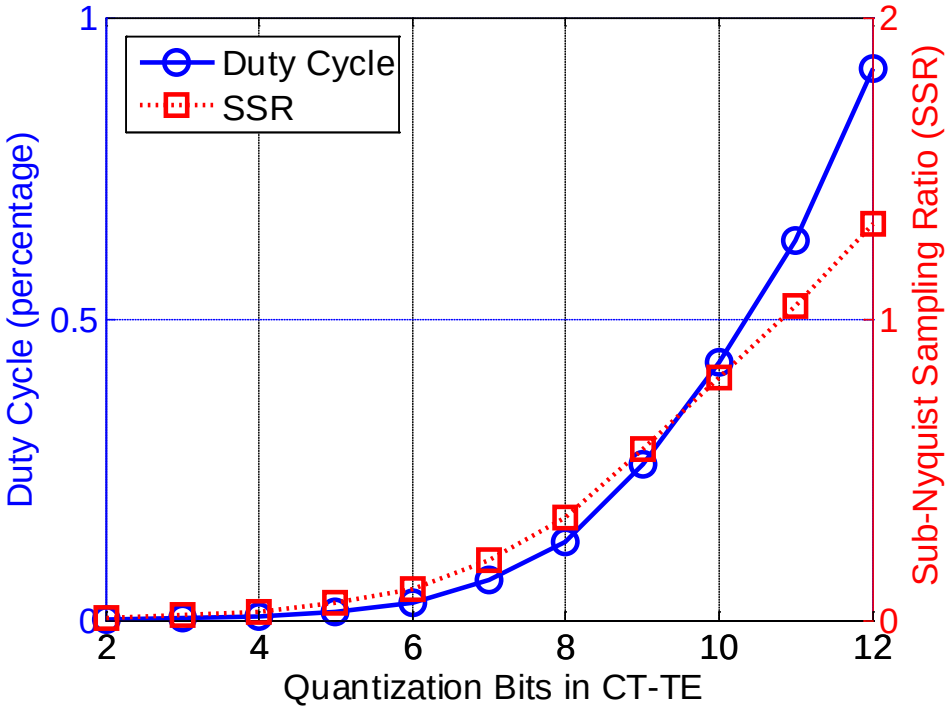

Fig. 48. Duty cycle versus sub-Nyquist sampling ratio (SSR) in the DRS-I for different quantization bits in the CT-TE. The imaging target consists of 5-point phantoms.

Fig. 48 shows the duty cycle in percentage versus the sub-Nyquist sampling ratio (SSR) of the DRS for different number of quantization bits in the CT-TE, when imaging 5-point phantoms placed with a distance of 20 mm starting at 30 mm from the transducer surface. The oversampling rate in the CT-TE scheme is 100 to accommodate the slew rate requirement in a (maximum) 12-bit CT-TE scheme. Fig. 49 compares the ultrasound imaging of a 5-point phantom by 12-bit ADC, and the proposed ACB with a 3-bit and a

5-bit CT-TE scheme. In Fig. 49 (b), we observe tiny “spikes” in the middle of the point phantom, which is distortion introduced by the granular noise effect in the CT-TE when the number of quantization bits is small. By increasing it to 5, the “spike” is significantly suppressed, as seen in Fig. 49 (c). As shown in Fig. 48, the 5-bit CT-TE scheme has a duty cycle of 0.15% and an SSR of 0.059 in capturing 5-point phantom signals.

The CNR is a useful metric for describing the signal amplitude relative to the ambient noise in an image [115]. Fig. 50 shows ultrasound imaging results of a disk-shape object with a scattering coefficient 10 times higher than that of the background medium, which is assumed to be standard normally distributed. The scan is fulfilled by a 192-element transducer, using 64 active elements with a Hanning apodization in both transmit and receive. The transducer element height is 5mm, the width is a wavelength and the kerf 0.05mm. The definition of CNR metric is described in [115] and given by

$$\mathrm{CNR} = \frac{\overline{x}_t - \overline{x}_{bg}}{\sigma_{bg}} \quad , \tag{6.19}$$

where $\bar{x}_t$ and $\bar{x}_{bg}$ is the averaged gray scale of a region of interest (ROI) in the disk, and that in an ROI in the background, respectively, and σ_{bg} is the standard deviation of the background noise. Fig. 50 (a) and (b) show the imaging result using a 12-bit 100MHz sampling rate ADC and 5-bit CT-TE scheme, respectively. The CNR is calculated to be 2.93 in (a), and 2.80 in (b), respectively, according to Eq. (6.19). The proposed 5-bit CT-TE scheme introduces some granular effects in Fig. 50 (b) but maintains comparable (less than 5% difference) CNR performance and exhibits a 12-fold data volume reduction when compared to a 12-bit conventional ADC due to an SSR of 0.081.

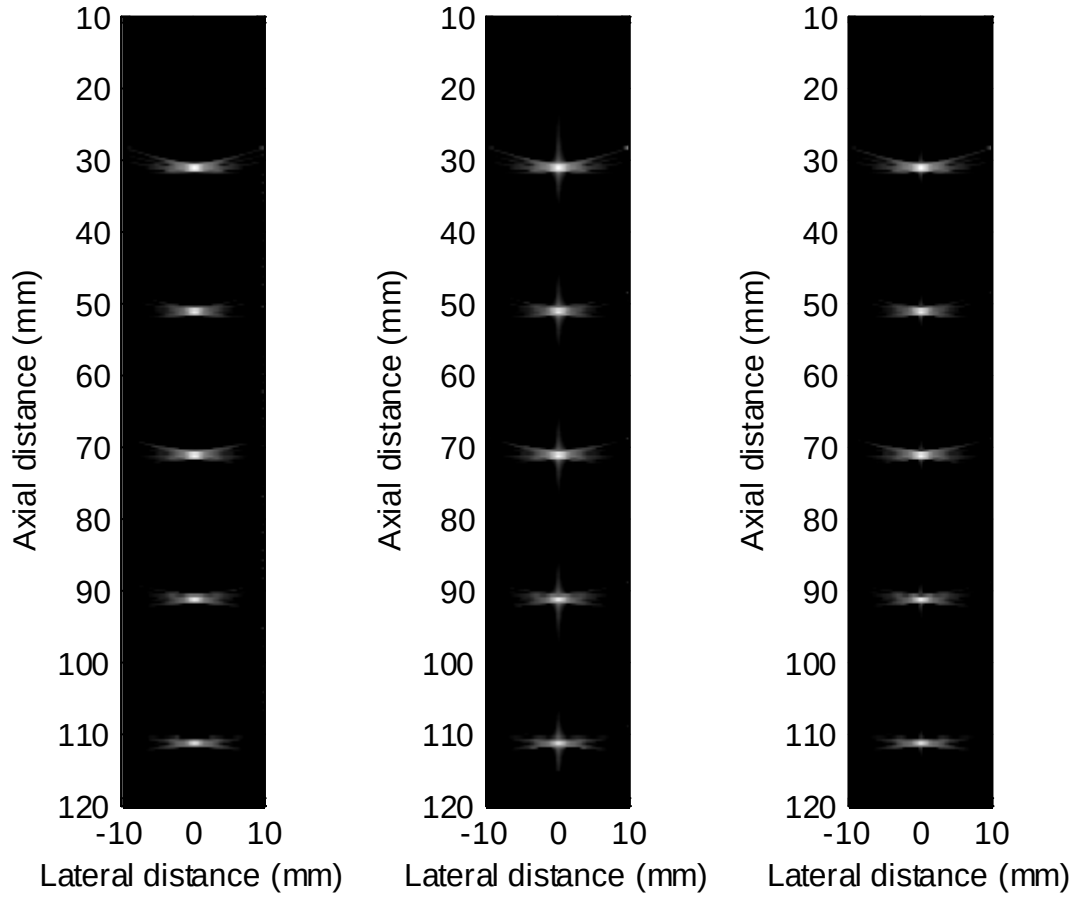

(a) (b) (c)

Fig. 49. Ultrasound imaging of 5-point phantoms with a spacing of 20 mm starting at 30 mm from the transducer surface: (a) conventional 12-bit 100MHz sampling rate ADC; (b) 3-bit quantization in the CT-TE, SSR = 0.016; (c) 5-bit quantization in the CT-TE, SSR = 0.059.

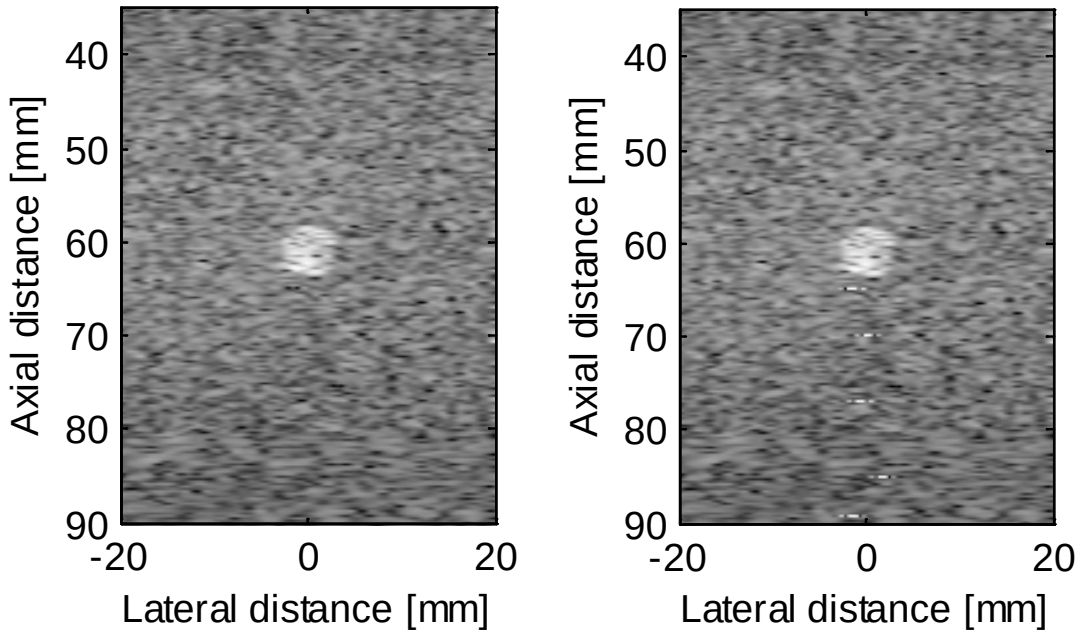

(a) (b)

Fig. 50. Ultrasound imaging of a highly scattering disk-shape object: (a) conventional 12-bit 100MHz sampling rate ADC, CNR = 2.93; (b) 5-bit quantization in the CT-TE, CNR = 2.80, SSR = 0.081.

In addition to the simple objects like the point phantom and disk-shape phantom, the proposed ACB shown in Fig. 46 is also tested with experimentally captured ultrasound data using a 64-element transducer array at 7.5MHz carrier frequency. The ultrasound signals were saved with a 30MHz sampling rate and 12-bit integer format. A clock rate of 500 times the ultrasound Nyquist rate is adopted in the proposed multi-channel DRS-I to accommodate the slew rate requirement in a (maximum) 12-bit CT-TE scheme. Fig. 51 illustrates the duty cycle in percentage versus SSR of the DRS-I when a quantization bit in the CT-TE scheme changes. The resulting ternary timing signals have an average sparsity of 0.13% in 8-bit CT-TE. As analyzed in Chapter III, the inner product calculation becomes trivial for all zero-valued inputs as a finite input multiplying zero always returns zero. Therefore, the duty cycle of the digital accumulator in the DRS-I is 0.13%. The sparsity increases as the number of quantization bits in the CT-TE scheme increases, as does the duty cycle. But, as shown in Fig. 51, the duty cycle remains small even for a 12-bit CT-TE, yielding 2.13%. The sparse ternary signals enable a sub-Nyquist sampling even with the 500 time oversampling clock. Fig. 51 also shows a duty cycle of 0.04% for 5-bit CT-TE and an SSR of 0.11, i.e., a 9-fold data compression compared with Nyquist sampling.

Note that a 5-bit CT-TE with an oversampling ratio of 500 have the same in-band quantization noise power as a 13-bit Nyquist-rate ADC because oversampling spreads the quantization noise into a much broader bandwidth. From these results, we adopt the 5-bit CT-TE and SSR of 0.11 in the following numerical results.

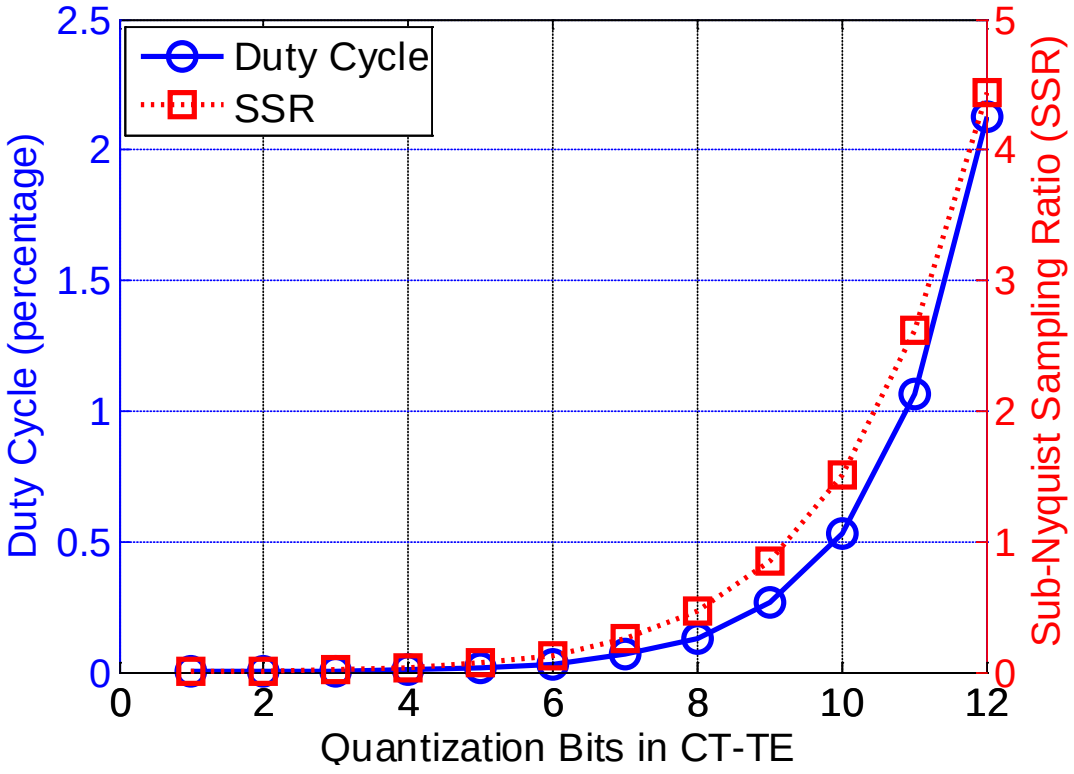

Fig. 51. Duty cycle versus the sub-Nyquist sampling ratio (SSR) of the multi-channel DRS-I for different number of quantization bits in the CT-TE scheme.

Fig. 52 compares the error rate of the ternary timing signal's recovery using different CS estimators in heavy noise (0dB-5dB SNR). The optimal thresholds in (5.25) are selected for the SPLS estimator. For comparison, the threshold is set to ±0.5 for the conventional sparse recovery algorithms as these CS estimators are able to yield an exact (but noisy) signal recovery with high probability. In other words, they are unbiased with a high probability, allowing simple choice of threshold following reconstruction.

10,000 independent simulations are carried out for the Monte-Carlo analysis. In Fig. 52, the SPLS estimator achieves the lowest error rate in the low SNR range, where ultrasound signals often reside. This occurs because SPLS employs a "tall" matrix $\mathbf{B}_2$ for each section estimate leading to an over-determined problem which is robust to heavy noise, and hence a good fit for this application. In addition, the performance difference between the SPLS algorithm with and without interference pruning does not appear until the SNR increases. This is because in the low SNR region, noise dominates the error rate. As the SNR increases, interference from the nonzero elements outside of the projection window influences both bias and variance of the SPLS estimator, as presented in (5.14) and (5.21). Nevertheless, Fig. 52 confirms the performance difference between the SPLS algorithm with and without interference pruning is small. The proposed SPLS algorithm functions well even in the data recovery from the first section, which can be considered to have a maximum interference from nonzero elements. However, due to the low complexity of the interference pruning step (a subtraction of sign adjusted measurement matrix from the measurements) and the resulting improved error rate at high SNR, we include the interference pruning step in **Algorithm 5.1**, as reflected in Fig. 25.

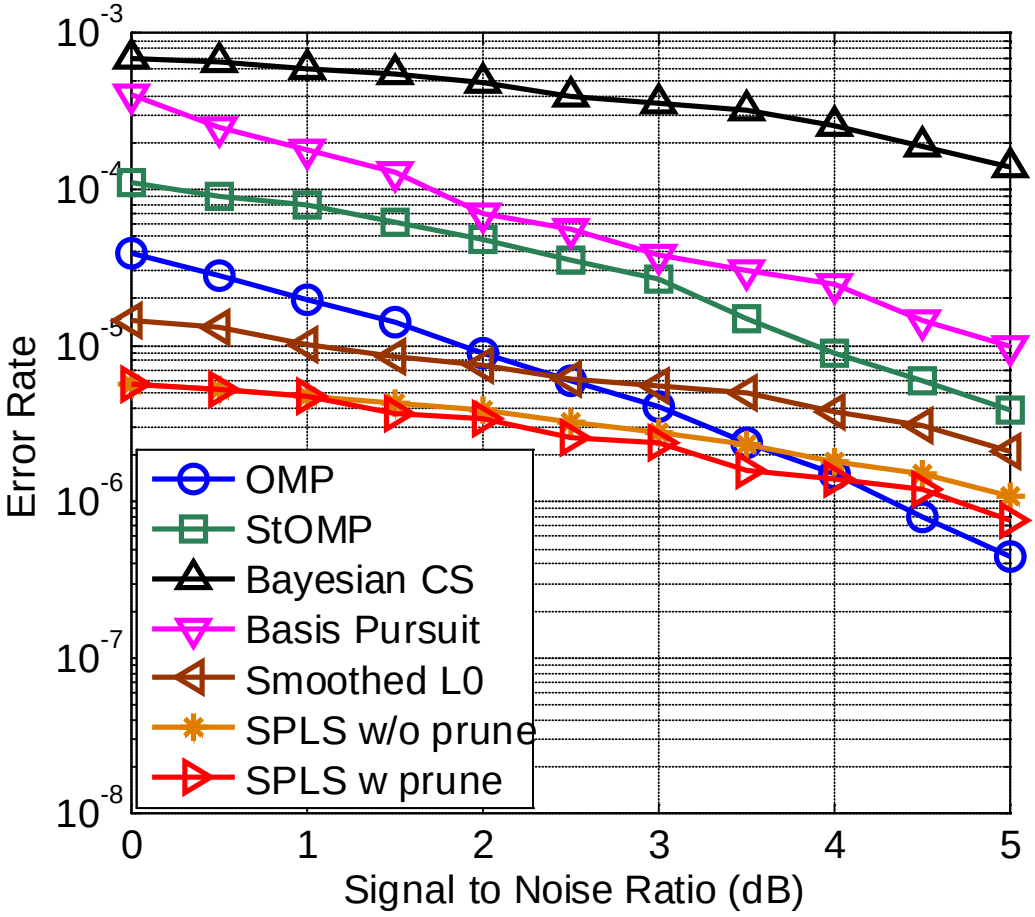

Fig. 52. Error rate of the recovered ternary signal after amplitude detection versus signal-to-noise ratio (SNR), with a sub-Nyquist sampling ratio (SSR) of 0.11.

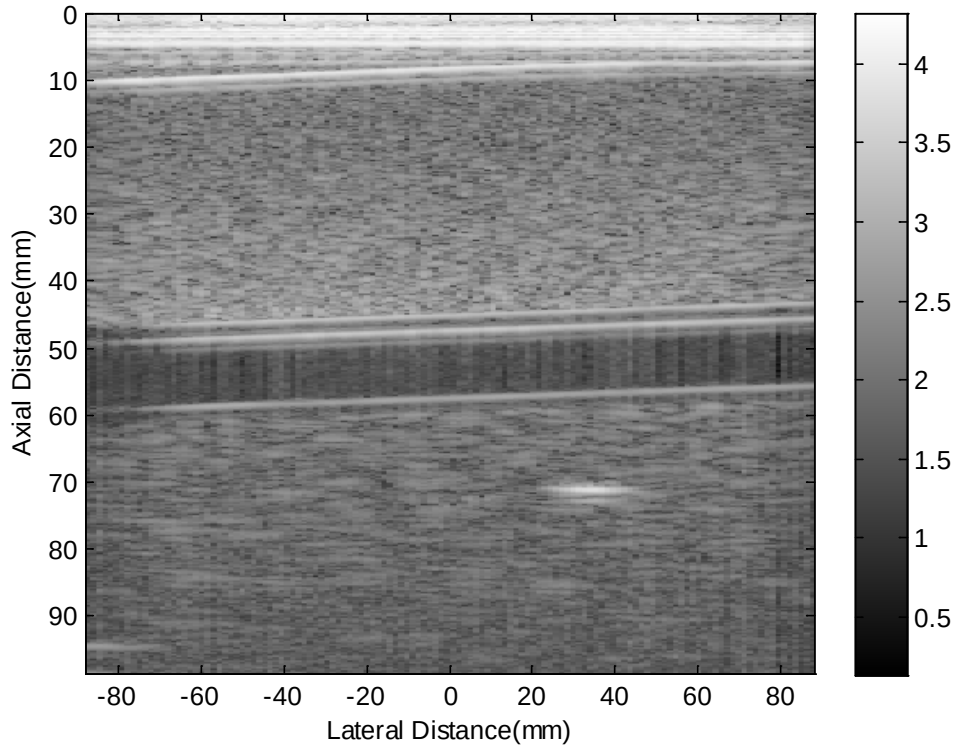

Fig. 53. B-mode ultrasound image with the proposed asynchronous compressed beamformer, 5-bit quantization in CT-TE, and the SSR is 0.11.

Fig. 53 illustrates the reconstructed B-mode ultrasound image (2D gray-scale imaging). Signal processing modules including apodization, clutter filtering, envelop detection and log compression, were implemented [107]. As shown in Fig. 53, the ultrasound signal reconstructed from the compressed measurements achieves a DR of more than 70dB, which confirms the 12-bit dynamic range ability in a 5-bit CT-TE scheme with a 500 times oversampling rate. In Fig. 53, a section of blood vessel can be distinguished from the neighboring tissues in the axial distance from 50mm to 60mm.

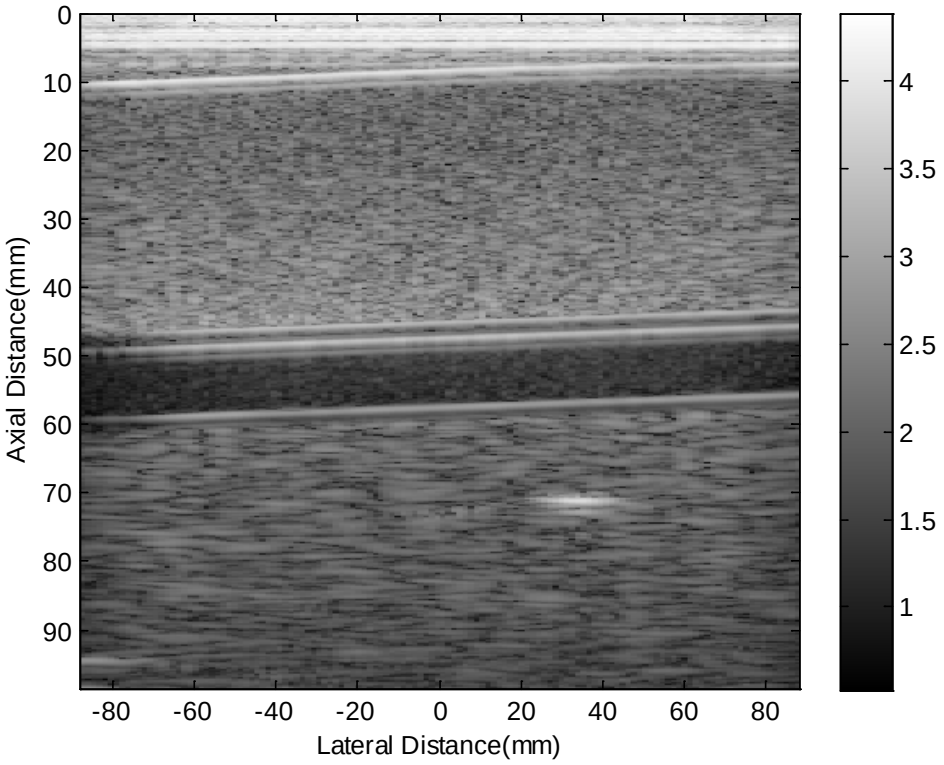

Fig. 54. B-mode ultrasound image with 12-bit Nyquist rate ADCs.

Fig. 55 illustrates the reconstructed color Doppler ultrasound image (2D Doppler imaging) from 7 frames of data. The velocity is calculated based on an auto-correlation technique and averaged between 7 frames for final display. The clear belt section appearing in the axial distance from 50mm to 60mm indicates that there is flowing liquid at an averaged velocity of 0.2mm/sec. Together with the B-mode image in Fig. 53, we may conclude that a section of blood vessel is present in the axial distance from 50 to 60mm, and the inside blood flow at a velocity of 0.2mm/sec.

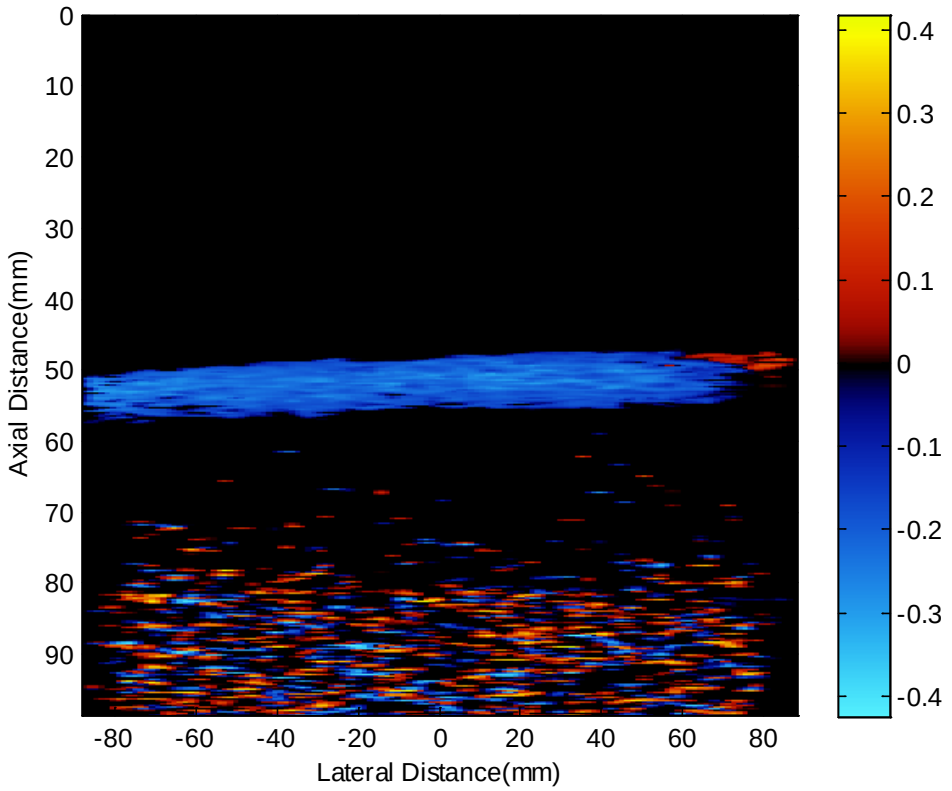

Fig. 55. Color Doppler ultrasound image with the proposed asynchronous compressed beamformer, 5-bit quantization in CT-TE, and SSR equal to 0.11.

For comparison, Fig. 54 and Fig. 56 show the B-mode and color Doppler ultrasound image with 12-bit Nyquist rate ADCs, respectively. There is little perceivable difference from the images processed via the proposed ACB and the SPLS algorithm. Color Doppler ultrasound imaging in Fig. 56 confirms an averaged velocity of 0.2mm/sec in the same area as that in Fig. 55. However, compared with full 12-bit Nyquist sampling, the proposed method exhibits a 9-fold data volume compression at the mixed-signal interface, and employs a 5-bit CT-TE that will require only 0.04% duty cycle of the digital accumulator in the DRS-I.

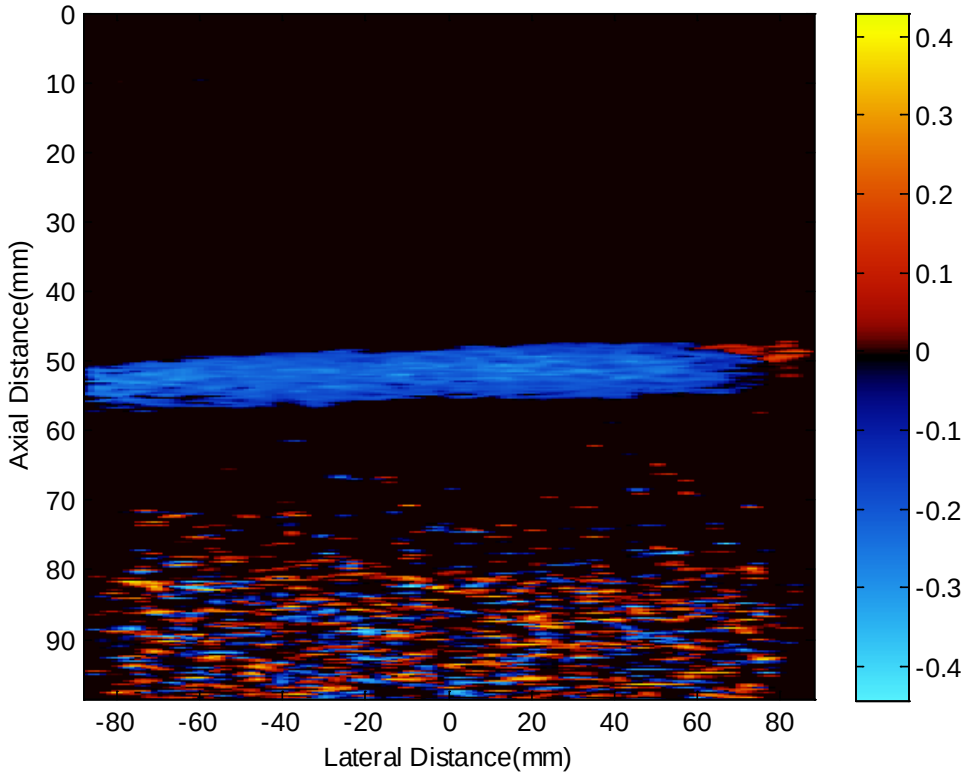

Fig. 56. Color Doppler ultrasound image with 12-bit Nyquist rate ADCs.

CHAPTER VII

CONCLUSIONS

Conventional analog-to-digital converters (ADCs) are restricted to the Shannon/ Nyquist sampling theorem and have to operate at or above the Nyquist rate in order to avoid image aliasing. As a result, sampling of very broadband signals can be extremely power-demanding or even technology impossible. Though many advanced digital signal processing (DSP) algorithms is capable of compressing the discrete samples volume, it is carried out at the digital domain which requires Nyquist-rate sampling as the first stage at the mixed-signal interface.

Compressive sensing (CS) technique integrates sampling and compression into one step as compressed sensing and facilitates a sub-Nyquist rate sampling of sparse and compressible signals. The original signals can be restored from compressed samples by a convex optimization problem. The existing CS framework has proved that it is reliable with probabilistic guaranteed signal reconstruction performance and universal to any sparse/compressible signals.

Nevertheless, there are challenges in hardware implementation of CS front-end and signal reconstruction algorithms in terms of power, performance and complexity. In this dissertation, we propose an asynchronous compressive sensing (ACS) front-end and two advanced signal reconstruction algorithms to address them. The ACS front-end includes a continuous-time ternary encoding (CT-TE) scheme and a digital random sampler (DRS). The CT-TE scheme converts amplitude variations into high-speed

ternary timing signals. And the DRS captures the ternary timing signals at sub-Nyquist rate by exploiting the sparsity of impulse-like signals. The ACS front-end exhibits many advantages such as low power, ease of massive integration, and excellent linearity in comparison to state-of-the-art CS front-ends, such as random demodulator, modulated wideband converter, etc.

In the signal reconstruction part, we propose two advanced signal reconstruction algorithms with different features. The first algorithm is group-based total variation (GTV). It follows the principle of total variation (TV) but introduces a regularized group-based total variation penalty in the objective function, which provides smaller mean squared error (MSE) and faster convergence rate than conventional TV schemes. The second algorithm is called split-projection least squares (SPLS). The SPLS avoids the typical CS-based high-cost and nonlinear signal reconstruction, and relies instead on a series of low-complexity and independent l_2-norm problems that are easily solved via least squares (LS) estimators. With the *prior* on ternary-valued amplitude, the proposed SPLS scheme significantly decreases the computational cost in signal reconstruction, as is desired for real-time CS signal processing and display.

In experiment study, we exploit performance of the ACS front-end and the SPLS scheme in two practical applications where compressed sampling at the mixed-signal interface is critical. The proposed ACS front-end has been further optimized depending on the actual requirements. Specifically, in the first application, we proposed multi-channel filter banks ACS front-end for the interference-robust radar with in-band wireless communication interference. With the presence of strong wireless interference,

the propose radar receiver performs reliable target detection with nearly 8-fold data volume compression compared with the Nyquist-rate ADCs. In the second application, we propose an asynchronous compressed beamformer (ACB) for low-power portable diagnostic ultrasound imaging systems. The ACB takes the advantages of the high-speed CT-TE scheme and achieves low-complexity compressed digital beamforming. The ACB scheme is tested with point phantom, disk phantom as well as the experiment data, which confirms a 9-fold data volume reduction in comparison to the Nyquist-rate ADCs, without significant perceptual loss on imaging results.

The theoretical analyses and numerical results presented in this dissertation have been published or currently under review in several IEEE journals and conference papers.

REFERENCES

[1] C. E. Shannon, "Communication in the presence of noise," *Proceedings of the IRE*, vol. 37, no. 1, pp. 10 – 21, Jan. 1949.

[2] F. Maloberti, *Data converters*, Springer, New York, United States, 2007.

[3] H. Sun, A. Nallanathan, C. Wang and Y. Chen, "Wideband spectrum sensing for cognitive radio networks: a survey," *IEEE Wireless Communications*, vol. 20, no. 2, pp. 74 – 81, Apr. 2013.

[4] B. Murmann, "ADC performance survey 1997-2013," [Online]. Available: http://www.stanford.edu/~murmann/adcsurvey.html, 2013.

[5] C. Lelandais-Perrault, T. Petrescu, D. Poulton, P. Duhamel, and J. Oksman, "Wideband, bandpass, and versatile hybrid filter bank A/D conversion for software radio," *IEEE. Trans. Circuits and Systems I*, vol. 56, no. 8, pp. 1772 – 1782, Aug. 2009.

[6] D. Asemani, J. Oksman, and P. Duhamel, "Subband architecture for hybrid filter bank A/D converters," *IEEE J. Selected Topics Signal Processing*, vol. 2, no. 2, pp. 191 – 201, Apr. 2008.

[7] E. Brunner, "How ultrasound system considerations influence front-end component choice," *Analog Dialogue*, vol. 36, no. 3, pp.1 – 4, 2002.

[8] S. Grgic, M. Grgic, B. Zovko-Cihlar, "Performance analysis of image compression using wavelets," *IEEE Trans. Industrial Electronics*, vol. 48, no. 3, pp. 682 – 695, Jan. 2001.

[9] A. Averbuch, D. Lazar, and M. Israeli, “Image compression using wavelet transform and multiresolution decomposition,” *IEEE Trans. Image Processing*, vol. 5, no. 1, pp. 4 – 15, Jan. 1996.

[10] R. Talluri, K. Oehler, T. Barmon, and J. D. Courtney, “A robust, scalable, object-based video compression technique for very low bit-rate coding,” *IEEE Trans. Circuits and Systems for Video Technology*, vol. 7, no. 1, pp. 221 – 233, Feb.1997.

[11] S. M. S. Jalaleddine, C. G. Hutchens, R. D. Strattan, and W. Coberly, “ECG data compression techniques - a unified approach,” *IEEE Trans. Biomedical Engineering*, vol. 37, no. 4, pp. 329 – 343, Apr. 1990.

[12] A. Yadollahi, and Z. Moussavi, “Respiratory sounds compression,” *IEEE Trans. Biomedical Engineering*, vol. 55, no. 4, pp. 1336 – 1343, Apr. 2008.

[13] E. J. Candès, M. B. Wakin, “An introduction to compressive sampling,” *IEEE Signal Processing Magazine*, vol. 25, no. 2, pp. 21 – 30, Mar. 2008.

[14] D. Donoho, “Compressed sensing,” *IEEE Trans. Information Theory*, vol. 52, no. 4, pp. 1289-1306, Apr. 2006.

[15] M. Lustig, D. L. Donoho, J. M. Santos, and J. M. Pauly, “Compressed sensing MRI,” *IEEE Signal Processing Magazine*, vol. 25, no. 2, pp. 72 – 82, Mar. 2008.

[16] Z. Ashouri, and S. Shirani, “Video super resolution using contourlet transform and bilateral total variation filter,” *IEEE Trans. Consumer Electronics*, vol. 59, no. 3, pp. 604 – 607, Aug. 2013.

[17] Y. Mostofi, “Compressive cooperative sensing and mapping in mobile networks,” *IEEE Trans. Mobile Computing*, vol. 10, no. 12, pp. 1769 – 1784, Dec. 2011.

[18] A. Eftekhari, J. Romberg, and M. B. Wakin, "Matched filtering from limited frequency samples," *IEEE Trans. Information Theory*, vol. 59, no. 6, pp. 3475 – 3496, Jun. 2013.

[19] F. J. Herrmann, M. P. Friedlander, and O. Yilmaz, "Fighting the curse of dimensionality: compressive sensing in exploration seismology," *IEEE Signal Processing Magazine*, vol. 29, no. 3, pp. 88 – 100, May 2012.

[20] E. J. Candès, Y. C. Eldar, D. Needell, and P. Randall, "Compressed sensing with coherent and redundant dictionaries," *Applied and Computational Harmonic Analysis*, vol. 31, no. 1, pp. 59 – 73, May 2010.

[21] D. L. Donoho and X. Huo, "Uncertainty principles and ideal atomic decomposition," *IEEE Trans. Information Theory*, vol. 47, no. 7, pp. 2845 – 2862, Nov. 2001.

[22] M. Elad and A. M. Bruckstein, "A generalized uncertainty principle and sparse representation in pairs of bases," *IEEE Trans. Information Theory*, vol. 48, no. 9, pp. 2558 – 2567, Sep. 2002.

[23] D. L. Donoho, and M. Elad, "Optimally sparse representation in general (non-orthogonal) dictionaries via l_1 minimization," *Proc. Natl. Acad. Sci. USA*, vol. 100, no. 5, pp. 2197 – 2202, Mar. 2003.

[24] E. J. Candès, J. Romberg, and T. Tao, "Robust uncertainty principles: Exact signal reconstruction from highly incomplete Fourier information," *IEEE Trans. Information Theory*, vol. 52, no. 2, pp. 489 – 509, Jan. 2006.

[25] R. DeVore, “Deterministic constructions of compressed sensing matrices,” *J. Complexity*, vol. 23, pp. 918 – 925, 2007.

[26] R. G. Baraniuk, M. Davenport, R. A. DeVore, and M. Wakin, “A simple proof of the restricted isometry property for random matrices,” *Constructive Approximation*, vol. 28, pp. 253 – 263, Jan. 2008.

[27] J. N. Laska, S. Kirolos, M. F. Duarte, T. S. Ragheb, R. G. Baraniuk, and Y. Massoud, “Theory and implementation of an analog-to-information converter using random demodulation,” in *Proc. of IEEE Int. Symposium on Circuits and Systems*, pp. 1959–1962, May 2007.

[28] S. Kirolos, J. N. Laska, M. B. Wakin, M. F. Duarte, D. Baron, T. Ragheb, Y. Massoud, and R. G. Baraniuk, “Analog-to-information conversion via random demodulation,” *Proc. of IEEE Dallas Circuits and Systems Workshop*, Oct. 2006.

[29] A. Harms, W. U. Bajwa, R. Calderbank, “A constrained random demodulator for sub-Nyquist sampling,” *IEEE Trans. Information Theory*, vol. 61, no. 3, pp. 707 – 723, Feb. 2013.

[30] H. Mamaghanian, N. Khaled, D. Atienza and P. Vandergheynst, “Compressed sensing for real-time energy-efficient ECG compression on wireless body sensor nodes,” *IEEE Trans. on Biomedical Engineering*, vol. 58, no. 9, pp. 2456-2466, Sep. 2011.

[31] E. G. Allstot, A. Y. Chen, A. M. R. Dixon, D. Gangopadhyay and D. J. Allstot, “Compressive sampling of ECG bio-signals: quantization noise and sparsity considerations,” *IEEE Biomedical Circuits and Systems Conf.*, pp. 41-44, 2010.

[32] L. F. Polania, R. E. Carrillo, M. B. Velasco and K. E. Barner, “Compressed sensing based method for ECG compression,” in *Proc. of IEEE Int. Conf. on Acoustics, Speech, and Signal Processing*, pp. 761-764, Apr. 2011.

[33] Z. Yu, J. Zhou, M. Ramirez, S. Hoyos, and B. M. Sadler, “The impact of ADC nonlinearity in a compressive sensing receiver for frequency-domain sparse signals,” *J. of Physical Communication*, vol. 5, no. 2, pp. 196-207, Jun. 2012.

[34] X. Chen, Z. Yu, S. Hoyos, B. M. Sadler and J. Silva-Martinez, “A sub-Nyquist rate sampling receiver exploiting compressive sensing,” *IEEE Trans. Circuits Systems I*, vol. 58, no. 3, pp. 507-520, Mar. 2011.

[35] Z. Yu, S. Hoyos, and B. M. Sadler, “Mixed-signal parallel compressed sensing and reception for cognitive radio,” in *Proc. of IEEE Int. Conf. on Acoustics, Speech and Signal Processing*, pp. 3861–3864, Mar. 2008.

[36] M. Mishali, Y. C. Eldar, “Expected RIP: conditioning of the modulated wideband converter,” *IEEE Information Theory Workshop*, pp. 343 – 347, 2009.

[37] M. Mishali and Y. C. Eldar, “From theory to pratice: Sub-Nyquist sampling of sparse wideband analog signals,” *IEEE J. Selected Topics Signal Processing*, vol. 4, no. 2, pp. 375 – 391, Apr. 2010.

[38] S. Hoyos and B. M. Sadler, “Ultra-wideband analog to digital conversion via signal expansion,” *IEEE Trans. Vehicle Technol*ogy, vol. 54, no. 5, pp. 1609 – 1622, Sep. 2005.

[39] S. Hoyos, B. M. Sadler, and G. R. Arce, "Broadband multicarrier communications receiver based on analog to digital conversion in the frequency domain," *IEEE Trans. Wireless Communication*, vol. 5, no. 3, pp. 652 – 661, Mar. 2006.

[40] Y. C. Eldar, P. Kuppinger and H. Bolcskei, "Compressed sensing of block-sparse signals: uncertainty relations and efficient recovery," *IEEE Trans. on Signal Processing*, vol. 58, no. 6, pp. 3042 – 3054, 2010.

[41] W. Lu and N. Vaswani, "Modified basis pursuit denoising for noisy compressive sensing with partially known support," in *Proc. of IEEE Int. Conf. on Acoustics, Speech, and Signal Processing*, pp. 3926 – 3929, Apr. 2010.

[42] J. A. Tropp and A. C. Gilbert, "Signal recovery from random measurements via orthogonal matching pursuit," *IEEE Trans. Information Theory*, vol. 53, no. 12, pp. 4655 – 4666, Dec. 2007.

[43] D. Needell and J. A. Tropp, "CoSaMP: Iterative signal recovery from incomplete and inaccurate samples," *Applied and Computational Harmonic Analysis*, vol. 26 no. 3. pp. 301 – 321, 2009.

[44] D. Donoho, Y. Tsaig, I. Drori, and J. Starck, "Sparse solution for underdetermined linear equations by stagewise orthogonal matching pursuit," *IEEE Trans. on Information Theory*, vol. 58, no. 2, pp. 1094 – 1121, Feb. 2012.

[45] I. Daubechies, M. Defrise, and C. De Mol, "An iterative thresholding algorithm for linear inverse problems with a sparsity constraint," *Communications on Pure and Applied Mathematics*, vol. 57, no. 11, pp. 1413 – 1457, Aug. 2004.

[46] M.A.T. Figueiredo, R.D. Nowak, and S. J. Wright, "Gradient projection for sparse reconstruction: application to compressed sensing and other inverse problems," *IEEE J. Selected Topics in Signal Processing*, vol. 1, no. 4, pp. 586–597, Dec. 2007.

[47] E. J. Candès and T. Tao, "The Dantzig selector: statistical estimation when p is much larger than n," *Annals of Statistics*, vol. 35, no. 6, pp. 2313 – 2351, Dec. 2007.

[48] E. J. Candès, J. Romberg, and T. Tao, "Stable signal recovery from incomplete and inaccurate measurements," *Communications on Pure and Applied Mathematics*, vol. 59, no. 8, pp. 1207 – 1223, Mar. 2006.

[49] S. G. Mallat and Z. Zhang, "Matching pursuits with time-frequency dictionaries," *IEEE Trans. Signal Processing*, vol. 41, no. 12, pp. 3397 – 3415, Dec. 1993.

[50] J. A. Tropp, J. N. Laska, M. F. Duarte, J. K. Romberg and R. G. Baraniuk, "Beyond Nyquist: efficient sampling of sparse bandlimited signals," *IEEE Trans. on Information Theory*, vol. 56, no. 1, pp. 520 – 544, Jan. 2010

[51] J. A. Tropp, and S. J. Wright, "Computational methods for sparse solution of linear inverse problems," in *Proceedings of the IEEE*, vol. 98, no. 6, pp. 948-958, June 2010.

[52] A.C. Gilbert, M. J. Strauss, and R. Vershynin, "One sketch for all: fast algorithms for compressed sensing," in *Proc. 39th ACM Symposium on Theory of Computing*, June 2007.

[53] A. C. Gilbert, S. Guha, P. Indyk, S. Muthukrishnan, and M. J. Strauss, "Near optimal sparse Fourier representations via sampling," in *Proc. 34th ACM Symposium on Theory of Computing*, pp. 152 – 161, 2002.

[54] S. Ji, Y. Xue, and L. Carin, "Bayesian compressive sensing," *IEEE Trans. Information Theory*, vol. 56, no. 6, pp. 2346 – 2356, Jun. 2008.

[55] H. Mohimani, M. B. Zadeh, and C. Jutten, "A fast approach for overcomplete sparse decomposition based on smoothed L0 norm," *IEEE Trans. on Signal Processing*, vol.57, no.1, pp. 289 – 301, Jan. 2009.

[56] R. S. Katti, X. Ruan and H. Khattri, "Multiple-output low-power linear feedback shift register design," *IEEE Trans. Circuits Systems I*, vol. 53, no. 7, pp. 1487-1495, Jul. 2006

[57] O. H. Schmitt, "A thermionic trigger," *J. of Scientific Instruments*, vol. 15, no. 1, 1938.

[58] A. A. Lazar and L. T. Toth, "Perfect recovery and sensitivity analysis of time encoded bandlimited signals," *IEEE Trans. Circuits Systems I*, vol. 51, no. 10, pp. 2060 – 2073, Oct. 2004.

[59] N. S. Jayant and A. E. Rosenberg, "The preference of slope overload to granularity in the delta modulation of speech," *Bell System Technical Journal*, vol. 50, no. 10, Dec. 1971.

[60] A. S. Alvarado and J. C. Principe, "From compressive to adaptive sampling of neural and ECG recordings," in *Proc. of IEEE Int. Conf. on Acoustics, Speech, and Signal Processing*, pp. 633 – 636, Apr. 2011.

[61] P. E. Allen and D. R. Holberg, *CMOS analog circuit design*, Oxford University Press, 3rd edition, Aug. 2011.

[62] T. Jiang, W. Liu, F. Y. Zhong, C. Zhong and P. Y. Chiang, "Single-channel, 1.25-GS/s, 6-bit, loop-unrolled asynchronous SAR-ADC in 40nm-CMOS," *IEEE Custom Integrated Circuits Conference*, pp.1 – 4, Sep.2010.

[63] B. Razavi, *Design of analog CMOS integrated circuits*, McGraw-Hill Science/ Engineering/Math, 1st edition, Aug. 2000.

[64] J. Zhou, M. Ramirez, S. Palermo, and S. Hoyos, "Digital-assisted asynchronous compressive sensing front-end," *IEEE J. on Emerging and Selected Topics in Circuits and Systems*, vol.2, no.3, pp.482 – 492, Sep. 2012.

[65] J. Williams, and D. Thomas, *Digital VLSI design with Verilog: a textbook from Silicon Valley technical institute*, Springer, Jun. 2008.

[66] MIT-BIH arrhythmia database. (2005). URL: http://www.physionet.org/physiobank/database/mitdb/

[67] F. Chen, A. P. Chandrakasan, V. Stojanovic, "A signal-agnostic compressed sensing acquisition system for wireless and implantable sensors," *IEEE Custom Integrated Circuits Conference*, pp. 1 – 4, Sep. 2010.

[68] L. I. Rudin, S. J. Osher, and E. Fatemi, "Nonlinear total variation based noise removal algorithms," *Physica D*, vol. 60, no. 1 – 4, pp. 259–268, 1992.

[69] A. Chambolle, V. Caselles, M. Novaga, D. Cremers, and T. Pock, "An introduction to total variation for image analysis," Lecture notes, 2009, DOI: http://hal.archives-ouvertes.fr/hal-00437581/en/

[70] A. Chambolle, P. L. Lions, “Image recovery via total variation minimization and related problems,” *Numerische Mathematik*, vol. 76, no. 2, pp. 167 – 188, Apr. 1997.

[71] S. Osher and S. Esedoglu, “Decomposition of images by the anisotropic Rudin-Osher-Fatemi model,” *Commun. Pure Appl. Math.*, vol. 57, no. 12, pp. 1609 – 1626, Dec. 2004.

[72] T. Chan, S. Esedoglu, F. Park, and A. Yip, “Recent developments in total variation image restoration,” in Mathematical Models of Computer Vision, New York: Springer-Verlag, 2005.

[73] W. K. Allard, “Total variation regularization for image denoising, II. Examples,” *SIAM J. Imaging Sciences*, vol. 1, no. 4, pp. 400 – 417, Oct. 2008.

[74] Y. M. Huang, M. K. Ng, and Y. W. Wen, “A new total variation method for multiplicative noise removal,” *SIAM J. Imaging Sciences*, vol. 2, no. 1, pp. 20 – 40, Jan. 2009.

[75] W. Stefan, R. A. Renaut, and A. Gelb, “Improved total variation-type regularization using higher order edge detectors,” *SIAM J. Imaging Sciences*, vol. 3, no. 2, pp. 232–251, Apr. 2010.

[76] A. Chambolle, S. E. Levine, and B. J. Lucier, “An upwind finite- difference method for total variation-based image smoothing,” *SIAM J. Imaging Sciences*, vol. 4, no. 1, pp. 277–299, 2011.

[77] P. Getreuer, “Contour stencils: total variation along curves for adaptive image interpolation,” *SIAM J. Imaging Sciences*, vol. 4, no. 3, pp. 954–979, 2011.

[78] P. Blomgren, T. F. Chan, P. Mulet, and C. K. Wong, “Total variation image restoration: numerical methods and extensions,” in *Proc. IEEE ICIP*, pp. 384–387, 1997.

[79] G. Steidl, S. Didas, and J. Neumann, “Relations between higher order TV regularization and support vector regression,” *Scale-Space, PDE Methods Comput. Vis.*, vol. 3459, pp. 515–527, Jan. 2005.

[80] T. T. Do, X. Lu, and J. Sole, “Compressive sensing with adaptive pixel domain reconstruction for block-based video coding,” *IEEE Intern. Conf. on Image Processing* (ICIP), pp. 3377-3380, 2010.

[81] M. P. Vishal, M. Ray, C. G. Anna, and C. Rama, “Gradient-based image recovery methods from incomplete Fourier measurements,” *IEEE Trans. on Image Processing*, vol. 21, no. 1, Jan. 2012.

[82] J. Zhang, S. Liu, and D. Zhao, R. Xiong, and S. Ma, “Improved total variation based image compressive sensing recovery by nonlocal regularization,” *IEEE Int’l Symposium on Circuits and Systems* (ISCAS), pp. 2836 – 2839, 2013.

[83] B. Wohlberg and P. Rodriguez, “An iteratively reweighted norm algorithm for minimization of total variation functionals,” *IEEE Signal Processing Letters*, vol. 14, no. 12, pp. 948 – 951, Dec. 2007.

[84] O’D. Nicholas, and M. F. M. Jose, “On the product of independent complex Gaussians,” *IEEE Trans. on Signal Processing*, vol. 60, no. 3, pp. 1050 – 1063, Mar. 2012.

[85] R. A. Fisher, “Application of student’s distribution,” Metron, 5:90 – 104, 1925. Available online: http://digital.library.adelaide.edu.au/dspace/ handle/2440/15187.

[86] R. E. Walpole, R. H. Myers, S. L. Myers, *Probability and statistics for engineers and scientists*, Pearson Education, 7th edition.

[87] Z. Huang, and P. Tsai, “Efficient implementation of QR decomposition for gigabit MIMO-OFDM systems,” *IEEE Trans. Circuits and Systems I*, vol. 58, no. 10, pp. 2531 – 2542, Oct. 2011.

[88] D. Besiris, V. Tsagaris, N. Fragoulis, C. Theoharatos, “An FPGA-based hardware implementation of configurable pixel-level color image fusion,” *IEEE Trans. Geoscience and Remote Sensing*, vol. 50, no. 2, pp. 362 – 373, Feb. 2012.

[89] Y. Bei, M. Wu, C. Studer, J. Cavallaro, and C. Dick, “Implementation trade-offs for linear detection in large-scale MIMO systems,” *IEEE Int’l Conf. on Acoustics, Speech, and Signal Processing*, May 2013.

[90] Z. Ben-Haim, Y. Eldar, and M. Elad, “Coherence-based performance guarantees for estimating a sparse vector under random noise,” *IEEE Trans. on Signal Processing*, vol. 58, no. 10, pp. 5030 –5043, Oct. 2010.

[91] E. Candès and T. Tao, “The Dantzig selector: statistical estimation when p is much larger than n,” *The Annals of Statistics*, vol. 35, no. 6, pp. 2313–2351, 2007.

[92] R. M. Bassem and E. Atef, *MATLAB simulations for radar systems design*, Chapman and Hall/CRC, 1st edition. 2003.

[93] M. O. Robert, “Radar systems engineering,” available online: http://ece.wpi.edu/radarcourse/radar%20se%20List%20of%20Lectures%20.html

[94] M. Skolnik, *Introduction to radar systems*, McGraw-Hill Science, 3rd edition, 2002.

[95] J. Zhou, S. Palermo, B. M. Sadler, and S. Hoyos, "Asynchronous compressive sensing in radar systems," *IEEE Texas Symposium on Wireless and Microwave Circuits and Systems*, pp.1 – 4, Apr. 2013.

[96] "National science foundation workshop on enhancing access to the radio spectrum," final report, August 4-6, 2010, available online, http://www.nsf.gov/mps/ast/ears_workshop_final_report_ce_final_corr.pdf

[97] M. Xing, Q. Wang, G. Wang, and Z. Bao, "A matched-filter-bank-based 3-D imaging algorithm for rapidly spinning targets," *IEEE Trans. On Geoscience and Remote Sensing*, vol. 47, no. 7, pp: 2106 – 2113, 2009.

[98] D. Hai, B. Himed, "Interference mitigation processing for spectrum-sharing between radar and wireless communications systems," *IEEE Trans. on Aerospace and Electronic Systems*, vol. 49, no. 3, pp: 1911 – 1919, 2013.

[99] M.A. Herman and T. Strohmer, "High-resolution radar via compressed sensing," *IEEE Trans. on Signal Processing*, vol. 57, no. 6, pp. 2275 – 2284, 2009.

[100] W. Bajwa, K. Gedalyahu, and Y. Eldar, "Identification of parametric underspread linear systems and super-resolution radar," *IEEE Trans. on Signal Processing*, vol. 59, no. 6, pp. 2548 – 2561, 2011.

[101] J. Zhou, S. Palermo, José S. Martínez, B. M. Sadler, and S. Hoyos, "Asynchronous compressive radar," the *39th Annual Government Microcircuit Applications & Critical Technology Conference* (GOMACTech), to appear in Mar. 2014.

[102] General rules, techniques and advice for all drivers and riders (103 to 158). Government of United Kingdom. Available online: https://www.gov.uk/general-rules-all-drivers-riders-103-to-158/control-of-the-vehicle-117-to-126

[103] S. Hoyos, S. Pentakota, Z. Yu, E. Sobhy, X. Chen, R. Saad, S. Palermo, and J. Silva-Martinez, "Clock-jitter tolerant wideband receivers: an optimized multi-channel filter-bank approach," *IEEE Transactions on Circuits and Systems I*, vol. 58, no. 2, pp. 253 – 263, Feb. 2011.

[104] E. Fishler, A. Haimovich, R. Blum, L. Cimini, D. Chizhik, R. Valenzuela, "Spatial diversity in radars–models and detection performance," *IEEE. Trans. on Signal Processing*, vol. 54, no. 3, pp: 823 – 838, Mar. 2006.

[105] J. Zhou and S. Hoyos, "Asynchronous compressive multi-channel radar for interference-robust vehicle collision avoidance systems," *IEEE Texas Symposium on Wireless and Microwave Circuits and Systems*, Apr. 2014.

[106] J. Zhou, Y. He, B. M. Sadler, and S. Hoyos, "Compressed digital beamformer with asynchronous sampling for ultrasound imaging," *IEEE International Conf. on Acoustics, Speech, and Signal Processing*, pp. 1056 – 1060, May 2013.

[107] T. L. Szabo, *Diagnostic ultrasound imaging: inside out* (Elsevier), 2004.

[108] G. D. Kim, C. Yoon, S. B. Kye, Y. Lee, J. Kang, Y. Yoo, and T. K. Song, "A single FPGA-based portable ultrasound imaging system for point-of-care applications," *IEEE Trans. on Ultrasonics, Ferroelectrics and Frequency Control*, vol. 59, no. 7, pp: 1386-1394, July 2012.

[109] S. K. Edelman, *Understanding ultrasound physics*, 3rd edition (Esp), Dec. 2003.

[110] A. Agarwal, Y. Yoo, F. Schneider, C. Gao, K. Mong, and Y. Kim, "New demodulation method for efficient phase-rotation-based beamforming," *IEEE Trans. on Ultrasonics, Ferroelectrics and Frequency Control*, vol. 54, no. 8, pp: 1656 – 1668, Aug. 2007.

[111] Y. F. Li and P. C. Li, "Ultrasound beamforming using compressed data," *IEEE Trans. on Information Technology in Biomedicine*, vol. 16, no. 3, pp. 308 – 313, May 2012.

[112] N. Wagner, Y.C. Eldar, and Z. Friedman, "Compressed beamforming in ultrasound imaging," *IEEE Trans. on Signal Processing*, vol. 60, no. 9, pp. 4643 – 4657, Sept. 2012.

[113] J. A. Jensen, "Field: a program for simulating ultrasound systems," Proceedings of the 10th Nordic-Baltic Conference on Biomedical Imaging, Published in *Medical & Biological Engineering & Computing*, pp. 351 – 353, Volume 34, Supplement 1, Part 1, 1996.

[114] J. A. Jensen and N. B. Svendsen, "Calculation of pressure fields from arbitrarily shaped, apodized, and excited ultrasound transducers," *IEEE Trans. Ultrason., Ferroelec., Freq. Contr.*, 39, pp. 262-267, 1992.

[115] J. T. Bushberg, J. A. Seibert, E. M. Leidholdt, and J. M. Boone, *The essential physics of medical imaging*, Lippincott Williams & Wilkins, 3rd edition, 2011.

[116] O. Abari, F. Lim, F. Chen, and V. Stojanović, "Why analog-to-information converters suffer in high-bandwidth sparse signal applications," *IEEE Trans. Circuits and Systems I*, vol. 60, no. 9, pp. 2273 – 2284, Sep. 2013.

[117] X. Chen, E. Ahmed, Z. Yu, S. Hoyos, J. Silva-Martinez, S. Palermo, and B. M. Sadler, “A sub-Nyquist rate compressive sensing data acquisition front-end,” *IEEE J. on Emerging and Selected Topics in Circuits and Systems*, vol. 2, no. 3, pp. 542 – 551, Sep. 2012.